Measurement of B-Hadron Masses at CDF Run II

by

Andreas Korn

Submitted to the Department of Physics
in partial fulfillment of the requirements for the degree of

Doctor of Philosophy

at the

MASSACHUSETTS INSTITUTE OF TECHNOLOGY

September 2004

Author .....

Department of Physics
May 26, 2004

Certified by .....

Christoph M.E. Paus
Assistant Professor
Thesis Supervisor

Accepted by .....

Thomas J. Greytak
Professor, Associate Department Head for Education

Measurement of B-Hadron Masses at CDF Run II

by

Andreas Korn

Submitted to the Department of Physics
on May 26, 2004, in partial fulfillment of the
requirements for the degree of
Doctor of Philosophy

Abstract

We measure the mass of b-hadrons in exclusive J/ψ-decay modes. The correct momentum scale is established by the following steps: validate and quantify distortions or systematic effects in the Central Outer Tracker and Silicon Vertex Detector, apply and fine tune the energy loss corrections per track, and finally tune the magnetic field scale. With the momentum scale established, we find:

$$\begin{aligned} m(B^+) &= 5279.10 \pm 0.41\,_{(stat)} \pm 0.36\,_{(sys)}, \\ m(B^0) &= 5279.63 \pm 0.53\,_{(stat)} \pm 0.33\,_{(sys)}, \\ m(B_s^0) &= 5366.01 \pm 0.73\,_{(stat)} \pm 0.33\,_{(sys)}, \\ m(\Lambda_b) &= 5619.7 \pm 1.2\,_{(stat)} \pm 1.2\,_{(sys)}\ \mathrm{MeV/c^2}. \end{aligned}$$

The measurements of the Λ_b and B_s masses are the current world best. The value of the Λ_b mass is consistent with the CDF run I measurement resolving a discrepancy in the PDG average.

Thesis Supervisor: Christoph M.E. Paus
Title: Assistant Professor

Acknowledgments

Ista Horribilis Taetraque Finita est Passio

---

anonymous

The acknowledgment section of every thesis is in a way also an account of that phase in one's life. But compressing the last years into a few pages is of course an impossible task.

I would like to thank my advisor Prof. Christoph Paus for giving me the opportunity to come to MIT. I admire him as the hardest working person I know. I would like to thank him and my academic advisor Bolek Wyslouch for their guidance through the rough waters at the institute.

I'm indebted to my previous science educators, in particular Prof. Hebbeker, Prof. Keiper and my high school teacher Mr. Mahn.

I would like to thank the MIT group for sharing the burden of grad school experience with me. My fellow graduate students Ivan Furic, Konstantin Anikeev, Mike Mulhearn and Sasha Rakitine provided the atmosphere needed, to get the work done. Thanks to the younger students, Alberto Belloni, Arkady Bolshov, Boris Iyutin, Nuno Leonardo and Jeff Miles for freeing my time during the last year, by taking over our hardware responsibilities. David Starr contributed to this work with his undergraduate thesis. Gerry Bauer's broad scientific curiosity was a constant inspiration. From Steve Tether I learned a lot about computing and more Science-Fiction anecdotes than I can remember. I gained more than one insight during discussions with Sham Sumorok. And if you would have paid attention, you too would have noticed his dry British humor as a welcome entertainment at group meetings. Jeff Tseng always had an open door and we talked about physics and beyond. Ilya Kravchenko is not only a good collegue, I consider him a friend. Getting to know the previous generation of the CDF MIT group Prof. Paris Sphicas, Tushar Shah, Paul Ngan, Ken Kelly and Dejan Vucinic was an honor. At MIT Prof. Jerry Friedman is still the niecest person around. Peggy Berkowitz and Roger Gaul deserve a thank you for their support in all administrative matters.

It is not easy to describe the interesting group dynamics of a large collaboration like CDF. I would like to mention Marjorie Shapiro, Stefano Giagu, Pasha Murat, Young-Kee Kim, Nigel Lockyer, Ting Miao, Jonathan Lewis, Barry Wicklund and Joe Kroll as some of the people that made an impression on me. Working with the muon software group under the leadership of Michael Schmitt and Ken Bloom was a very enjoyable experience. Rick Tesarek as chair of my godparenting committee had an important part in getting the documentation into shape.

Thanks to the "Coffee Club" and the British tea faction for many enjoyable discussions. Farrukh deserves to be mentioned separately as a friend and the best cook I know. Thanks to Maria for dragging me out of the office on occasion. Thanks to Uli, Uli, Ayres and Kurt for helping to keep up my few Doppelkopf skills while at Fermilab. Thanks to Stephi, Kurt, Marcel, Uli and Claudia of the Karlsruhe group for shared times in and out of the office.

A very special thanks goes to all my friends in Berlin. I think most of them don't realize how much they kept me sane.

At last, but not least I would like to thank my parents Erika and Horst Korn. Without their unconditional support I would have never have made it this far.

Finally I would like to express my apologies to any person that I forgot to mention.

Contents

List of Figures

List of Tables

Chapter 1

Introduction

1.1 The Origin of Mass

What is the origin of the mass of the everyday objects around us? This question is best addressed by taking an object apart and look whats inside. Objects can be composed of different substances, but every material is made of a collection of atoms in molecules or lattice structures. Atoms in turn contain a core of nucleons surrounded by an electron cloud. The contribution of the mass of electrons to the total mass of an atom can be safely neglected. The mass of regular matter is determined by the mass of the nucleons: protons and neutrons.

In the Standard Model, which is the leading theory of particle physics, nucleons are composite particles and the mass of a nucleon is given by the binding energy and mass of it's constituent quarks [1]. Quarks carry color charge and are bound by the strong force. The binding energy can be calculated by the theory of strong interactions, Quantum Chromodynamics or short QCD.

1.2 B-hadrons

Hadrons are colorless particles made up of strongly-interacting constituents. We currently know of two types: mesons and baryons. A meson is formed by a quark-anti-quark pair. Baryons contain three quarks. Recently hints of a third type of

Table 1.1: Properties of the known quarks.

generation	1	2	3
quark	u	c	t
charge	+2/3	+2/3	+2/3
mass	$1-5$ MeV	$1.15-1.35$ GeV	174.3 ± 5.1 GeV
quark	d	s	b
charge	-1/3	-1/3	-1/3
mass	$3-9$ MeV	$75-175$ MeV	$4.0-4.4$ GeV

hadrons, so called penta-quarks, has been found [2].

A total of six quark flavors have been observed. They are organized into three families or generations of iso-doublets. The properties of the six quarks are summarized in Table 1.1. The first family consists of up and down quarks, the constituents of the matter around us. The second family is comprised of charm and strange quarks. The third family contains top and bottom. Because the top quark is very heavy, it decays before it hadronizes. This makes the b quark interesting for study, as it is the heaviest quark that forms hadrons. The quark content of b-hadrons of interest is summarized in Table 1.2.

Table 1.2: Quark composition of b-hadrons.

b-hadron	quark-content
B^0	$d\bar{b}$
B^+	$u\bar{b}$
B_s^0	$s\bar{b}$
Λ_b	udb

Particles containing quarks of the second and third generation are not stable. In order to carry out measurements involving particles of these generations, we have to produce them in collisions.

1.3 B-hadrons in $p\bar{p}$-collisions

The experimental environment at a $p\bar{p}$-collider has a number of unique properties. The $b\bar{b}$ total production cross section is about 100 μb [3]. This production rate is very large, when compared with $\sim$ 1 nb for e^+e^--colliders running at the $\Upsilon(4s)$ resonance [4] and $\sim$ 6 nb running at the Z^0 [5]. The high rate is the main advantage of a $p\bar{p}$-machine, it comes at the price of large backgrounds. The total $p\bar{p}$-interaction cross section is 75 mb [6], almost three orders of magnitude higher than $b\bar{b}$ production. A further complication arises from the compositness of the colliding particles. The constituents of proton, quarks and gluons, are commonly referred to as partons. The collision takes place between partons, that carry only a fraction of the proton momentum. The parton momentum fraction and therefore the center of mass energy in a collision is unknown. The proton/anti-proton constituents that do not directly take part in the hard scattering, will also form hadronic showers. These particles are called underlying event. The average number of charged particles in a b-event, that reach the tracking chamber is about 30.

The high rate and large background fraction require a selection of interesting events. A trigger is the most critical ingredient for any physics at a $p\bar{p}$-collider and b-physics in particular. Two strategies are employed: trigger on lepton signature and trigger on a secondary vertex. A fraction of b-hadrons decays semi-leptonically or into a J/ψ that decays into two leptons. These decays are selected by the lepton triggers. The secondary vertex trigger exploits the relative long lifetime of heavy flavor hadrons.

1.4 Overview of mass measurement

Using a sample of J/ψ mesons collected with the di-muon trigger, a precision mass measurement of b-hadrons is performed and presented in this thesis. Candidates of b-hadrons are reconstructed in exclusive J/ψ-decay channels. The same J/ψ-sample used to reconstruct the b-hadrons is used to establish the momentum scale prerequisite

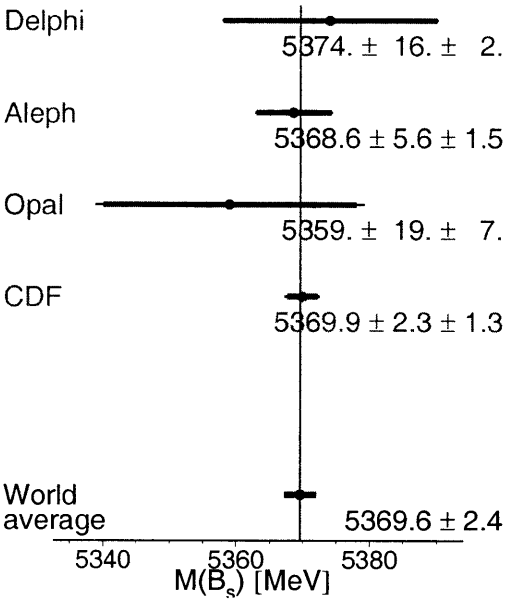

Figure 1-1: Summary of the measurements used for the PDG average of the B_s^0-mass.

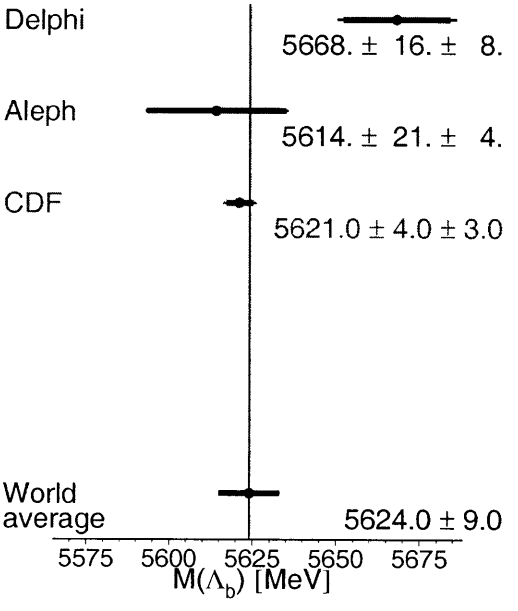

Figure 1-2: Summary of the measurements used for the PDG average of the Λ_b-mass. Results from DELPHI [7], ALEPH [8] and CDF Run I [9] are shown.

for this measurement. The correct momentum scale is determined by the following steps: validate and quantify distortions or systematic effects in the Central Outer Tracker and Silicon Vertex Detector, apply and fine tune the energy loss corrections per track, and finally tune the magnetic field scale. The resulting correction method is applied to the reconstructed b-hadron decays. Finally the mass for each mode is extracted using an unbinned likelihood fit.

While the B^0 and B^+ masses are known relatively well, the B_s^0 and Λ_b masses have considerable uncertainties. The situation for the B_s^0 is shown in Figure 1-1. The previous best measurement of the B_s^0 mass was performed at CDF Run I [10, 11].

The Λ_b mass is quoted in the PDG [12] as: $m(\Lambda_b)_{PDG} = 5624 \pm 9$ MeV/c^2. This value is based on an average of three experiments as shown in Figure 1-2. Both LEP measurements are based on only 4 candidates each. The DELPHI measurement is in disagreement with a simple average and the authors of the PDG scale the combined uncertainty. This scaling is performed in order to "normalize" the χ^2 of the combined measurements.

$$\chi^2 = \sum_{i=1}^{Nexp} \frac{(\bar{x} - x_i)^2}{\sigma_i^2}$$

The combined χ^2 of the three measurements is $0.3 + 0.2 + 6.1 = 6.6$ resulting in a scale factor of $\sqrt{\frac{\chi^2}{N-1}} = \sqrt{\frac{6.6}{3-1}} = 1.8$. This new measurement with significantly better accuracy and larger data sample helps to clarify this issue.

The D0 and CDF detectors at the Tevatron are currently the only places where B_s mesons and Λ_b baryons can be studied. The CDF detector is equipped with a large and accurate tracking system, making it a unique place to perform high precision mass measurements.

Chapter 2

Theory

2.1 Quantum Chromodynamics

A detailed introduction to QCD is well beyond the scope of this thesis and we refer the reader to [13]. Quantum Chromodynamics is a gauge theory which describes the strong interaction between quarks and gluons [14, 15, 16, 17]. The gauge theory is based on the non-abelian $SU(3)_C$ color symmetry. Quarks come in three colors: "red", "green" and "blue". Gluons as mediators of the strong force carry a color charge and therefore couple to themselves. The self-interaction of gluons is the reason behind the confinement and asymptotic freedom of QCD.

The running of the strong coupling constant α_s is given by the renormalization group equation:

$$\alpha_s(\mu_2) = \frac{1}{\frac{1}{\alpha_s(\mu_1)} - \beta_0 \ln\left(\frac{\mu_2^2}{\mu_1^2}\right)} \tag{2.1}$$

The gluon self coupling makes the β-function negative:

$$\beta_0 = -\left(\frac{33 - 2N_q}{12\pi}\right) \tag{2.2}$$

The coupling constant vanishes for large momentum transfers or small quark separations. This behavior is called asymptotic freedom. For large distances the coupling constant becomes very large. Quarks are bound stronger and stronger the more they

are separated. The separation of colored objects is therefore impossible, a fact that is called confinement. Quantum Chromodynamics can be treated perturbatively only at very small distances, where the coupling is small. The large coupling constant at large distances or small momenta requires a non-perturbative treatment. The calculation of hadron masses can be done only in the non-perturbative regime.

2.2 Predictions

The use of mass calculations to test Quantum Chromodynamics is as old as QCD itself. One of the first predictions was the Gell-Mann-Okubo mass formula for mesons and baryons [14, 18]. When considering only u, d and s quark flavors and assuming $m(q_i) - m(q_j) \ll \Lambda_{QCD}$ QCD exhibits a $SU(3)_F$ flavor symmetry. The $SU(2)$ iso-spin symmetry is a subgroup of $SU(3)_F$. Gell-Mann utilized the $SU(3)_F$ symmetry and its breaking due to the strange quark mass to arrive at the relation:

$$3m_\eta^2 = 4m_K^2 - m_\pi^2; \quad 3m_\Lambda = 2(m_n + m_\Xi) - m_\Sigma$$

Quarks also carry electric charge. The interaction between different charge combinations introduces an electromagnetic mass splitting. This was first pointed out by Coleman and Glashow [19]:

$$m(\Xi^-) - m(\Xi^+) = m(\Sigma^-) - m(\Sigma^+) + m(p) - m(n)$$

Modern predications for heavy hadrons rely on special methods described below. The determination of hadron masses, which can be thought of spectroscopy of a QCD system, serves as a crucial cross check for these methods. A successful test gives confidence in the calculation of other quantities. In addition the mass is needed as input. The mass enters for example as $\sim m^5$ into decay rate calculations. A precise mass measurement is therefore needed in order to extract quark mixing parameters from lifetime measurements. The current mass predictions for b-hadrons are summarized in Table 2.1.

Table 2.1: Theoretical predictions of b-hadron masses and mass differences.

type of calculation	quantity	prediction
relativistic	$m(B_d^0)$	5285 MeV
Potential Model [20, 21]	$m(B_s^0)$	5375 MeV
HQET [22]	$m(B_s^0)$	5379 MeV
	$m(\Lambda_b)$	$5624 - 30$ MeV
Lattice	$m(B_d^0)$	$5296 \pm 4^{-2}_{+3}$ MeV
NRQCD [23]	$m(B_s^0)$	$5385 \pm 15^{-6-0}_{+7+20}$ MeV
	$m(B_s^0) - m(B_d^0)$	$87 \pm 9^{-3-0}_{+5+19}$ MeV
	$m(\Lambda_b)$	$5679 \pm 71^{-19}_{+14}$ MeV
Lattice NRQCD [24]	$m(B_s^0) - m(B_d^0)$	90 ± 10 MeV
Lattice	$m(B_s^0)$	$5380 \pm 108^{-21}_{+18}$ MeV
NRQCD [25]	$m(\Lambda_b)$	$5664 \pm 98^{-33}_{+46}$ MeV
Lattice QCD [26]	$m(B_s^0)$	5630 ± 170 MeV
	$2m(B_s^0) - m(\Upsilon)$	$1361 \pm 8 \pm 17$ MeV

2.2.1 Potential models

In general the QCD potential between two quarks can be written as [27]:

$$V(r) = -\frac{4}{3}\frac{\alpha_s}{r} + \sigma r \tag{2.3}$$

The first term describes the potential due to simple gluon exchange, similar to the Coulomb potential. The second term accounts for the confinement due to increasing coupling strength. The parameter σ is called "string tension" [28]. Apart from the Cornell potential of Equation 2.3 other empirical forms are used. For example the Richardson Potential [29]:

$$V(r) = \int d^3q e^{iq\cdot r}\frac{\alpha_s(q^2)}{4\pi q^2}$$

and variants of the Martin Potential [30, 31]:

$$V(r) = a\ln(r) + b$$

When comparing different potential models, it is observed, that the potentials agree

well in the region of $r \sim 0.1 - 0.8$ fm.

A heavy-light meson can be modeled as a relativistic light quark in a quasi-static heavy quark potential [20].

2.2.2 Lattice QCD

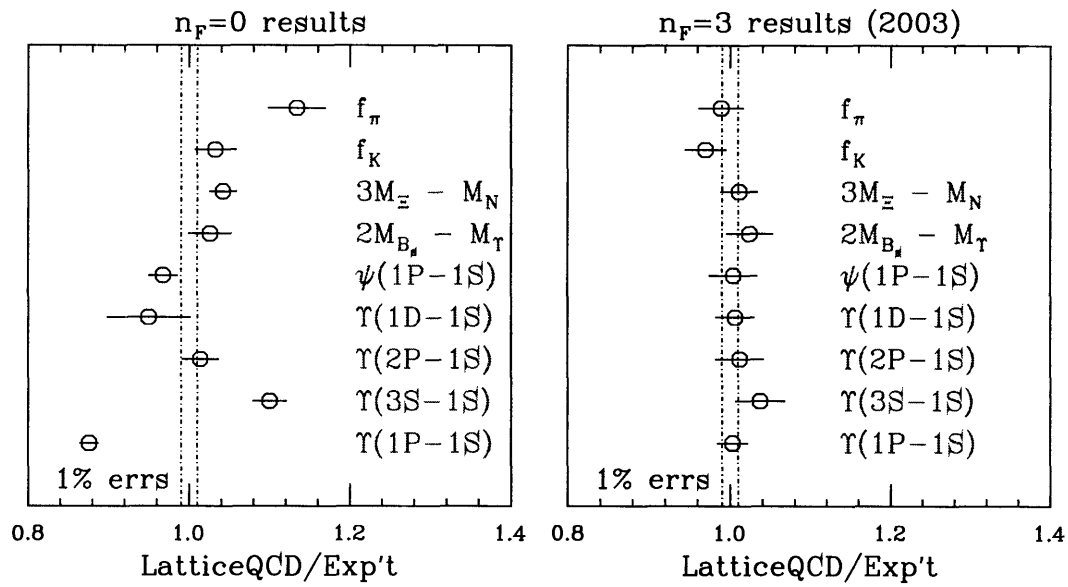

Figure 2-1: Ratio of lattice QCD results to experimental measurements for a selection of gold plated quantities [32]. Quenched results on the right compared to unquenched calculations on the left.

Lattice QCD attempts to solve the equations of QCD numerically on a discretized space time [33]. It uses the Feynman path integral formalism. This formalism can be thought of as the quantum mechanical extension of the least action principle. The value of an operator $\mathcal{O}$ is given by the integral over all possible path's weighted by their action $S = \int \mathcal{L} d^4x$ [34]:

$$< \mathcal{O} >= \frac{\int \mathcal{O} e^{-S} dU d\psi d\bar{\psi}}{\int e^{-S} dU d\psi d\bar{\psi}}$$

Here U and ψ denote the configurations of gluon and quark fields respectively. After discretization this integral can be evaluated as a sum over a set of configurations.

The action contains contributions from both gluon and quarks. Quarks as fermions need to be treated as anti-commuting quantities and can not be handled numerically. The quark contribution therefore needs to be integrated out by hand. After integration one finds that fermion loop contributions are given by a determinant $\det M(\psi)$. As the matrix M has a dimension comparable to the lattice size, evaluating this determinant is computationally very expensive. The "quenched" approximation is therefore common, which neglects contributions from dynamic quark loops. Only recently "unquenched" calculations have become available [32, 35]. As can be seen Figure 2-1 this results in a significant improvement.

Masses are calculated in units of lattice spacing. The exact lattice spacing is determined by comparing one chosen dimensionful quantity with its experimental value.

2.2.3 Heavy Quark Effective Theory

In the $m_Q \to \infty$ limit, heavy quarks are a static source of color charge without spin and flavor. In reality one has to take $\frac{1}{m_Q}$ corrections into account. This is the realm of HQET [36]. A result of the flavor blindness in HQET is the fact that mass splittings in D and B-mesons should be the same:

$$m(B^*) - m(B) = m(D^*) - m(D)$$

2.2.4 Nonrelativistic QCD

Nonrelativistic QCD performs an expansion in the relative, nonrelativistic velocity of the heavy quark [37]. The method is particularly suited for heavy quarkconia like J/ψ and Υ were both quarks can be treated nonrelativistically. It is an irony, that the B_c-meson as double heavy bc-state allows the most precise theoretical prediction, while the experimental mass uncertainty is still the largest.

The heavy quark propagator of NRQCD effective theory can be used in lattice calculations. This is very attractive, as this simplified propagator reduces the com-

putational cost.

Chapter 3

Tevatron Collider and CDF Detector

3.1 Tevatron

The CDF detector is located at the Tevatron $p\bar{p}$-collider at Fermilab. Until the turn-on of the LHC, the Tevatron will be the world's highest energy collider. For RUN II, which began in 2001, the accelerator complex has gone through major upgrades. The center of mass energy was raised from 1.8TeV to 1.96TeV. A large increase in luminosity was attempted by reducing the time between beam crossings to 396ns. The currently achieved record instantaneous luminosity is 7.2×10^{31} $\mathrm{cm}^{-2}\mathrm{s}^{-1}$ to be compared with the design of 2×10^{32} $\mathrm{cm}^{-2}\mathrm{s}^{-1}$.

The acceleration process starts with Cockroft-Walton Voltage Multipliers [38]. Negative H^- ions are produced from hydrogen gas in a 750keV DC electric field. In the following Linac, H^- ions are accelerated to 400 MeV. The Linac produces a $20\mu s$ long pulse. The revolution time in the Booster [39], a synchrotron of 74.47m radius [40], is $2.2\mu s$. The long Linac pulse has therefore to be continuously added to up to eleven turns in the Booster [41]. During injection into the Booster the beam passes through a thin foil, which removes all electrons from the ion. In the Booster stage the proton energy is increased to 8 GeV.

The Main Injector is one of the important Tevatron upgrades [42]. In comparison

to its predecessor, the Main Ring, it allows a higher particle rate. From the Main Injector a 120 GeV proton beam is supplied to the Anti-proton Source [43]. In the first stage of the Anti-proton Source, the 120 GeV proton beam collides with a nickel target. In this collision many different particles are produced. The created particles are focused using a Lithium lens, essentially a high current magnet. A bending magnet acting as mass spectrometer separates the anti-protons from other particles. About 20 anti-protons are produced for every 1 million proton collision [43]. The anti-protons are then injected to Debuncher.

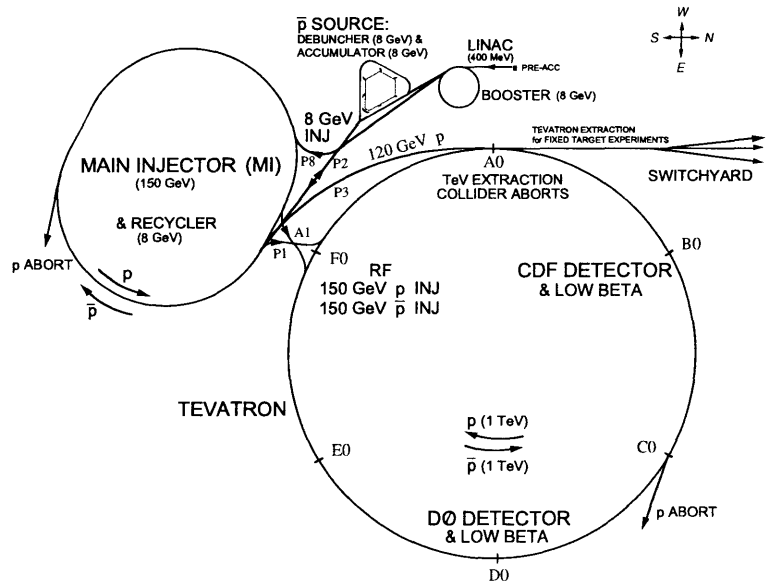

Figure 3-1: An overview of the Tevatron Accelerator chain.

The Debuncher ring translates the pulsed beam with large energy spread into a continuous beam with only small differences in energy. This is accomplished by sending particles of different kinetic energy on different orbits. The construction is such, that a particle with higher than average energy will perform a longer orbit with less acceleration. The remaining energy spread still needs to be reduced further. A technique called "stochastic cooling" is used in both the Debuncher and the following Accumulator [44]. The Accumulator is capable of storing and cooling anti-protons for tens of hours until the needed intensity is reached.

Particles can enter the Main Injector from three sources: the Booster, the Anti-proton Source and the Recycler. The Main Injector now accelerates protons and anti-protons to 150 GeV and injects them into the final acceleration stage, the Tevatron Ring.

The Tevatron Ring with a circumference of 4.26 miles acts as both an accelerator and a storage ring. The ring is build using superconducting magnets and accelerates the beam from 150 GeV to 980 GeV. Beams of counter rotating protons and anti-protons can be stored for days, with the luminosity slowly declining with a time. The complete acceleration chain is sketched in Figure 3-1.

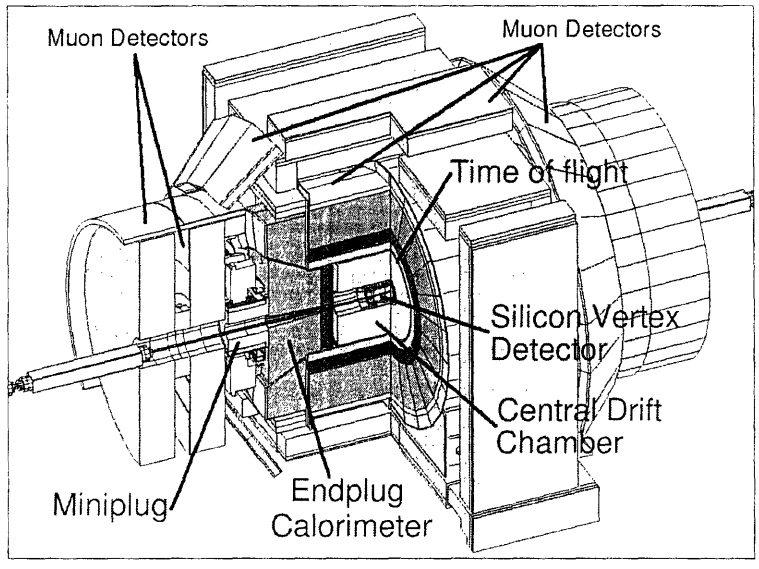

Figure 3-2: An overview of the CDF II detector.

3.2 Collider Detector Facility

3.2.1 Overview

The CDF detector shows a layered tube structure typical for HEP collider experiments. This is illustrated in Figure 3-2. Starting from the interaction point and moving outwards one encounters a precision vertex detector, a large tracking volume

inside a magnetic field, the magnet coils, electromagnetic and hadronic calorimetry and finally muon detectors. The coordinate system used is shown in Figure 3-3. The pseudo-rapidity, a frequently used quantity, which approximates a Lorentz invariant, is related to the angle θ:

$$\eta = -\ln \tan \frac{\theta}{2}.$$

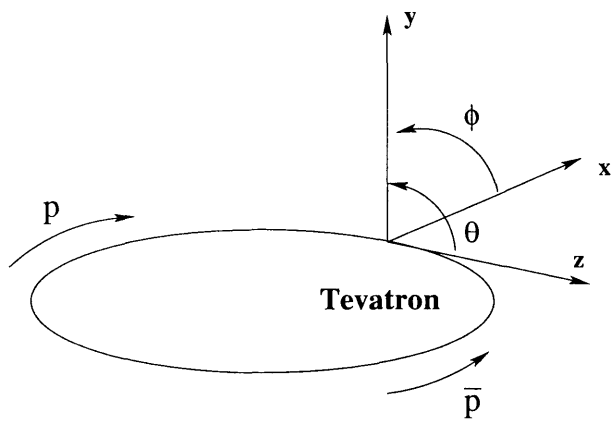

Figure 3-3: The CDF coordinate system.

For the analysis at hand, tracking, vertexing and muon identification are of importance. A detailed description of the CDF detector can be found in [45].

3.2.2 Tracking

The CDF tracking system consists of the Central Outer Tracker (COT) and the Silicon Vertex Detector (SVX). The system operates in a magnetic field of 1.4 T, provided by a superconducting solenoidal coil. The niobium-titanium coil operates at a current of 4650 A, regulated by a feedback loop. The curvature of charged particle trajectories in the magnetic field enables the measurement of particle momenta.

COT

A drift chamber consists of anode wires placed between cathode planes in a gas volume. A charged particle passing through a drift chamber ionizes the gas. Electrons

drift towards the anode or "sense wire". As the drift velocity is known, the drift time is translated into a spatial coordinate. Inside a magnetic field, the drift direction is rotated with respect to direction of the electric field by the Lorentz-angle. The high field near the sense wire results in an electron avalanche and an amplification of the signal with gains of up to 10^4.

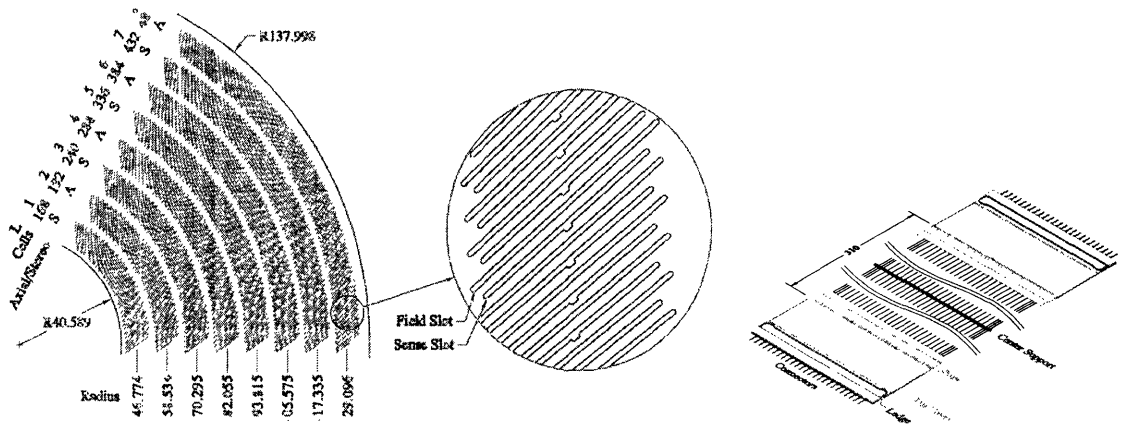

Figure 3-4: Shown is a quarter of the COT endplates. Eight superlayers with tilted wire planes are visible. A sense wire plane is shown on the right.

The COT is a large open-cell drift chamber segmented radially into eight superlayers [46]. The gas mixture is 50:50 Argone-Ethane. The mixture ensures short drift times of less than 100ns. Each superlayer contains 12 sense wires tilted by 35^o to compensate for the Lorentz-angle [47]. Neighboring sense wire planes are separated by a gold-plated Mylar cathode field sheet. Two adjacent field sheets with a sense wire plane in the middle form a drift cell. The single wire resolution is 150 μm.

In an "axial" layer sense wires and field shields are held in place by machined grooves in the end plates exactly opposite each other. In a "stereo" layer ends are offset by 6 cells forming a stereo angle of 2^o. The stereo angle allows for a crude z-coordinate measurement. The superlayers alternate between axial and stereo layer configuration, with the inner most layer being a stereo layer.

The drift chamber volume is 310 cm long with an inner bore of 40.59 cm. The COT extends to an radius of 137.99 cm and provides a large lever arm for the curvature

measurement. The raw momentum resolution achieved is:

$$\frac{\sigma(\mathrm{p})}{\mathrm{p}} = (0.7 \otimes 0.1\frac{\mathrm{p_T}}{[\mathrm{GeV}]})\%.$$

The pseudo-rapidity coverage of the COT is $|\eta| < 1$ for tracks traversing all eight superlayers.

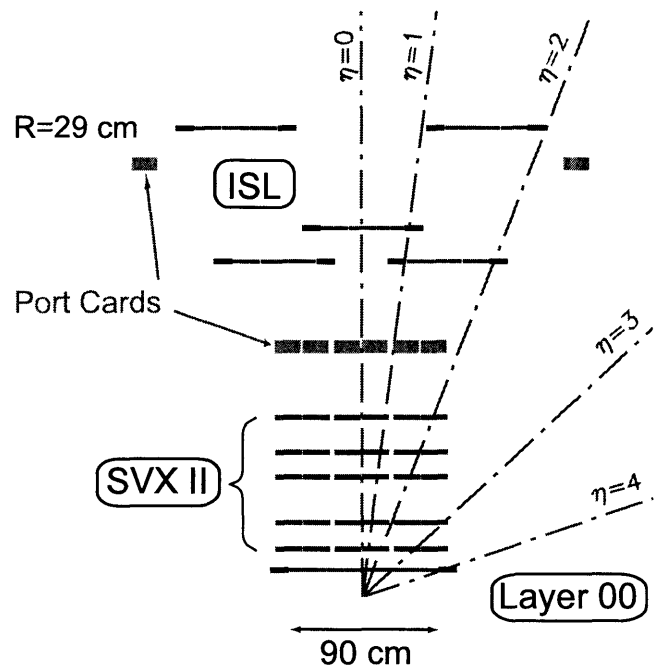

Figure 3-5: Location and extend of CDF silicon tracking systems in $r - z$ view.

SVX

Silicon strip detectors consist of extended semi-conductor diode strips. Voltage is placed on the diode to deplete the junction of charge carriers. An ionizing particle passing through the semi-conductor produces electron-hole pairs. The newly produced free electrons will drift towards the anode, holes towards the cathode. Good spatial resolution is achieved due to the small spacing between diode strips, the so called pitch. For CDF detectors, the pitch varies between $50 - 112$ μm.

The CDF silicon system can be divided into three parts: Layer00, Silicon VerteX

system for RUN II (SVXII) and the Intermediate Silicon Layer (ISL). An overview of the system is shown in Figure 3-6.

Layer00 is installed on the beampipe [48]. The location close to the interaction point provides a large improvement on the impact parameter resolution. The system is divided into 12 wedges. Six narrow layers are installed at a radius of 1.35 cm and six wide layers at a radius of 1.62 cm. The z-extent of Layer00 is 95 cm.

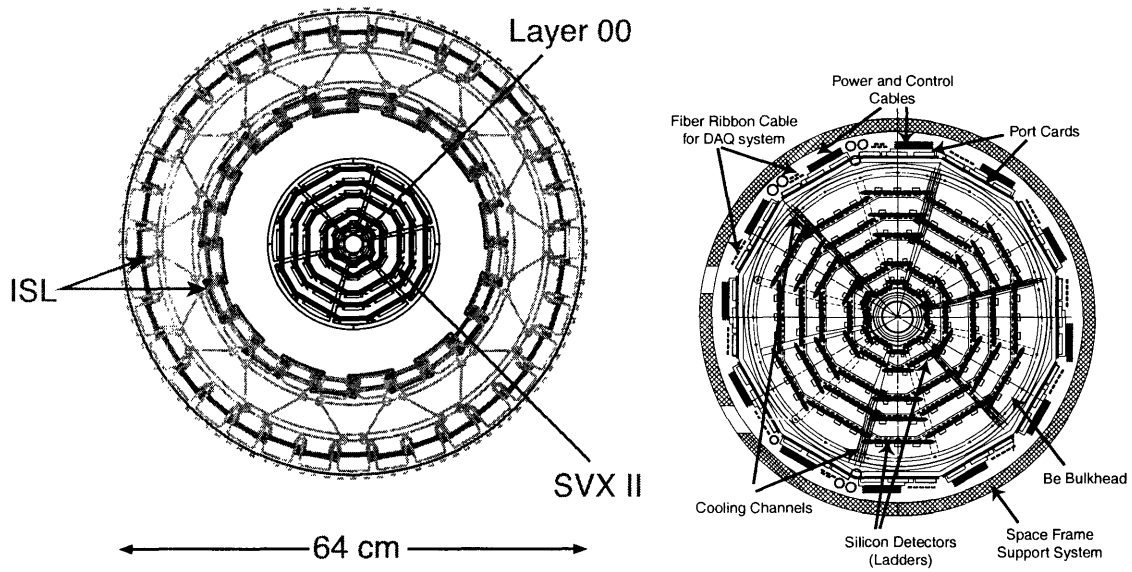

Figure 3-6: Location and extent of CDF silicon systems in $r - \phi$ view. On the right side a detailed view of the SVXII detector is shown.

Layer00 is surrounded by the main SVXII system consisting of 5 silicon layers [49]. The system is divided into 12 wedges and 3 barrels. The SVXII layers are made of double sided silicon. Double sided means that both anode and cathode are divided into strips. This is used to provide a measurement of the z-coordinate. Two configurations are employed: shallow angle stereo (SAS) at 1.2^o and 90^o stereo. Measurements of the z-coordinate in a 90^o stereo layer are far more accurate than shallow angle stereo measurements, but suffer from a large number of combinatorial ghost-hits. Layers 0, 1 and 3 are 90^o stereo layers, while layers 2 and 4 utilize SAS layers.

The system filling the gap before the COT is the ISL. The ISL covers the forward region up to a pseudo-rapidity of $|\eta| < 2$ as a complement to the COT. The ISL is

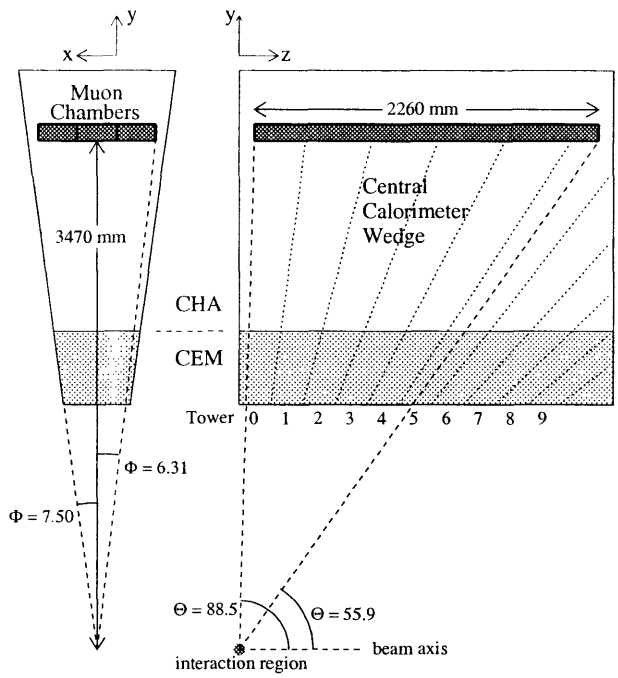

Figure 3-7: Geometry and location of the CMU chambers, the Central Hadron and Electromagnetic Calorimeter.

organized in three Layers, at 20 cm, 22 cm and 28 cm radius. The arrangement is shown in Figure 3-5.

3.2.3 Muon Detectors

Muons do not interact hadronically. Bremsstrahlung for muons is suppressed by a factor of over 40000 with respect to electrons, as this process is inversely proportional to the mass squared. The main interaction process for muons is ionization energy loss. Muon chambers are therefore placed after the electromagnetic and hadronic calorimeter. Electrons and most hadrons will be absorbed and only muons remain. The absorption material places a natural threshold on the energy of detectable muons. Muons below this energy will be stopped, a so called range out. At CDF the lowest range out threshold is 1.43 GeV. The location of the central muon chambers with respect to the calorimeters is shown in Figure 3-7.

The CDF muon system consists of 4 subsystems: Central Muon (CMU), Central

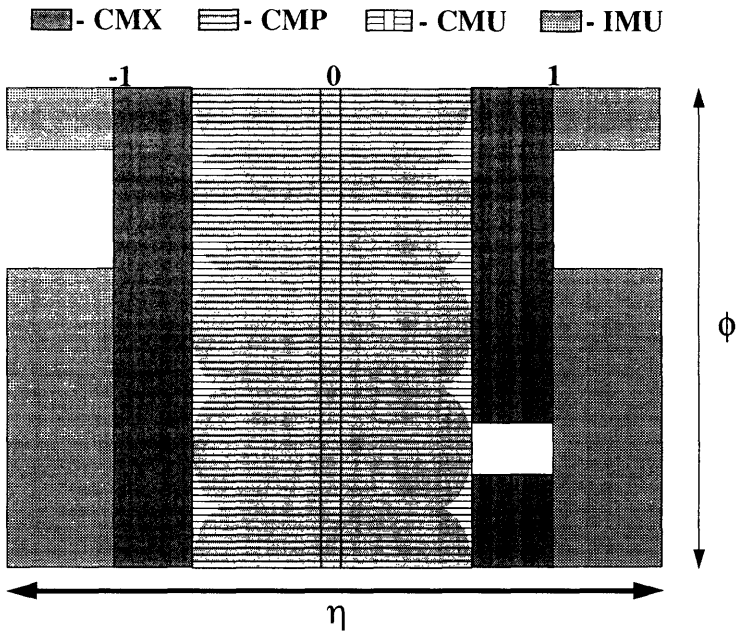

Figure 3-8: A sketch of the fiducial coverage of the CDF muon systems.

Muon uPgrade (CMP), Central Muon eXtension (CMX) and Intermediate MUon chambers (IMU). An overview of the coverage is shown in Figure 3-8. These systems usually consist of drift chambers combined with a layer of scintillation counters. A trajectory reconstructed from hits in the muon chambers is referred to as a muon stub. A muon is reconstructed offline by matching a track to a muon stub.

CMU

The Central Muon detectors (CMU) consist of two barrels, one each for the east and west side of the detector. The barrels are separated by 18 cm. The system covers a range in pseudo-rapidity up to $|\eta| < 0.6$.

The CMU is segmented in 24 wedges [50]. Each wedge contains 3 modules of 16 chambers each. Modules are subdivided into 4 layers and 4 stacks as seen in Figure 3-9. The construction of the chambers leaves a 1.5 degree gap in θ at the center and two 1.19 degree gaps in ϕ at the edges of each wedge. This is illustrated in Figure 3-7. A chimney runs through wedge number 5 on the east, requiring a reduced chamber

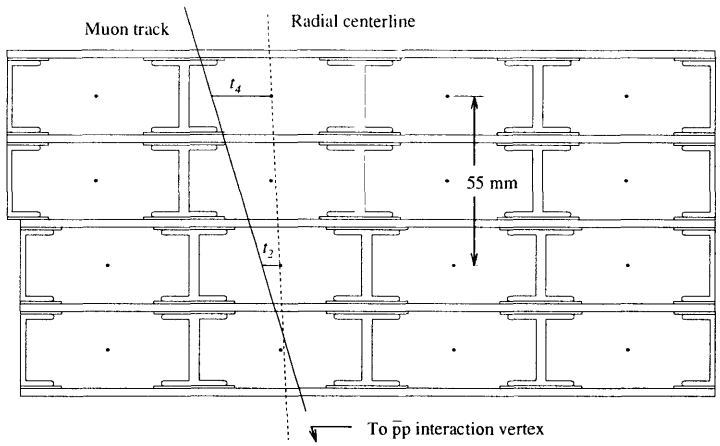

Figure 3-9: A CMU module is shown in cross-section. The layers are offset against each other to remove the left-right ambiguity of hit reconstruction.

size in this wedge.

Chambers on the east and west side are electrically joined at the middle. A measurement of the z-coordinate is possible via charge division. The collected charge is encoded into the pulse width.

CMP

The shielding material formed by the calorimeters in front of the central muon system, amounts to only about 5 interaction lengths. Energy from hadronic showers can leak into the back of the calorimeter, leaving hits in the CMU chambers. This source of fake muon hits is called a "punch through". To reduce this effect the CMP chambers were constructed behind additional steel absorbers. Muons need a transverse momentum above 2.2 GeV to reach the CMP.

The CMP system is arranged in a box shape of similar acceptance as the CMU and conventionally used as a confirmation of the CMU for higher momentum muons. A CMUP muon has both CMU and CMP stubs and a significantly better signal to noise ratio than muons identified by a single muon subsystem alone. A layer of scintillation counters (CSP) is mounted on the outer surfaces of the CMP.

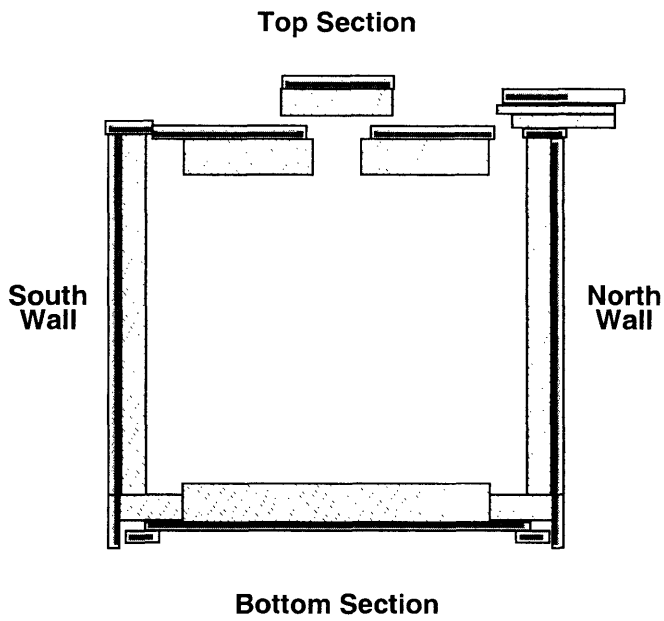

Figure 3-10: The location of the CMP chambers. [51]

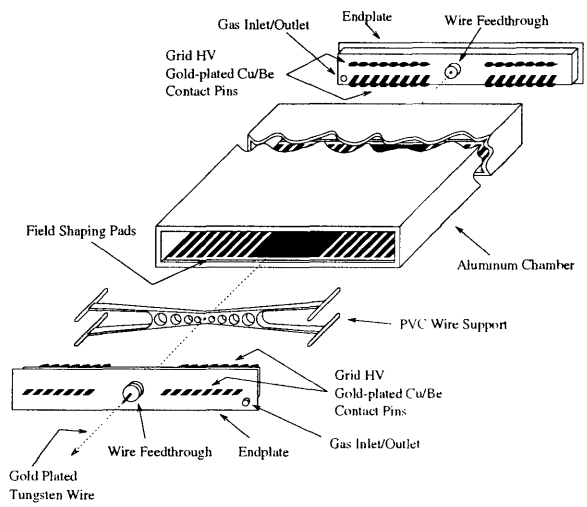

Figure 3-11: An exploded view of a single CMP drift cell [52].

An overview of the CMP geometry is given in Figure 3-10. The internal structure of the CMP is similar to that of the CMU. The rectangular shaped drift tubes have dimensions 2.5 cm × 15 cm × 640 cm. The details can be seen in Figure 3-11. Four tubes form a stack. Alternating layers are offset by ±7.62 cm.

CMX

The Central Muon eXtension consists of drift tubes (CMX) and scintillation counters (CSX) assembled in conical arranged sections. The CMX extends the pseudo-rapidity range to $0.6 < |\eta| < 1.0$. There are a total of 8 layers, but a fiducial muon can traverse at most 6 CMX layers. The arrangement of layers is shown in Figure 3-12. A measurement of the z-coordinate is possible due to a slight stereo-angle between different layers.

IMU

The Intermediate MUon system (IMU) extends the range of CDF muon chambers to a pseudo-rapidity of $1.0 < |\eta| < 1.5$ [53]. The IMU consists of Barrel MUon chambers (BMU), Barrel (BSU) and Toroid (TSU) scintillation counters. These forward chambers are mounted around the former toroid magnets for shielding. The steel acts also as additional shielding for the CMX counters. The IMU is not used in this analysis, mainly because no di-muon trigger was available for this system yet.

3.2.4 Time of Flight Detector

The Time of Flight system consists of 216 scintillator bars installed just inside the CDF solenoid [54]. The system was added in order to increase the particle identification to momenta below 1.5 GeV. This is illustrated in Figure 3-13. A charged track produces a light signal in the scintillator. This light is measured on both ends of the bars by nineteen stage fine-mesh PhotoMultiplier Tubes that can operate inside the magnetic field of 1.4 T. The double sided read out allows the determination of the z-coordinate of a track traversing the bar.

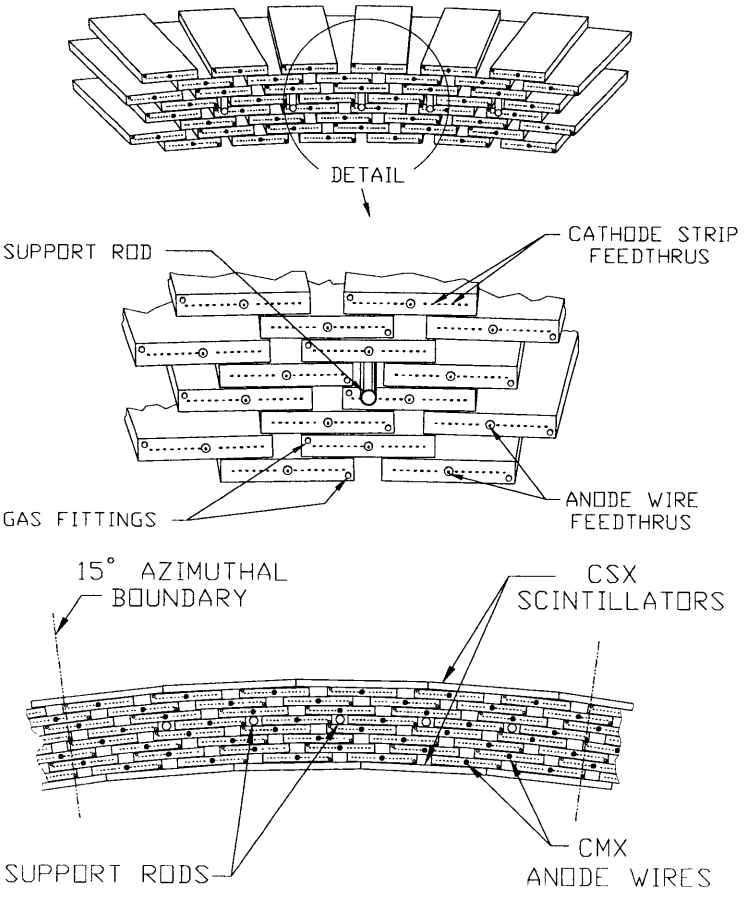

Figure 3-12: Layers of a CMX module are shown [52].

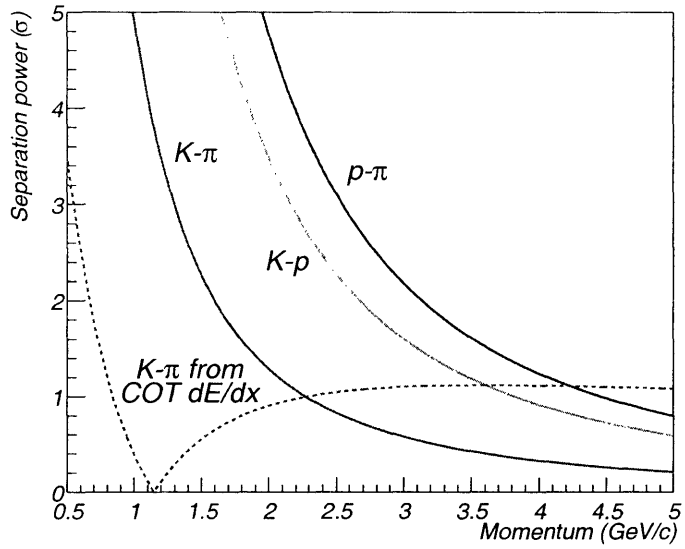

Figure 3-13: Separation power of the Time of Flight system versus momentum.

Velocity, mass and momentum are related via:

$$p = \gamma\beta mc = \frac{\beta}{\sqrt{1-\beta^2}}mc = \frac{1}{\sqrt{\frac{1}{\beta^2}-1}}mc = \frac{1}{\sqrt{\frac{(ct)^2}{L^2}-1}}mc.$$

Once flight time, pathlength and momentum of a track are known, it's mass can be calculated and used to distinguish different particle types.

3.2.5 Calorimetry

Calorimetry is used to measure the energy of incident particles. In general particles interact and form showers in the calorimeter. From the shower size the energy can be inferred.

Electromagnetic Calorimeter

The electromagnetic calorimeter provides energy measurements of electrons and photons.

The Central Electromagnetic caloriMeter (CEM) is build as a sampling calorime-

ter out of consecutive layers of lead and polystyrene scintillator. Lead is chosen as sandwich material for its high atomic number Z. Lead allows a large total depth of 19 X_0 in terms of radiation length while only having a thickness of 1 λ hadronic interaction length. The energy resolution obtained is $\frac{\sigma(E)}{E} = \frac{14.0\%}{\sqrt{E_T}} \otimes 2.0\%$. The location and tower segmentation of the CEM is shown in Figure 3-7.

The Central Electromagnetic Shower Maximum detector (CES) and the Central Preshower Radiator (CPR) are proportional chambers embedded in the CEM for improved spatial resolution. The CPR in addition allows for a better electron identification.

The central systems are complemented by the Plug Electromagnetic caloriMeter (PEM), the Plug Electromagnetic Shower Maximum detector(PES) and the Plug Preshower Radiator (PPR) in the forward region.

Hadron Calorimeter

The hadron calorimeter measures the energy of jets. The Central HAdron calorimeter (CHA) is an iron-scintillator sampling calorimeter with a total depth of 4.5 λ hadronic interaction length. The energy resolution achieved is $\frac{\sigma(E)}{E} = \frac{50.0\%}{\sqrt{E_T}} \otimes 3.0\%$. The CHA is complemented by the Plug HAdron calorimeter (PHA) in the forward region. The Wall HAdron calorimeter (WHA) fills the gap between both systems.

3.2.6 Trigger and DAQ

A collision at the Tevatron takes place every 396ns. It is impossible to read out and store the full detector information for each collision. A selection of interesting events is a necessity. In order to optimize the time available for this decision a three level trigger is used. Each level reduces the event rate further, while each level has more decision time and more event information available.

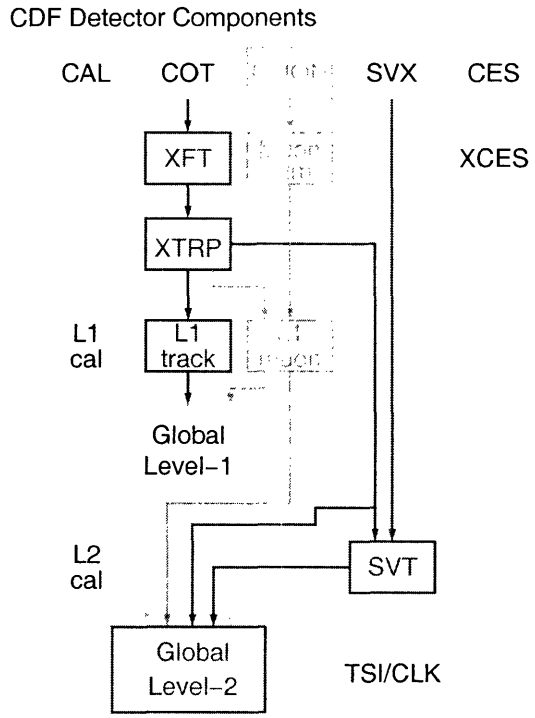

Figure 3-14: The trigger flow for muon triggers.

Level 1

The first level has 5 μs decision time available. This is accomplished using a 42-event deep pipeline. Given the short decision time required, the Level 1 trigger is based on hard-wired electronics. The trigger components important for this analysis are highlighted in Figure 3-14. The eXtremly Fast Tracker [55] transforms COT hits in a 1.25^o slice into a track estimate using a pattern lookup table. The XFT output are charge, 48 curvature bins and 7 bins for the ϕ position at radius of superlayer 6 in each slice. The first 15 low momentum curvature bins are twice as large as the high momentum bins. The last bin corresponds to infinite momentum.

The muon trigger looks for two hits in the muon chambers within a predefined time window in order to define a muon primitive. The time difference is related to the tilt of the muon stub as shown in Figure 3-9. The tilt of the muon trajectory is loosely related to the momentum of the muon and a cut on the timing window

corresponds to a momentum cut.

The eXTRaPolator module translates the track parameters of the XFT into a road pattern for the muon chambers. The XTRP performs an extrapolation with the help of a preloaded lookup table [56],[57]. A granularity of 2.5^o is used at Level 1. The di-muon trigger requires two separated muon primitives matched to XFT tracks.

The level 1 output rate is up to 40 KHz.

Level 2

At trigger level 2 is equipped with a 4 events deep buffer. The available decision time is extended to 20 μs. The time frame allows the use of programmable crate processors.

An exciting novel device is the Silicon Vertex Tracker (SVT) [58]. The SVT uses tracks from the Central Outer Tracking chamber as seeds to a parallelized pattern recognition in the Silicon Vertex Detector. The following linearized track fit returns track parameters with nearly offline resolution. The precise measurement of the track impact parameter allows one to trigger on displaced tracks from long-lived hadrons containing heavy flavor.

For the dataset described here all muon triggers were auto-accepted, as no Level 2 muon board was present.

Level 3

The last trigger stage is Level 3 [59]. At this trigger level the whole event is assembled in the Event Builder and passed onto a farm of commodity PC's where the event can be analyzed with reconstruction quality quantities.

The building of the event proceeds as follows. Analog signals from the different subdetectors are digitized and stored in the buffers of Front End crates. These buffers are read out via Front End Links. Up to 10 Front End Links are concentrated in a VME Readout Buffer (VRB). A VRB crate is controlled by a Scanner CPU (SCPU), a VME processor. The readout is synchronized via the Scanner Manager. The Level

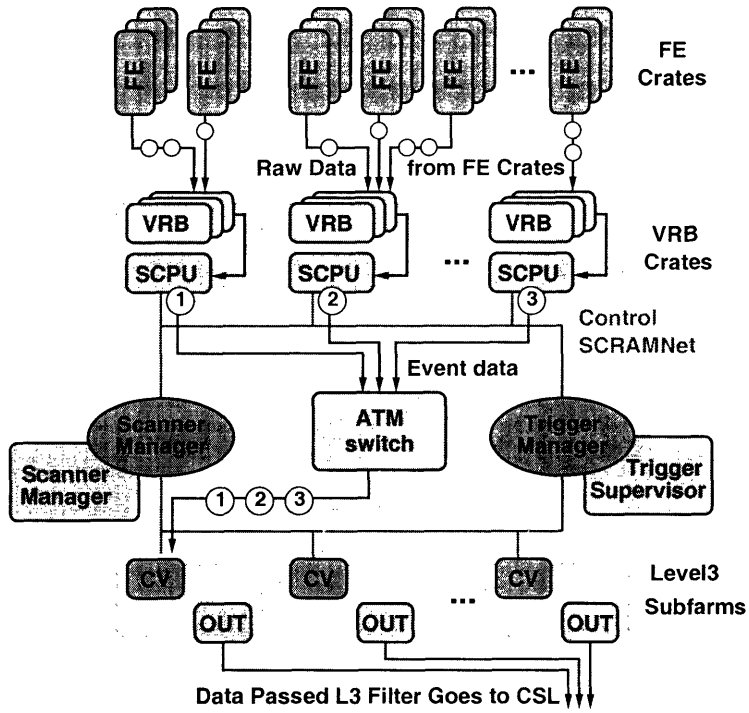

Figure 3-15: Shown is the event flow in the Level 3 trigger stage..

2 Global Accept is performed by the Trigger Supervisor. Scanner Manager, Trigger Supervisor and SCPU's are connected via a fast SCRAMNet control network ring.

Event fragments from 15 SCPU's are sent over an asynchronous transfer mode (ATM) switch to one of 16 converter nodes. Converter nodes are Linux PC's equipped with an ATM and a SCRAMNet card. The converter node assembles and formates the event fragments into a full event. Each converter node sends the assembled events to an idle processor node in the attached subfarm. A processor node is a dual processor PC running Linux. Each processor node runs 2 Level 3 Filter tasks. A Level 3 Filter task reconstructs the event and performs the Level 3 trigger decision. Accepted events are sent to an output node. The output rate out of Level 3 into the Consumer is $\sim$ 75Hz.

The system consists of a 250+ node processing farm. The flow of events is shown in Figure 3-15.

3.2.7 Offline Reconstruction and Simulation

Here we describe the low level reconstruction stages relevant for this analysis. In particular track and muon reconstruction.

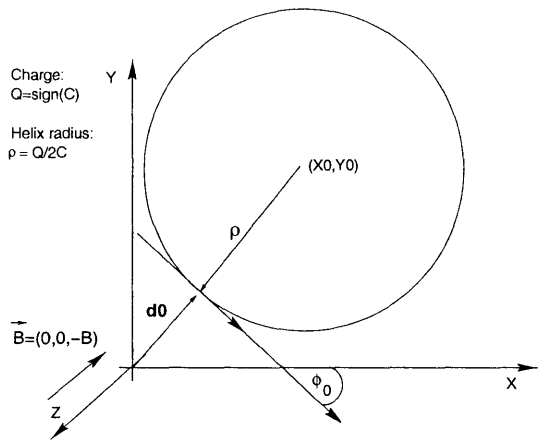

Figure 3-16: Illustration of 2D tracking parameters

Track Parameters

Tracks at CDF are described by helices. The five track parameters used in CDF are: curvature C, distance of closest approach or impact parameter $d0$, the ϕ coordinate at the point of closest approach $\phi 0$, the z coordinate at the point of closest approach $z0$ and the angle in the r-z-plane $\cot\theta$. Three of these parameters (C, $d0$, $\phi 0$) describe the location of a circle in 2 dimensions as illustrated in Figure 3-16. The five track parameters relate to the momentum components as follows:

$$\begin{aligned} p_T &= \frac{s}{C}, \\ p_x &= p_T \cdot \sin\phi 0, \\ p_y &= p_T \cdot \cos\phi 0, \\ p_z &= p_T \cdot \cot\theta. \end{aligned}$$

Track Reconstruction

The reconstruction starts with pattern recognition in the COT [60]. Two algorithms are deployed: Segment Linking (SL) [61] and Histogram Linking (HL). Segment linking starts with the construction of 3-hit seeds in each axial superlayer. The seed hits are fit to a straight line. Defined by this line more hits within the superlayer are added inside a given roadsize. Segments are linked by a simple circle fit. Once an $r - \phi$ estimate is established, stereo information is added and a final helix fit performed.

Histogram linking starts with a parameter estimate from the segment position. The three points formed by the segment, the beam line and the hit position are translated into a radius. The resulting radius is histogrammed for all hits in question. Hits along the track form a populated bin in the histogram. Tracks found by both SL and HL algorithms are matched.

The COT tracking is followed by "Outside-In" silicon tracking [62]. The COT measurement is extrapolated from the outside in towards the inner silicon detectors. As the progressive fit proceeds, r-ϕ hits are added along the way [61]. At each silicon layer the road size is evaluated based on the track error matrix. At each step the error matrix is updated to incorporate multiple scattering in the material encountered. Once all r-ϕ silicon layers have been considered, 3D hit information is added.

Muon Reconstruction

Muon reconstruction proceeds, once the prerequisite tracking is complete [63]. The first step translates the raw drift chamber information into hit coordinates. In the second step hit pairs from singly separated layers are used to form line segments with slope and intercept. Hits found in a road around the line segments are added. Once a minimum of three aligned muon chamber hits are found, an iterative fit incorporating the drift model returns the final parameters of this trajectory. Such a short trajectory is called a stub.

In the next step stubs are linked to tracks. The chosen procedure ensures, that a stub is never associated with more than one track. All tracks above 1.3 GeV are

extrapolated to the radius of each stub. If the intercept difference between track and stub is below a specified criterion, the track is added to the candidate list of the stub. The quality criterion is set to 30 cm for CMU and CMP. The criterion is 50 cm for the CMX system. After all tracks have been processed, the track candidate with the best quality criterion is found from the list for each stub. The stub-track combination with the best quality criterion of all stubs is chosen as a muon candidate. Stubs from other muon systems associated with the same track are added to the muon candidate. Stubs and tracks successfully assigned to a muon candidate are removed from the remaining candidate list and the arbitration is repeated.

Monte Carlo Simulation

Monte Carlo simulations allow to study complex phenomena. The acceptance of a complicated detector geometry for example is very hard to calculate analytically, but almost trivial to obtain from a Monte Carlo simulation.

The starting point for the simulations used here is the generation of a heavy hadron and its four momentum. The program Bgenerator [64, 65] with an NLO input spectrum is used [66].

The hadrons are decayed using the QQ decay routines [67].

The CDF detector geometry is modeled using the GEANT package [68]. The GEANT framework tracks particles in small steps. At each step the probability of an interaction is calculated. The deposited energy is converted into a simulated response of the detector electronics. The output of the simulation is a data structure of raw detector banks, similar as in data. Simulated and real data events are reconstructed with the same program.

A database keeps track of time dependent dead and noisy detector channels in real data. The realistic simulation framework [69] makes this information available in the hit generation of the silicon vertex detectors.

Chapter 4

Analysis

4.1 Data sample

The data used for this analysis are collected with the J/ψ-triggers described in the following Section 4.1.1. Data taken during runs 138425 through 168889 are used. The total luminosity of this data sample is 220 pb^{-1}.

4.1.1 Trigger Paths

Triggering at CDF is organized into 3 trigger levels. Each level reduces the incoming event rate further. A trigger path consists of a fully defined sequence of Level 1, Level 2 and Level 3 triggers.

Level 1

The di-muon trigger requires two muon stubs at Level 1. A muon stub is a short trajectory formed by hits in the muon chambers. Muon systems considered are Central MUon chambers (CMU) and Central Muon eXtension (CMX). A small fraction enters over a high p_T trigger requiring a stub in CMU and subsequently a confirmation in the Central Muon uPgrade (CMP). The CMP is located radially after the CMU behind a steel absorber. The stubs are matched in the eXTRaPolator module (XTRP) to a track from the eXtremely Fast Tracker (XFT). For CMU muons

a p_T cut of 1.5 GeV/c is applied on the matched XFT track. This cut is set to 2 GeV/c for CMX and to 6 GeV/c for CMP muons. In the L1_TWO_CMU1.5_PT1.5 and L1_CMU1.5_PT1.5_&_CMX1.5_PT2_CSX path the two XFT tracks are required to be of opposite charge.

Level 2

All Level 1 di-muon triggers are currently accepted at Level 2.

Level 3

Each Level 1 path serves as input for several Level 3 triggers. The correspondence between Level 1 and Level 3 triggers is summarized in Table 4.1.

Common to all paths is an opposite charge confirmation for the two muon tracks and a cut on the z_0 difference of 5 cm between the two muon tracks. On CMU muons a matching cut of 30 cm between the stub and track intercept is applied. This matching cut is relaxed to 50 cm for CMX muons and tightened to 15 cm for CMUP muons. These adjustments take into account the worse resolution of the CMX and the higher momentum threshold due to the CMP. For tracks associated with a CMU muon a transverse momentum cut of 1.5 GeV/c is applied. On the CMX and CMUP tracks this cut is raised to 2 GeV/c and 4 GeV/c respectively. With the exception of the ALLPHI path the phi opening angle between the two muon tracks is required to be less than 2.25 rad. A coarse di-muon mass window of $2.7 - 4.0$ GeV/c^2 is applied. For the HIGHPT path the mass window is widened to $2.0 - 5.0$ GeV/c^2. The HIGHPT path places an additional requirement on the vector sum of the transverse momenta to be greater than 9 GeV/c

A subset of path L3_JPSI_CMUCMU called L3_JPSI_CMU2CMU1.5 is used for monitoring purposes. This trigger tightens the mass window to $2.9 - 3.3$ GeV/c^2, adds an opening angle cut of 2.25 radians and raises the transverse momentum cut to 2 GeV/c on one muon leg.

In this analysis all 8 Level 3 J/ψ-trigger path are used.

Table 4.1: List of trigger path contributing to the J/ψ-dataset.

Level 1	Level 3
L1_TWO_CMU1.5_PT1.5 (2 CMU stubs matched to 1.5 GeV/c XFT track)	L3_JPSI_CMUCMU L3_JPSI_CMUCMU_ALLPHI L3_JPSI_CMUCMU_HIGHPT
L1_CMU1.5_PT1.5_&_CMX1.5_PT2_CSX (1 CMU stub matched to a 1.5 GeV/c XFT track 1 CMX stub matched to a 2 GeV/c XFT track)	L3_JPSI_CMUCMX L3_JPSI_CMUCMX_ALLPHI L3_JPSI_CMUCMX_HIGHPT
L1_CMUP6_PT4 (1 CMU stub matched to a CMP stub matched to 4 GeV/c XFT track)	L3_JPSI_CMUPCMU L3_JPSI_CMUPCMX

4.1.2 Production

After raw data are written to tape, they undergo a more complete reconstruction. When compared with the online reconstruction a Level 3 updated calibrations and alignments are available and more time consuming algorithms can be used. This reconstruction is referred to as production. During production pattern recognition is performed and tracks are reconstructed. A track is matched offline to stubs in the appropriate muon systems. The data used here are processed with production version 4.8.4a. These reprocessed data form the CDF datasets jbot0h, jpmm08 and jpmm09. The datasets contain runs 138425 through 168889. During reprocessing of runs 152595-154012 in dataset jbot0h faulty alignment and calibration constants are used. These data are referred to as bad alignment period. Files in jbot0h from this bad alignment period are replaced by the corrected versions in jpmm09.

4.2 Candidate Reconstruction

A user analysis program reconstructs the decay modes of interest. The CDF software version used in this analysis is 4.11.2. We start be describing the reconstruction steps common to all signals and conclude with detailed cut descriptions for each signal

mode: $\psi(2s) \to J/\psi\pi\pi$, $B^{\pm} \to J/\psi K^{\pm}$, $B^0 \to J/\psi K^{*0}$, $B_s^0 \to J/\psi\phi$, $B^0 \to J/\psi K_s^0$, $\Lambda_b \to J/\psi\Lambda$.

Here the high statistics mode $\psi(2s) \to J/\psi\pi\pi$ serves as a control sample for $B^0 \to J/\psi K^{*0}$, $B_s^0 \to J/\psi\phi$ with a common 4-track decay topology as seen in Figure 4-1. The $\psi(2s)$ is very precisely measured and therefore ideal to evaluate systematic uncertainties.

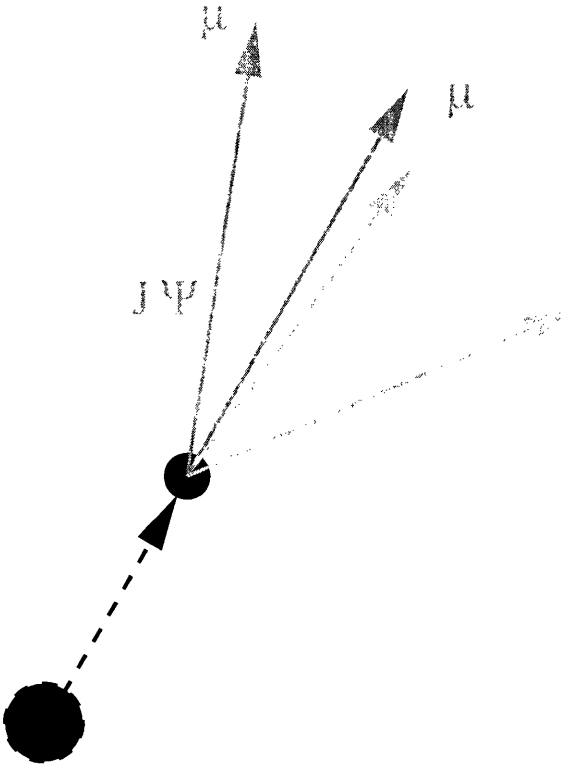

Figure 4-1: A diagram of the 4 track decay topology for the decays $B_s^0 \to \mathrm{J}/\psi\phi$, $\phi \to K^-K^+$, $B^0 \to \mathrm{J}/\psi\mathrm{K}^{*0}$, $\mathrm{K}^{*0} \to K^+\pi^-$ and $\psi(2s) \to \mathrm{J}/\psi\pi\pi$. The J/$\psi$ decays into $\mu^-\mu^+$.

The mode $B^0 \to J/\psi K_s^0$ is used as cross check for the typologically similar $\Lambda_b \to J/\psi\Lambda$ decay. Both modes contain a long-lived neutral particle decaying into two tracks as shown in Figure 4-2. We refer to such a particle in the further text as V^0 [70, 71].

In general we correct the original tracks for energy loss. The correction procedure is described in Section 4.2.1. Tracks originating directly from the decay of a particle

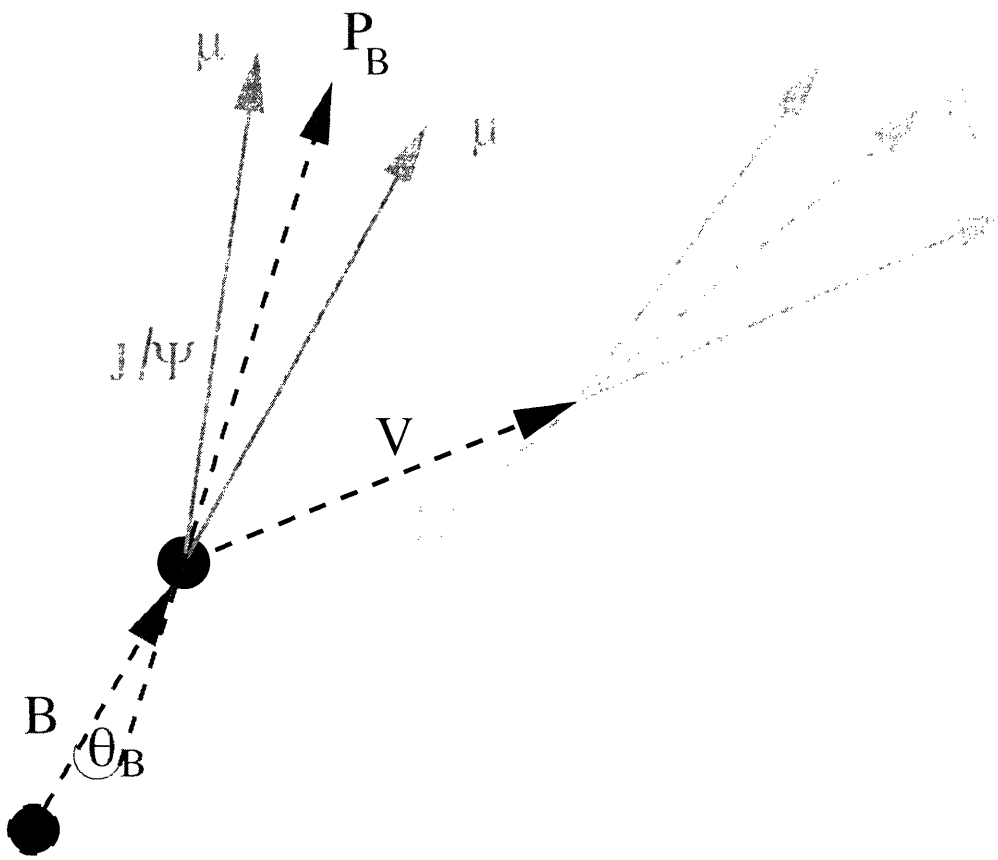

Figure 4-2: A diagram of the decay topology. A b-hadron is decaying into a J/ψ and a V^0 particle. P_B and P_V are the reconstructed momenta in 2D of the b-meson and V^0. The angles θ_B and θ_V are taken between the vertex and momenta directions of the b-meson and V^0. The definition of the angles θ_B and θ_V is given in the text.

come from a common vertex. We use this additional information to improve our mass resolution by constraining these tracks to a common vertex. This vertex fitting procedure is described in Section 4.2.2.

4.2.1 Track Preparation

The track refit is the final tracking operation after pattern recognition in the drift chamber and silicon. Refitting starts with the track parameters from the drift chamber as precursor. The fit proceeds from the outside in towards the detector center. In each step the measurements from the attached silicon hits are added, track parameters are corrected for energy loss and the error matrix is updated for multiple scattering.

There are two reasons to refit a track: correction for energy loss and improved detector alignment. The alignment used is accessed via the database tag ofotl_prd_read 100030 1 GOOD. Hits from Intermediate Silicon Layer (ISL) and Layer00 are dropped. In the standard reconstruction, each track is refit with a pion hypothesis. We use TrackRefitter [72] with the G3X option to refit each track with the corresponding particle hypothesis, as energy loss depends on the assigned mass.

The G3X option uses the G3XIntegrator [73] to incorporate material at each step. The G3XIntegrator uses the GEANT engine [68] to track particles through the CDF detector geometry description.

A refit starts with COT track parameters and error matrix. A successful refit therefore relies on a well measured track. We apply track quality cuts requiring ≥ 20 axial hits and ≥ 16 stereo hits in the Central Outer Tracker (COT). The elements of the initial track covariance matrix are rescaled using the accepted default method CorCotTrack [74] which is hidden in TrackRefitter. This procedure is necessary to correct for multiple scattering effects in the drift chamber volume.

Tracks from the COT are also corrected for energy loss in the drift chamber volume, using the corrCOTEloss method in TrackRefitter. This correction has no influence on the mass measurement. The energy loss in the COT can be simply absorbed into the material layer. The effect is accounted for separately in order to allow a correct estimate of the missing material.

4.2.2 Vertex Fit

We improve the mass resolution and signal to background ratio by exploiting knowledge about the topology of the decay. Requiring tracks to intersect at a given point imposes constraints on the track parameters. A χ^2 fit to the vertex and track parameters satisfying these constraints is performed, minimizing the shift with respect to the measured parameter values.

If the natural width of a particle is small compared to the detector mass resolution, we can constrain the combined mass of tracks resulting from the decay of this particle to its mass. Typical candidates for a mass constraint are the J/ψ, K_s^0 and Λ. Particles with a measurable width like the ϕ and K^{*0} are left unconstrained.

Further constraints can be helpful. Lets consider the topology shown in Figure 4-2. A b-hadron decays into a J/ψ and a V^0 particle. The reconstructed momentum direction of the V^0 at the V^0 vertex should point to the J/ψ-vertex. A pointing constraint requires, that the vector sum of tracks at the V^0 vertex points to a specified origin vertex. We apply a 3D pointing constraint in the reconstruction of b-decays into K_s^0 and Λ.

We use the CTVMFT [75] package to fit our tracks to a common vertex. In order to ensure good vertex quality, 3 or more silicon hits are required on all tracks. Tracks that form a V^0 need special treatment and are exempt from this requirement. We describe details in Section 4.2.3.

4.2.3 V^0 reconstruction

Due to the high displacement of V^0 tracks, in general they will not intersect all layers of silicon. This has two consequences, first requiring a large number of silicon hits, will reduce the efficiency and bias the reconstruction. Second, the energy loss correction will be overestimated, as in reality the tracks have passed through less material. The silicon hit requirement is dropped on V^0 candidate tracks. An estimate of the radial V^0 vertex location is obtained before energy loss corrections. The radial vertex location is used as stop radius for the material integration.

4.2.4 J/ψ Selection

All our signals originate from the J/ψ-trigger discussed previously in Section 4.1.1. We start our reconstruction with a refined J/ψ-selection.

- p_T of each track > 1.5 GeV/c
- muon quality cuts: CMU stub matching $\chi^2_{xpos} < 9$
- track quality cuts: > 2 Si-rϕ-hits
- vertex quality cut: converged vertex fit
- J/ψ-mass within 80 MeV/c^2 of PDG value [12]

4.2.5 Candidate Selection

We describe the kinematic cuts applied to enrich the signal. They follow closely the selection used in lifetime analysis [76] [77]. In addition we exploit the long b lifetime with a decay length L_{xy} cut. The decay length L_{xy} is defined as the difference between secondary and primary vertex projected onto the b-hadron flight direction as shown in Figure 4-3.

$\psi(2s) \rightarrow J/\psi\pi\pi$

The $\psi(2s) \rightarrow J/\psi\pi\pi$ decay serves as a high statistics control sample with a similar 4-track decay topology as B_s and B^0 decays.

The transverse momentum of the pions is required to be greater than 400 MeV/c We require 3 or more silicon r $-$ ϕ hits on all tracks. A cut of 0.1% is placed on the vertex fit probability in 2D. As the di-pion mass peaks towards the kinematical threshold, we apply a mass window of $310-610$ MeV/c^2. A $\psi(2s)$ transverse momentum cut of 6.5 GeV/c assures the similarity with the b-modes. This cut also improves the smoothness of the background, allowing to use a simple quadratic description.

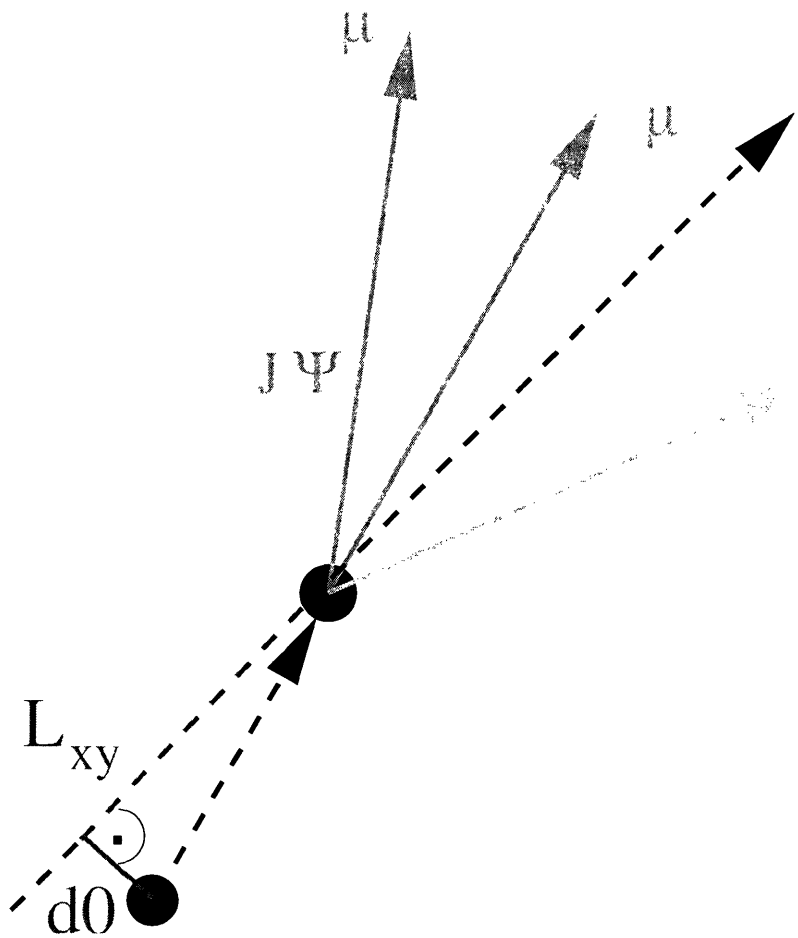

Figure 4-3: A diagram of the 3 track decay topology, exhibited by $B^{\pm} \rightarrow \mathrm{J}/\psi\mathrm{K}^{\pm}$ decays. A b-hadron is decaying into a J/ψ and another charged particle. The J/ψ decays into $\mu^{-}\mu^{+}$.

$B^{\pm} \rightarrow J/\psi K^{\pm}$

The $B^{\pm} \rightarrow J/\psi K^{\pm}$ is the highest statistics sample of fully reconstructed $B \rightarrow J/\psi X$ decays available. We require 3 or more silicon r $-$ ϕ hits on all tracks. The 3 track vertex fit is required to have a 2D probability above 0.1%. On the kaon track we impose a 2 GeV/c transverse momentum requirement. We place a cut of 100 μm on the decay length of the B-meson. A cut on B-meson transverse momentum of 6.5 GeV/c is imposed.

$B^0 \rightarrow J/\psi K^{*0}$

The K^{*0} is reconstructed in the $K^{*0} \rightarrow K^{\pm}\pi^{\mp}$ mode. The transverse momentum of pions and kaons is required to be greater than 400 MeV/c We require 3 or more silicon r $-$ ϕ hits on all tracks. The 4 track vertex fit is required to have a 2D probability above 0.1%. A cut on B-meson transverse momentum of 6.5 GeV/c is imposed. We place a cut of 100 μm on the decay length of the B. A 80 MeV/c^2 mass window around the PDG K^{*0} mass [12] is applied. This cut takes the large natural K^{*0} width into account. The momentum of the K^{*0} candidate is required to exceed 2 GeV/c

$B_s^0 \rightarrow J/\psi\phi$

The ϕ is reconstructed in the $\phi \rightarrow K^+K^-$ mode. The transverse momentum of the kaons is required to be greater than 400 MeV/c We require 3 or more silicon r $-$ ϕ hits on all tracks. The 4 track vertex fit is required to have a 2D probability above 0.1%. A cut on B-meson transverse momentum of 6.5 GeV/c is imposed. We place a cut of 100 μm on the decay length of the B-meson. On the ϕ candidate we impose a 10 MeV/c^2 mass window around the PDG mass [12]. The K^-K^+ mass distribution is shown in Figure 4-4. The momentum of the ϕ candidate is required to exceed 2 GeV/c

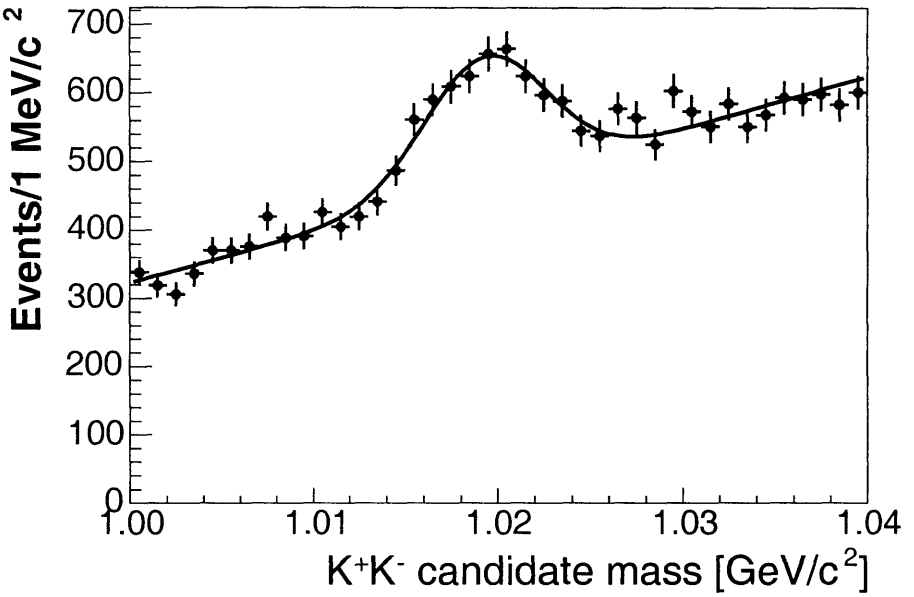

Figure 4-4: The K^+K^- mass distribution for B_s^0 candidates.

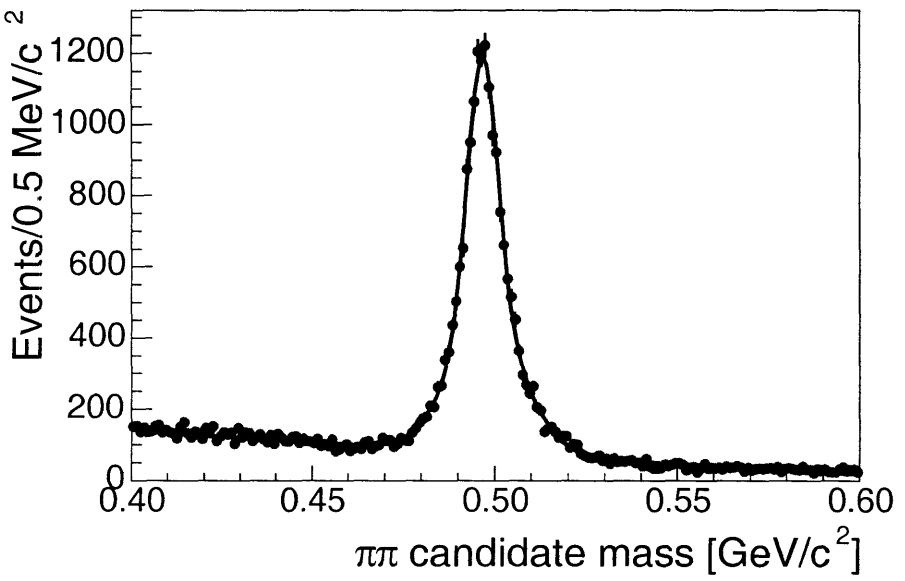

Figure 4-5: The $\pi^+\pi^-$ mass distribution for B^0 candidates.

$B^0 \to J/\psi K_s^0$

The K_s^0 is reconstructed in the $K_s^0 \to \pi^+\pi^-$ mode. The transverse momentum of the pions is required to be greater than 400 MeV/c We require 3 or more silicon r $-$ ϕ hits only on the muon tracks. We do not require silicon r $-$ ϕ hits only on the K_s^0 daughters. The 4 track vertex fit is required to have a 2D probability above 0.1%. We place a cut of 100 μm on the decay length of the B-meson and a cut of 5 mm on the K_s^0 decay length. On the K_s^0 candidate we impose a mass window from 460 MeV/c^2 to 540 MeV/c^2. The $\pi^-\pi^+$ mass distribution is shown in Figure 4-5. A cut on B-meson transverse momentum of 6.5 GeV/c is imposed.

A powerful cut for decays of long-lived V^0's is the requirement that the V^0 momentum vector points along the line of the vertex difference between V^0 and J/ψ. It can be easily expressed by a cut on the cosine of the angle θ_V between the two vectors. Separate fits to the V^0 and J/ψ vertex are used to evaluate these vectors. A similar cut can be formed for the angle θ_B between the B-meson momentum vector and the difference between B-meson and primary vertex. The angles are easily understood with the help of Figure 4-2. We place the pointing cuts at $\cos\theta_V > 0.99999$ and $\cos\theta_B > 0.99$. The distribution of this quantity in Monte Carlo simulation is shown in Figure 4-6.

$\Lambda_b \to J/\psi\Lambda$

The Λ is reconstructed in the $\Lambda \to p\pi$ mode. We require 3 or more silicon r $-$ ϕ hits only on the muon tracks. We do not require silicon r $-$ ϕ hits only on the Λ daughters. The 4 track vertex fit is required to have a 2D probability above 0.1%. We place a cut of 100 μm on the decay length of the b-hadron and a cut of 5 mm on the decay length of the Λ. On the Λ candidate we impose a mass window from 1.10 GeV/c^2 to 1.13 GeV/c^2. A cut on the Λ_b transverse momentum of 6.5 GeV/c is imposed. We require the transverse momentum of the proton candidate to exceed $3 * p_T(\pi)$ to reduce K_s^0 contamination. We place pointing cuts on $\cos\theta_V > 0.99995$ and $\cos\theta_B > 0.95$ described above.

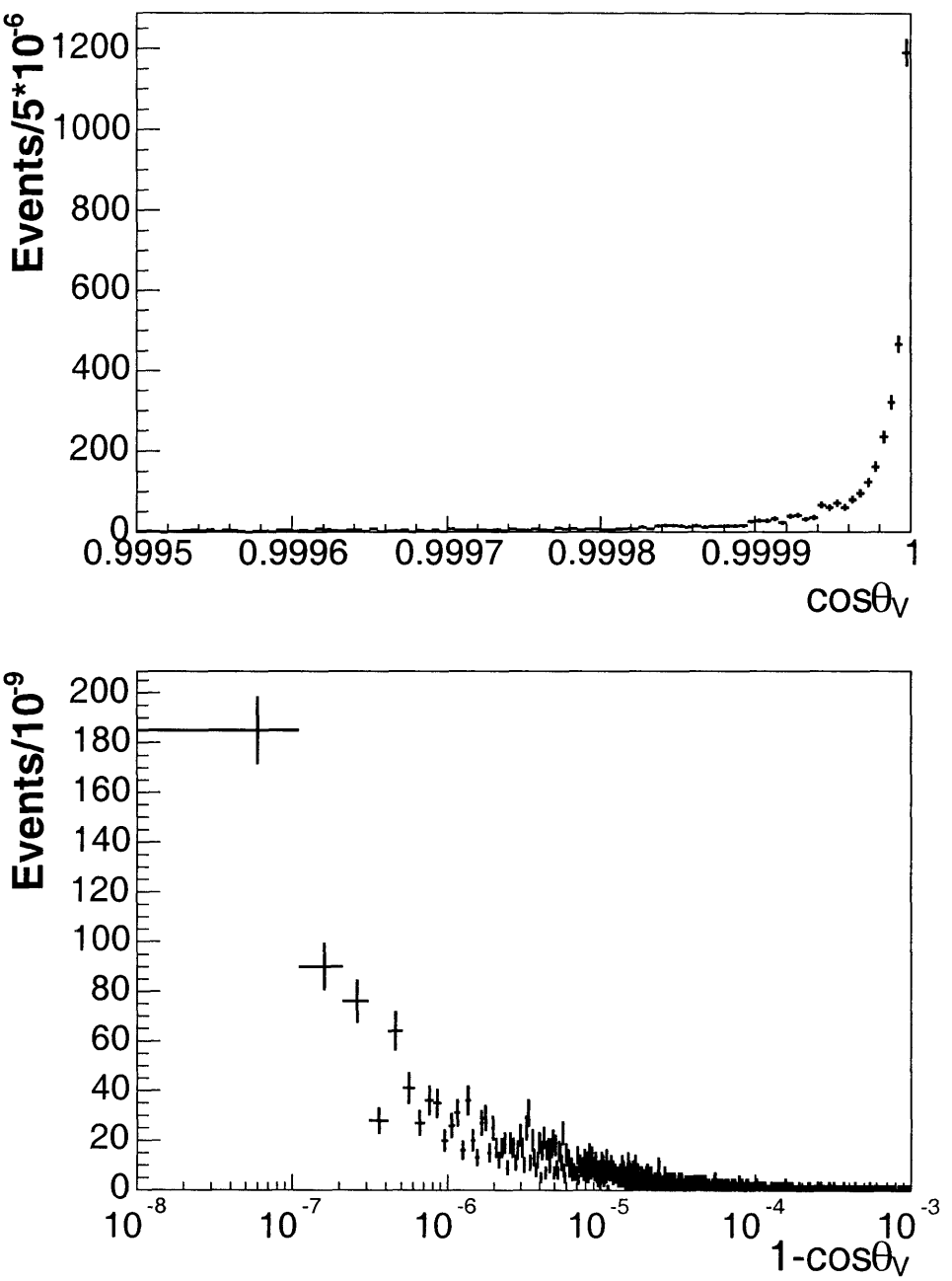

Figure 4-6: Distribution of the V^0 pointing angle in Monte Carlo simulation for the $B^0 \to \mathrm{J}/\psi \mathrm{K}^0_\mathrm{s}$ decay.

4.3 Calibration

To calibrate the momentum scale two values need to be tuned: the energy lost by a track when passing through the material in the inner detector and the strength of the magnetic field. Both quantities influence the mass and need to be disentangled.

A particles energy loss can be considered approximately constant at high momenta. The relative influence of energy loss therefore decreases as the particle momentum increases. An incorrect assignment of the energy loss results in a momentum dependence of the invariant mass. We therefore use the momentum dependence of the mass to tune the energy loss. Once the energy loss is corrected, the magnetic field scale is determined by the overall mass shift of a calibration particle with well established mass.

We use the $J/\psi \to \mu\mu$-sample to extract the correct values for energy loss and magnetic field.

4.3.1 Extraction of the J/ψ Mass

The J/ψ-meson is a narrow $c\bar{c}$ state with a width of 87 ± 5keV [12], which is far smaller than the CDF mass resolution. The width of the mass peak is therefore determined by detector effects. The detector causes a Gaussian-like smearing of the mass spectrum. Non-Gaussian tails originating from detector effects are expected to be symmetric and thus should not influence the peak position. However a radiative tail is present at the lower side of the peak due to final state Bremsstrahlung of the muons. The effect of this tail is significant and has to be taken into account in order to achieve an unbiased mass determination.

This bias has been investigated in detail from tuned a Monte Carlo Simulation in note [78]. An appropriate mixture of prompt and J/ψ-mesons from b-hadron is generated with Bgenerator [64, 65] and decayed using QQ [67] which includes a proper description of radiative decay. Detector and trigger effects are modeled with a parametric simulation [79, 80]. The mass resolution in the parametric simulation is momentum dependent and is tuned to agree with the data. The agreement is shown

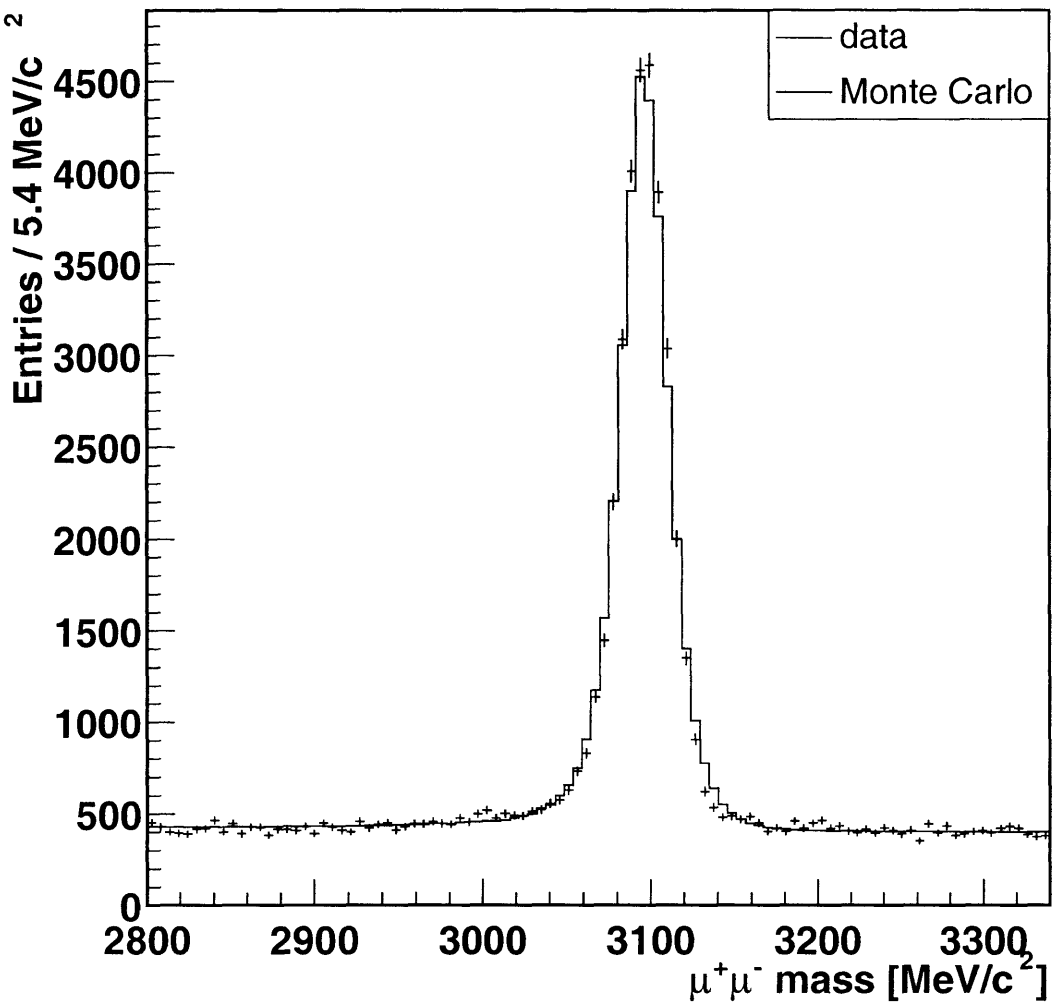

Figure 4-7: Comparison of the J/ψ mass in the parametric Monte Carlo Simulation and data. Taken from note [78].

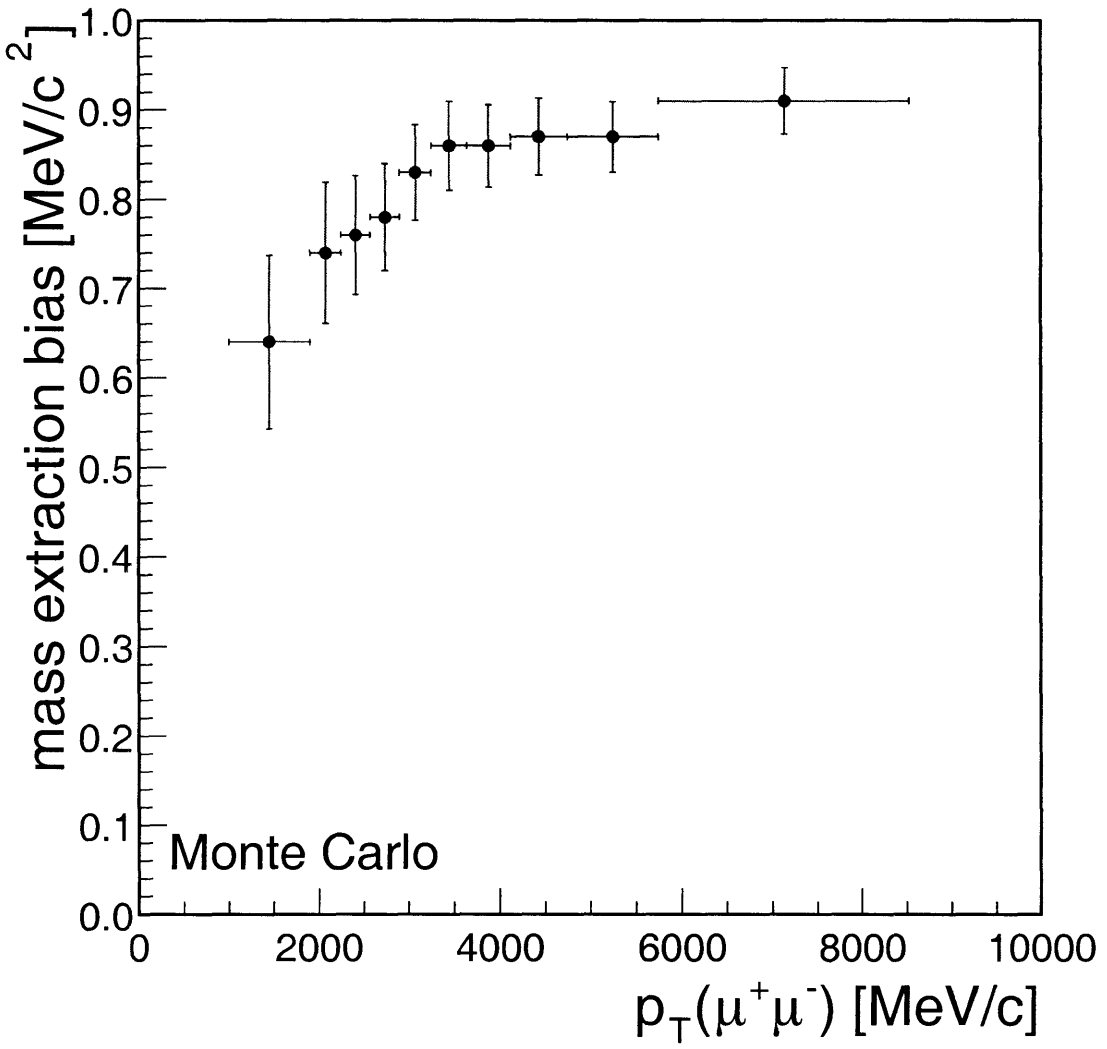

Figure 4-8: The J/ψ mass bias due to the radiative tail in single Gaussian mass fits as a function of J/ψ p_T. Taken from note [78].

in Figure 4-7.

The difference of the mean of a single Gaussian fit with respect to the input mass is taken as a bias. The bias is evaluated in bins of J/ψ P_T as shown in Figure 4-8. We correct the mass values in each transverse momentum bin by adding the bias from above.

4.3.2 Energy loss

The key to effective energy loss corrections is a proper accounting of detector material in terms of location, quantity and type. The most important part for this analysis is the implementation of passive material used in the construction of the silicon detector. Energy loss is dominated by the passive material of the silicon system. The SVX silicon sensors for example account for roughly $1.8\%X_0$ while cables already contribute up to $3\%X_0$ and silicon hybrids amount to $12\%X_0$ radiation length [81].

In order to correct for energy loss, we refit tracks according to the procedure described in Section 4.2.1.

Raw tracks show a transverse momentum dependence of J/ψ mass. The slope of this dependence is 0.90 MeV/c^2 per GeV/c as shown in Figure 4-9 by the curve in circles. Applying the default energy loss correction with the track fit, reduces the p_T dependence of the J/ψ mass to about 0.30 MeV/c^2 per GeV/c, as shown by the linear fit to the star shaped points in Figure 4-9, but a clearly measurable slope remains.

To address this deficiency, missing material is incorporated into GEANT. A thin layer of silicon is added to the geometry description at a radius of 34 cm as a real physical volume. The radius is chosen somewhat arbitrarily, but is technically limited to locations where no other detector volumes are present to avoid overlap. As a cross check, the layer is placed at 15 cm radius. No differences in behavior are found.

The thickness of this layer is tuned such that the J/ψ mass dependence in p_T is removed, as shown by the line through the triangles in Figure 4-9.

The layer material is chosen to be silicon of $2.33\frac{\text{g}}{\text{cm}^3}$ density [82]. After tuning, the thickness of the phantom layer is $(0.29 \pm 0.05(\text{stat}) \pm 0.08(\text{sys}))$ cm which corresponds

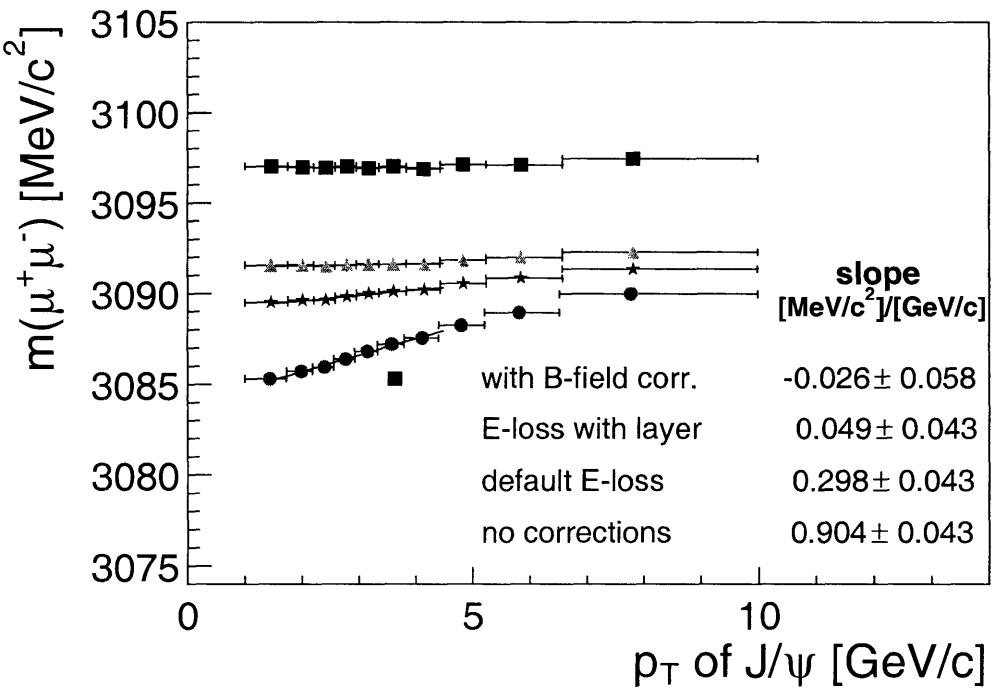

Figure 4-9: A plot of di-muon mass in the J/ψ region vs transverse momentum. The lowest curve in circles shows the slope of uncorrected tracks, the star curve above has only nominal energy loss corrections included. The middle curve in triangles shows that the slope has vanished after tuning of energy loss. The last curve in rectangles shows the final behavior after all energy loss corrections have been applied and the magnetic field scale has been adjusted.

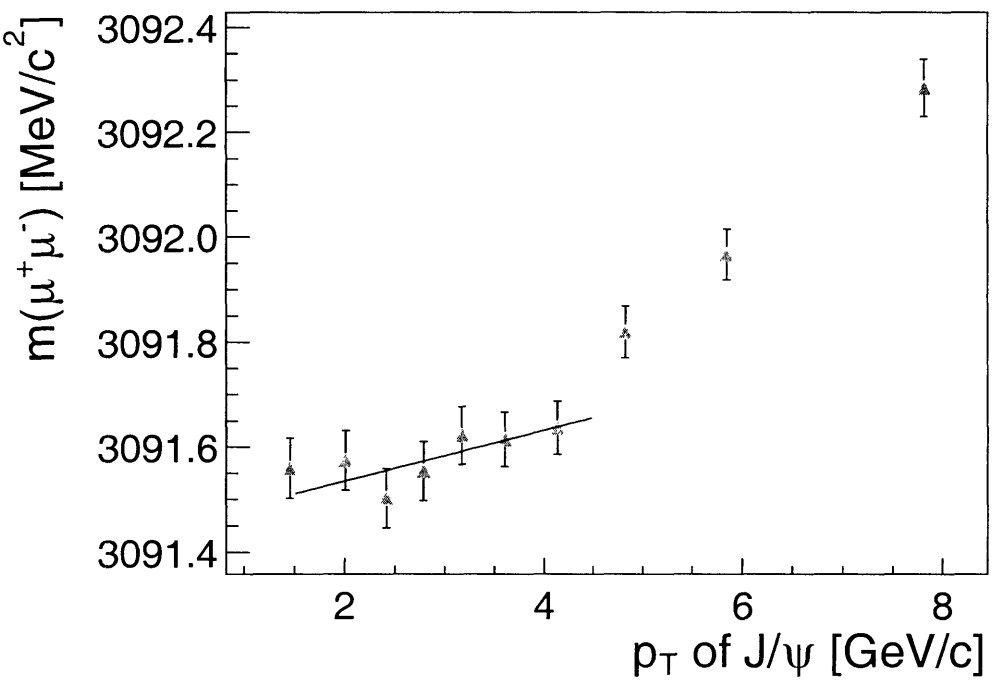

Figure 4-10: Plotted is the di-muon mass vs transverse momentum, after tuned energy loss correction. A non-linearity at high momentum is visible.

Table 4.2: The p_T dependence of the J/ψ mass after final energy loss corrections. Consult Figure 4-10

p_T fit range	$1.5-4.5$ GeV/c	$1.5-6$ GeV/c	$1.5-8$ GeV/c
offset [MeV/c^2](COT only)	3091.7 ± 0.2	3091.5 ± 0.1	3091.3 ± 0.1
slope [$\frac{\text{MeV/c}^2}{\text{GeV/c}}$](COT only)	-0.039 ± 0.058	0.035 ± 0.030	0.072 ± 0.022
offset [MeV/c^2](defTracks)	3091.5 ± 0.1	3091.3 ± 0.1	3091.2 ± 0.1
slope [$\frac{\text{MeV/c}^2}{\text{GeV/c}}$](defTracks)	0.048 ± 0.043	0.115 ± 0.021	0.133 ± 0.015

to $(0.68 \pm 0.12(\text{stat}) \pm 0.19(\text{sys}))\frac{\text{g}}{\text{cm}^2}$. The statistical uncertainty comes directly from the uncertainty on the slope returned by the fit, assuming a linear dependence between slope and layer thickness and a conversion factor of (layer at zero slope)/(slope at zero layer) $= \frac{0.29 \text{ cm GeV}}{0.30 \text{ MeV}}$. A systematic uncertainty of $\frac{-0.039-0.133}{2}\frac{0.29}{0.30}$ cm $= 0.08$ cm is assigned, taking half maximum variation of the slope as seen in Table 4.2. This quantifies two systematic effects, the inconsistency between SVX and COT tracks and the nonlinearity in the mass versus p_T plot. The nonlinearity is more apparent in Figure 4-10. Tracking systematics as investigated in Section 4.6.3 are suspected as cause.

A general cross check of the energy loss correction procedure and the effects of missing material is performed by a Monte Carlo simulation exercise previously [78].

A study of the z dependence of the invariant mass indicates where material has been over- or under-corrected. In Figure 4-11 the dependence of the J/ψ mass on the z position of the di-muon vertex is shown.

The assumption that the complete p_T dependence of the mass is due to the energy loss correction is valid only to first order. The adjustment of the magnetic field also bears a p_T dependence because the daughter particles are massive. As it turns out this effect is very small for the momentum range in question and can be quantified by the change in slope before (triangles) and after (squares) magnetic field correction as shown in Figure 4-9. No measurable slope remains after final correction.

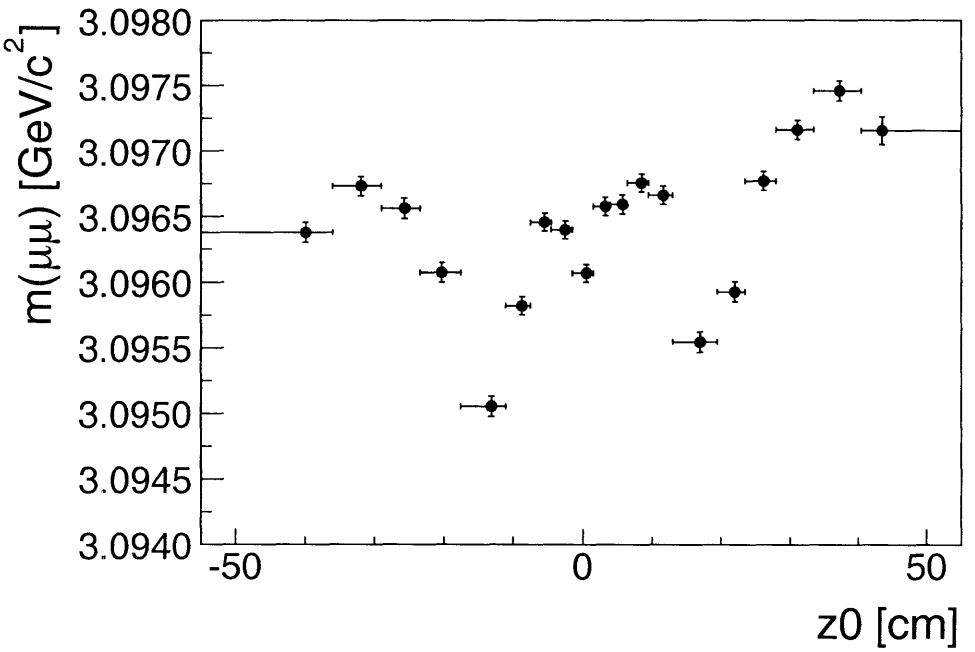

Figure 4-11: The J/ψ mass as a function of its z coordinate of the vertex, after the energy loss corrections are applied.

4.3.3 Magnetic Field

The magnetic field scale defines the translation from the track parameter curvature into momentum. The time stability and field uniformity is investigated. We determine the overall scale by adjusting the extracted J/ψ mass to its well established world average.

Time stability

The time stability of the magnetic field in the CDF tracking volume is of importance. The CDF solenoid current is regulated by a feedback loop driven by an Nuclear Magnetic Resonance, or NMR, probe which also provides a measurement of the magnetic field. The typical time interval for the feedback is in the order of a minute and the precision of the NMR is far beyond what is needed for high quality mass measurements. Because the NMR probe is itself the basis for the feedback control it cannot be used as a gauge of residual systematic variations in the magnetic field. An independent verification of the stability of the magnetic field is obtained by monitoring the position of reconstructed mass peaks over time.

The J/ψ sample provides a good starting point to verify the stability of the magnetic field. The time dependence of the energy loss and magnetic field corrected J/ψ mass is shown in Figure 4-12. Given the large statistics this test is sensitive to changes in the B-field of $\frac{0.1 \ \mathrm{MeV/c^2}}{3.1 \ \mathrm{GeV/c^2}} < 0.003\%$. The mass is constant within $\pm 0.2 \ \mathrm{MeV/c^2}$, driven by only a few variations. This variation results in a systematic uncertainty of $\frac{0.2 \ \mathrm{MeV/c^2}}{3.1 \ \mathrm{GeV/c^2}} = \pm 0.00006$ on the magnetic field scale.

Field Uniformity

The magnetic field inside the tracking volume has been measured and mapped in Run I [83, 84, 85, 86, 87]. This field map shows inhomogeneities towards the outer ends of the tracking volume. This can be seen in Figure 4-13. If left uncorrected, these deviations would result in shifts of up to 10 $\mathrm{MeV/c^2}$ on the J/ψ mass. The current CDF tracking software incorporates this map and corrects for known field deviations.

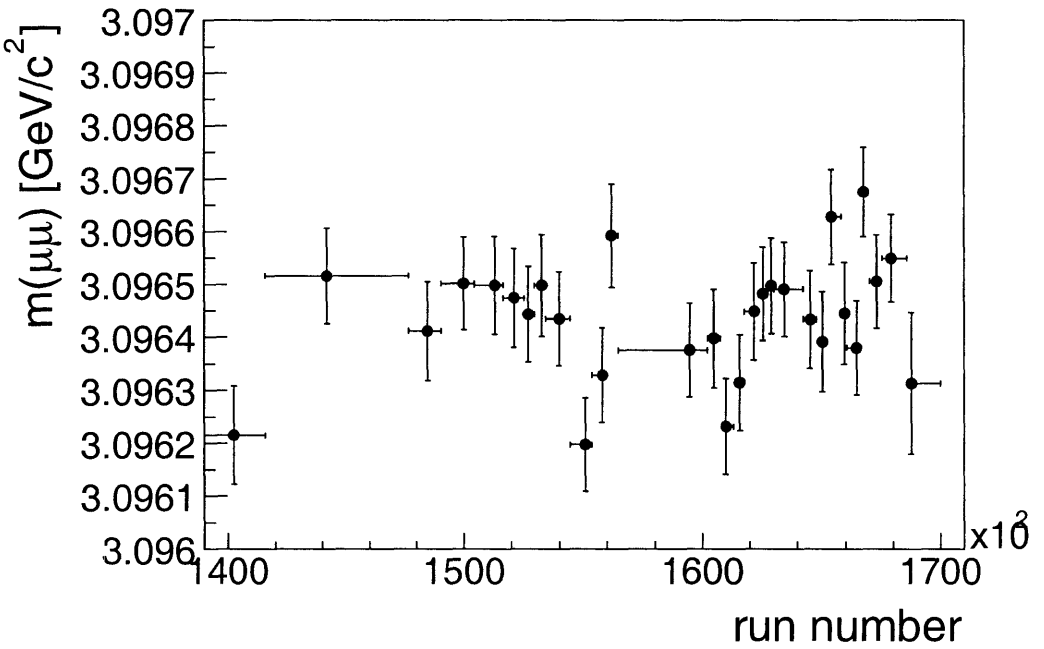

Figure 4-12: The J/ψ mass as a function of run number. It can be seen, that the mass is very stable with time.

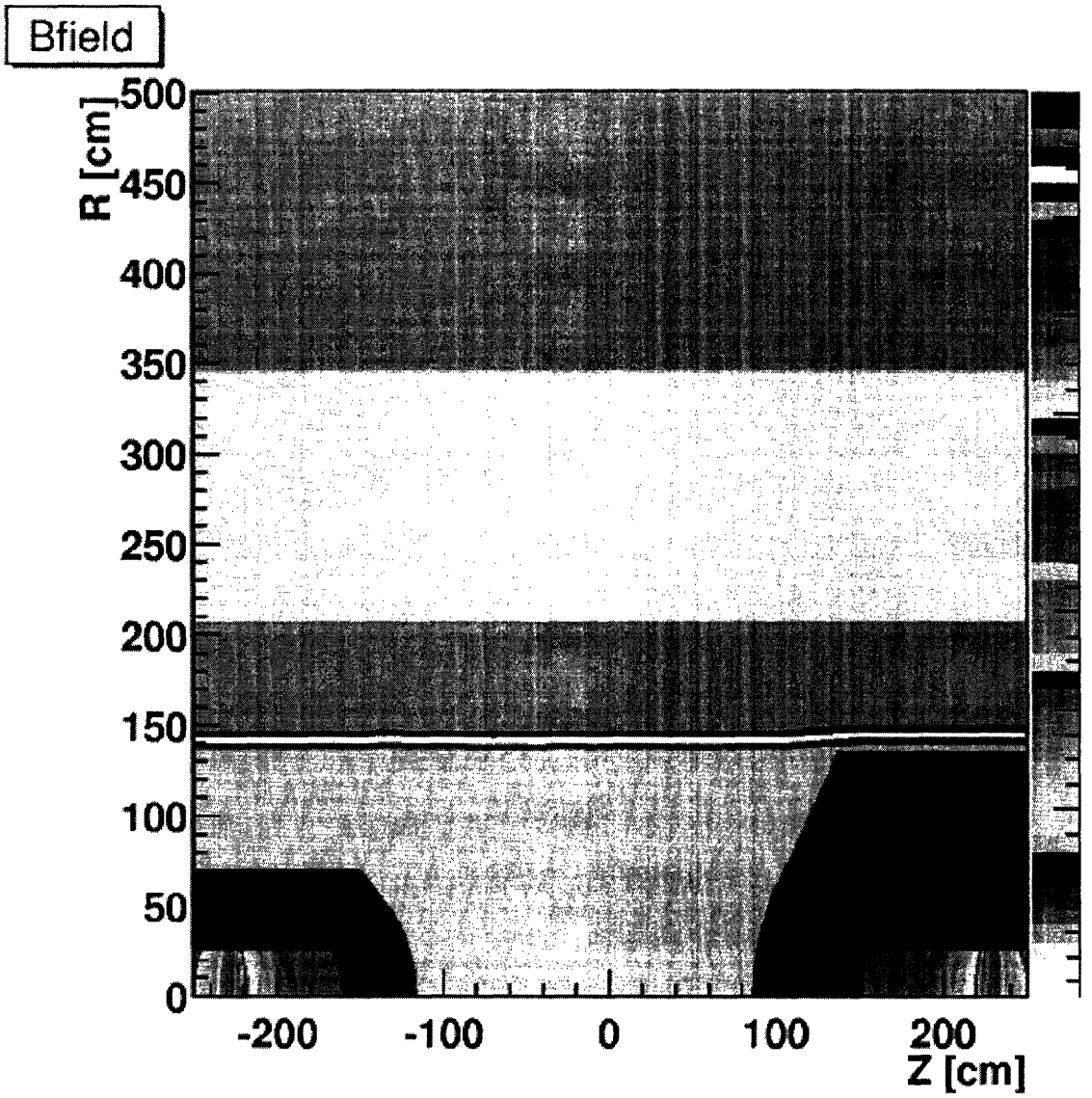

Figure 4-13: Map of the magnetic field as implemented in the Run II software. The field has been measured for Run I and is extrapolated using simulation programs. Inhomogeneities are shown at the ends of the tracking volume, which are different for the east and west end of the detector.

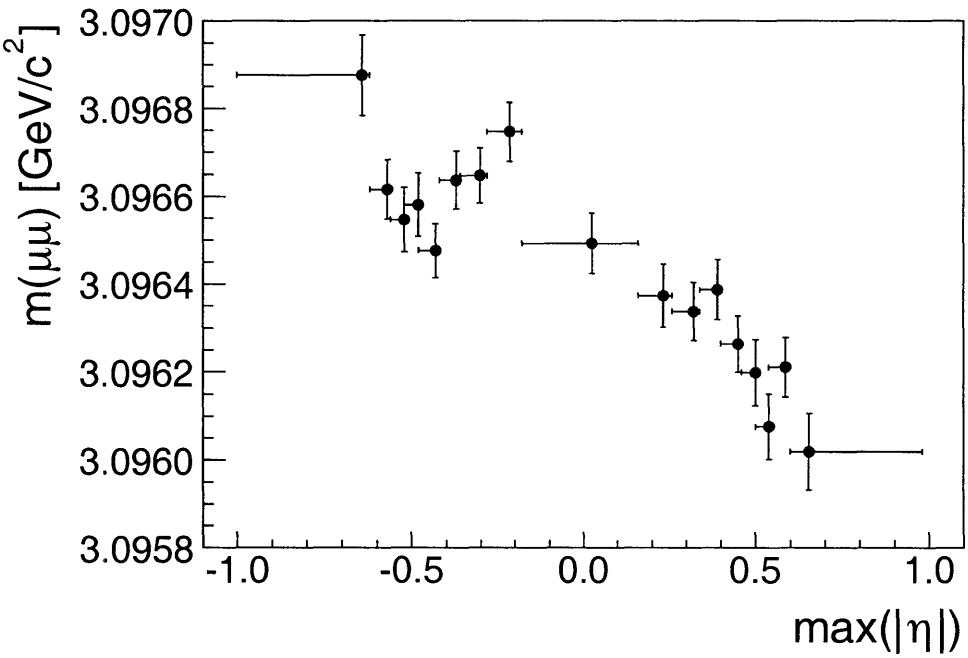

Figure 4-14: Plotted is the J/ψ mass versus the maximum absolute pseudo-rapidity η of the two daughter muons.

To check the success of the correction, the behavior of tracks in different regions of the tracking volume has to be investigated. In Figure 4-14 we examine the dependence of the J/ψ mass on maximum absolute value of the pseudo-rapidity η of the two daughter muons. A remaining variation of ± 0.4 MeV/c^2 is seen. This variation results in a systematic uncertainty of $\frac{0.4 \text{ MeV/c}^2}{3.1 \text{ GeV/c}^2} = \pm 0.00013$ on the magnetic field scale.

Table 4.3: Summary of the overall magnetic field scale factors

	mass [MeV]	correction factor
COT only	3091.7 ± 0.1	$1.00167 \pm 0.00003(stat)$
defTracks	3091.5 ± 0.1	$1.00173 \pm 0.00003(stat)$
combined	3091.6 ± 0.1	$1.00170 \pm 0.00003(stat) \pm 0.00015(sys)$

Table 4.4: Summary of the systematic uncertainties of the calibration.

effect	magnetic field scale systematic
time stability	± 0.00006
homogeneity	± 0.00013
tracking	± 0.00003
combined	± 0.00015

4.3.4 Measurement of Nominal Magnetic Field Scale

After the material has been tuned and the tracks properly corrected for energy loss, the magnetic field scale is adjusted such that the extracted J/ψ mass is scaled to its PDG value of m$(J/\psi) = 3096.87 \pm 0.04$ MeV [12]. The ratio of the measured and nominal mass is calculated to scale the magnetic field, a process which includes the radiative fitting correction as explained in Section 4.3.1. The mass values from linear p_T dependency fits in Table 4.2 are used. The region of J/ψ p_T from $1.5 - 4.5$ GeV is used. The resulting scale factors for combined and drift chamber only tracking are summarized in Table 4.3. The difference between these two scale factors is taken as

a systematic uncertainty. The combined systematic uncertainties are summarized in Table 4.4. The line through the squares in Figure 4-9 shows the behavior of the J/ψ mass after both energy loss and magnetic field corrections are applied.

4.3.5 The Υ mass: momentum scale upward

Establishing the scale in a particular kinematic neighborhood does not preclude that there are systematic variations which cause mass values to drift away from the true values as one extends into distant kinematic regimes or different decay topologies. The Υ states provide a convenient "high" mass point to monitor such possibilities.

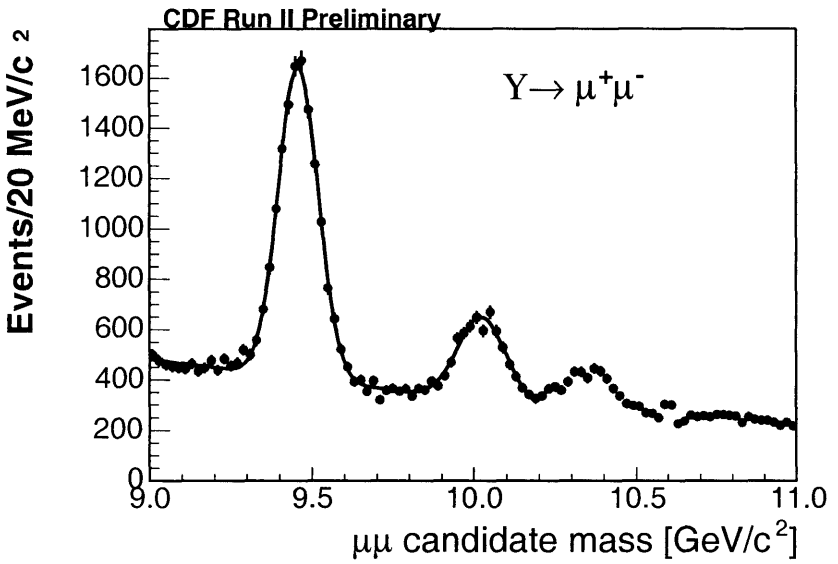

Figure 4-15: Di-muon mass distribution in the Υ and Υ' region.

The Υ decay selection is basically the same as the J/ψ selection and the resulting di-muon mass distribution is shown in Figure 4-15. The three Υ states are clearly visible, but the small statistics of the $\Upsilon(2S)$ and $\Upsilon(3S)$ states as well as their near overlap make these two states poor test cases for the mass scale. We restrict ourselves to the $\Upsilon(1S)$ state candidates, and by a single Gaussian fit we determine that the energy and magnetic field corrected mass is $9458.48 \pm 0.95\,(stat)$ MeV/c^2.

The distorting effects of the radiative bias on the mass are again investigated by creating parametric Monte Carlo simulation samples with mass resolutions that

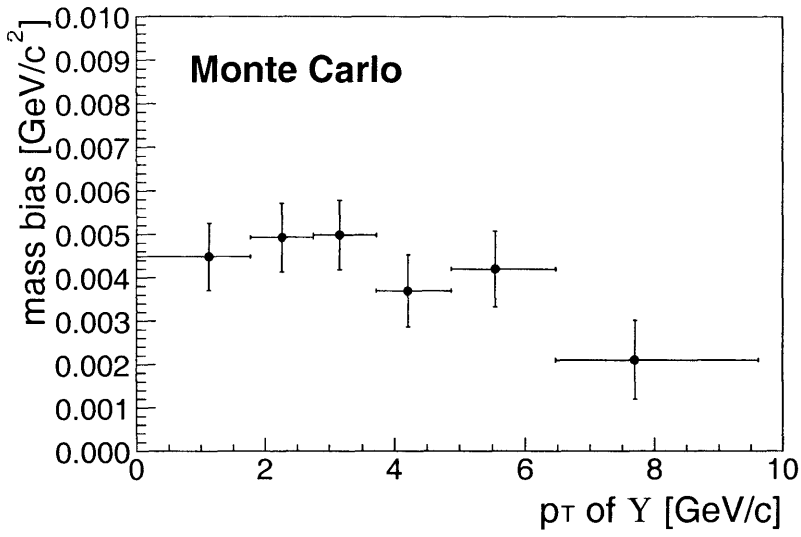

Figure 4-16: The p_T dependence of the fit bias to $\Upsilon(1S)$ mass due to radiative tail.

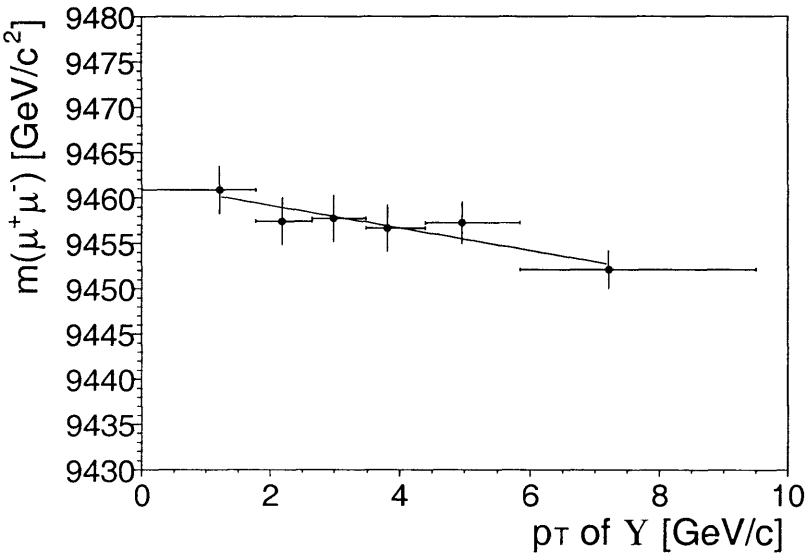

Figure 4-17: Plotted is the di-muon mass in Υ region versus p_T of the Υ, after all corrections are applied.

describe the data. The momentum dependence of this bias is shown in Figure 4-16.

Single-Gaussian fits of the $\Upsilon(1S)$ underestimate the mass by -3.74 ± 0.35 MeV/c^2, which brings our corrected value, 9462.22 ± 1.01 $(stat)$ MeV/c^2, into reasonable agreement with the PDG value of 9460.30 ± 0.26 MeV/c^2.

4.4 Mass Fitting Procedure

Once the above corrections are applied, the mass distribution for each decay under consideration is fit to obtain the central value of the mass. An unbinned log likelihood fit is used to extract the mass. We do *not* use the event-by-event estimates of the mass uncertainty from the vertex fit in the likelihood.

The likelihood function used here has the following form:

$$(1 - f_{\rm b}) \cdot S(m, x) + f_{\rm b} \cdot B(m, x) \tag{4.1}$$

The parameter f_b is the background fraction. In general the signal function S is modeled as a single Gaussian:

$$S(m, \sigma, m_{\rm fit}) = \frac{1}{\sqrt{2\pi} \cdot \sigma} \exp\left(\frac{(m - m_{\rm fit})^2}{2\sigma^2}\right) \tag{4.2}$$

The background B is modeled using a linear function L:

$$B(m, a_{\rm bgl}) = L(m, a_{\rm bgl}) = a_{\rm bgl} \cdot m + C \tag{4.3}$$

with the normalization constant C:

$$C = \frac{1 - \frac{1}{2}a_{\rm bgl}(m_{\rm max}^2 - m_{\rm min}^2)}{m_{\rm max} - m_{\rm min}},$$

The parameter $a_{\rm bgl}$ refers to the slope of the distribution. The beginning and end of the mass fitting range are denoted by $m_{\rm min}$ and $m_{\rm max}$. The fit ranges are indicated on the individual plots by the curve. For example the B_s^0 fit range is $5.1 < x <$

5.6 GeV/c^2 (Figure 4-33).

For the $\psi(2s) \to J/\psi\pi\pi$ decay a polynomial of second degree is chosen as background description.

$$B(m, a_{\mathrm{bg2}}, b_{\mathrm{bg}}) = P2(b_{\mathrm{bg}}, a_{\mathrm{bg2}}, m) = b_{\mathrm{bg}} \cdot m^2 + a_{\mathrm{bg2}} \cdot m + D \tag{4.4}$$

$$D = \frac{1 - \frac{1}{2} a_{\mathrm{bg2}} \cdot (m^2_{\mathrm{max}} - m^2_{\mathrm{min}}) - \frac{1}{3} b_{\mathrm{bg}} \cdot (m^3_{\mathrm{max}} - m^3_{\mathrm{min}})}{m_{\mathrm{max}} - m_{\mathrm{min}}},$$

This introduces one additional parameter b_{bg} for the quadratic portion. The term D is a normalization constant.

Some modes require a more detailed modeling. These functions are described later in the Section 4.4.1 below.

The underlying general framework has been used and tested extensively. Pull distributions obtained from Toy Monte Carlo fits are shown for the models used in Figure 4-18.

4.4.1 Background Contributions

In addition to combinatorial background, each mode contains background from partial and mis-reconstructed b-hadron decays. These contributions are hard to remove because they result from real b-hadron decays and exhibit the same vertex displacement as the signal. Figure 4-19 shows the $J/\psi K^{\pm}$ mass distribution after tightening the transverse momentum and decay length cuts. A clear shoulder is visible on the low mass side. The background from b-hadrons is modeled well by the Monte Carlo simulation. Therefore we can use the Monte Carlo simulation to understand the different background contributions. We use an inclusive $b \to J/\psi X$ Monte Carlo with realistic detector simulation [69]. This sample, is available as dataset mbot10.

In Figure 4-20 the background contributions of bottom decay modes reconstructed as $B^{\pm} \to J/\psi K^{\pm}$ can be seen. Two clear features are observed. Visible on the left side is a shoulder, mainly from partially reconstructed $B^0 \to J/\psi K^{*0}$ decays. Underneath the peak on the high mass side we find the Cabibbo suppressed $B^{\pm} \to J/\psi \pi^{\pm}$ mode.

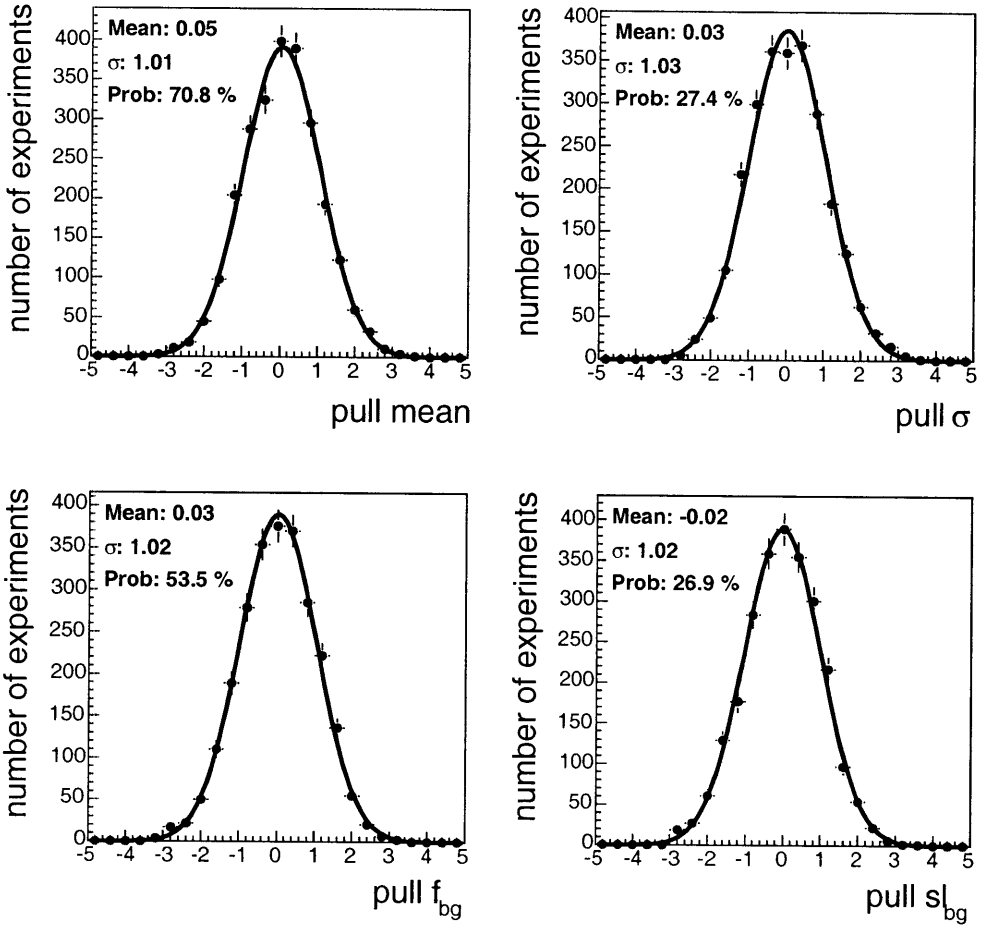

Figure 4-18: Behavior of the pulls for the unbinned log likelihood fitter. Shown are the 4 parameters of the simple linear model.

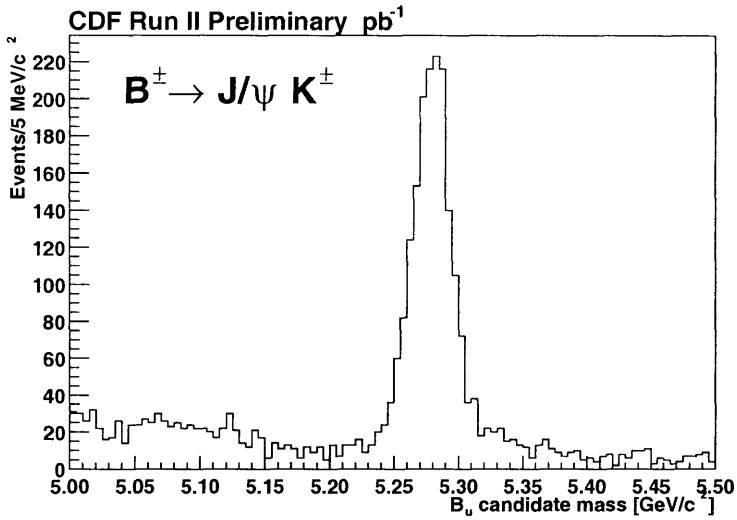

Figure 4-19: A plot of the purified B^+ sample. The decay length and momentum cuts have been tightened to $L_{xy} > 250$ μm and $p_T(B) > 8$ GeV. The remaining reflection on the low mass side is clearly visible.

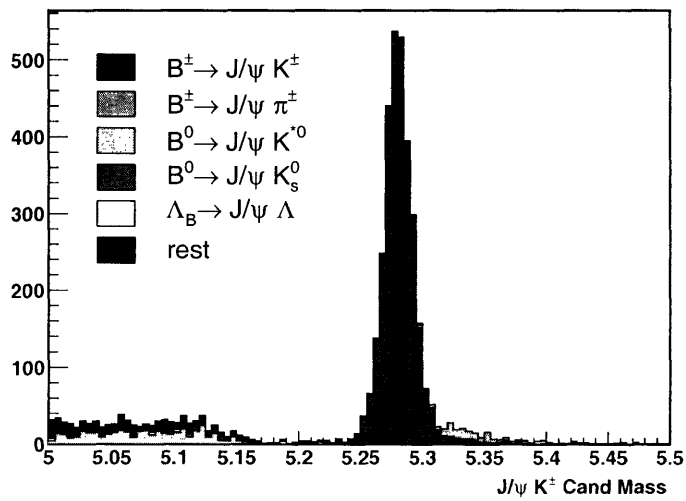

Figure 4-20: A plot of the b-hadron contributions to the reconstructed $B^{\pm} \to J/\psi K^{\pm}$ signal. Most prominent are the left shoulder from partially reconstructed $B^0 \to J/\psi K^{*0}$ decays and the $B^{\pm} \to J/\psi \pi \pm$ peak on the right.

These features are modeled as follows:

$$B(m, f_T, f_\pi, a_{\text{bgl}}) = f_T \cdot T(m, \mu_T, \sigma_T) + f_\pi \cdot B_\pi(m, \mu_\pi, \lambda_\pi) + (1.0 - f_T - f_\pi) \cdot L(m, a_{\text{bgl}}) \tag{4.5}$$

Where the function T describes the left side turn on modeled with an error function Erf:

$$T(m, \mu_T, \sigma_T) = \frac{1}{E}\left(1.0 - \text{Erf}\left(\frac{m - \mu_T}{\sigma_T}\right)\right) \tag{4.6}$$

and the $B^\pm \to J/\psi\pi$ contribution is modeled by:

$$B_\pi(m, \mu_\pi, \lambda_\pi) = \frac{1}{F} \cdot (m - \mu_\pi)^6 \cdot e^{-\frac{m-\mu_\pi}{\lambda_\pi}} \tag{4.7}$$

Here E and F are normalization constants. The parameters μ_T, σ_T, μ_π and λ_π that determine the shape characteristics are obtained from Monte Carlo simulation and fixed in the fits. The fractions f_T and f_π are left to float. The signal peak is modeled as a double Gaussian with common mean. We fix the width of the second Gaussian to the Monte Carlo simulation value. The fraction of the second Gaussian is determined by the fit. The pull distributions for this fit model are shown in Figure 4-21.

In Figure 4-22 we plot modes reconstructed as $B^0 \to J/\psi K^{*0}$. The clear second peak at the B^0 mass in Figure 4-22 comes from non-resonant $B^0 \to J/\psi K^\pm \pi^\mp$ decays and serves as additional signal. There is an additional contribution underneath the B^0 peak from reflected $B_s^0 \to J/\psi\phi$ decays visible in Figure 4-22. This contribution is easily removed by a cut on the $K^\pm\pi^\mp$ candidate mass of ± 50 MeV with respect to K^{*0} PDG mass [12]. The rest of the background contribution are well described with linear function. An additional feature in this decay mode arises, when the $K^{*0} \to K^\pm\pi^\mp$ is mis-reconstructed using the wrong kaon and pion assignment. We refer to this type of mis-reconstruction as a swap. The effect is demonstrated in the Monte Carlo simulation shown in Figure 4-24. The fraction of this type of mis-reconstructed $B^0 \to J/\psi K^{*0}$ events is 19%. The events with swapped kaon and pion assignment are described with two Gaussians. The narrow peak has a width of 21.7 MeV and

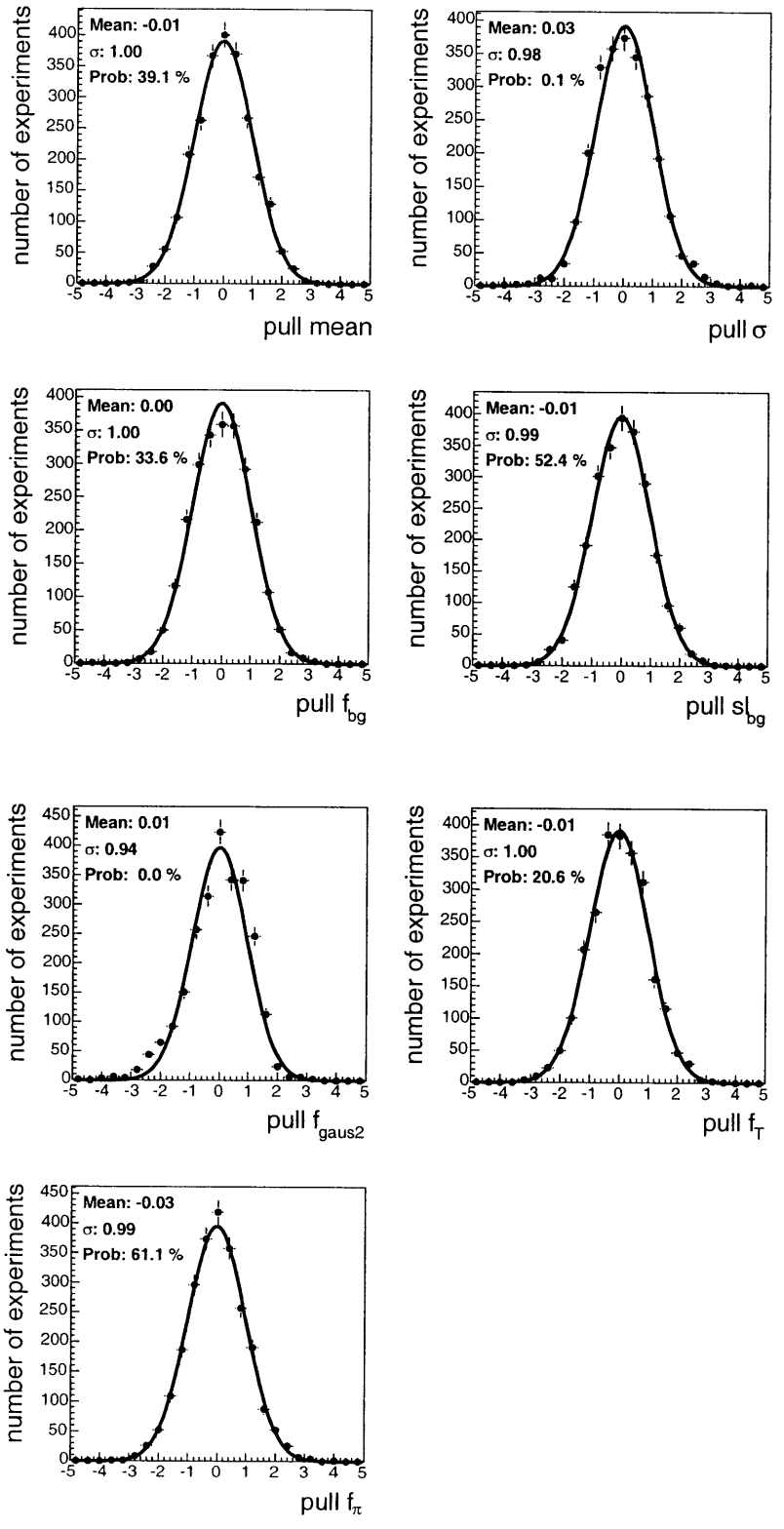

Figure 4-21: Behavior of the pulls for the unbinned log likelihood fitter. Shown are the parameters of the complex model for the $B^{\pm}$.

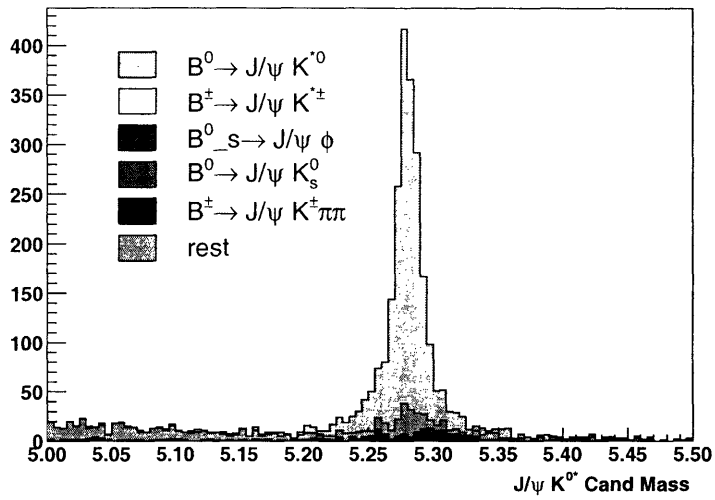

Figure 4-22: A plot of the b-hadron contributions to the reconstructed $B^0 \to \mathrm{J}/\psi \mathrm{K}^{*0}$ signal. The peak in the remaining background, results from non-resonant $B^0 \to \mathrm{J}/\psi \mathrm{K}^{\pm}\pi^{\mp}$ decays. The peak from $B_s^0 \to \mathrm{J}/\psi\phi$ decays can be removed with a stringent cut on the K^{*0} mass. A linear model is a good description for the remaining background.

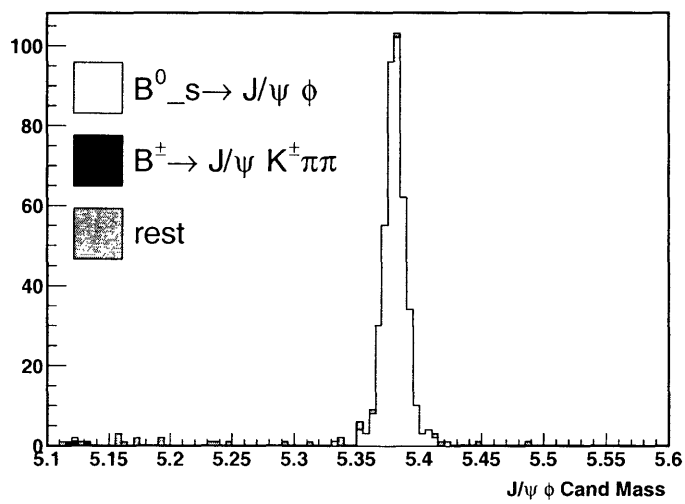

Figure 4-23: A plot of the b-hadron contributions to the reconstructed $B_s^0 \to \mathrm{J}/\psi\phi$ signal. This mode is essentially background free.

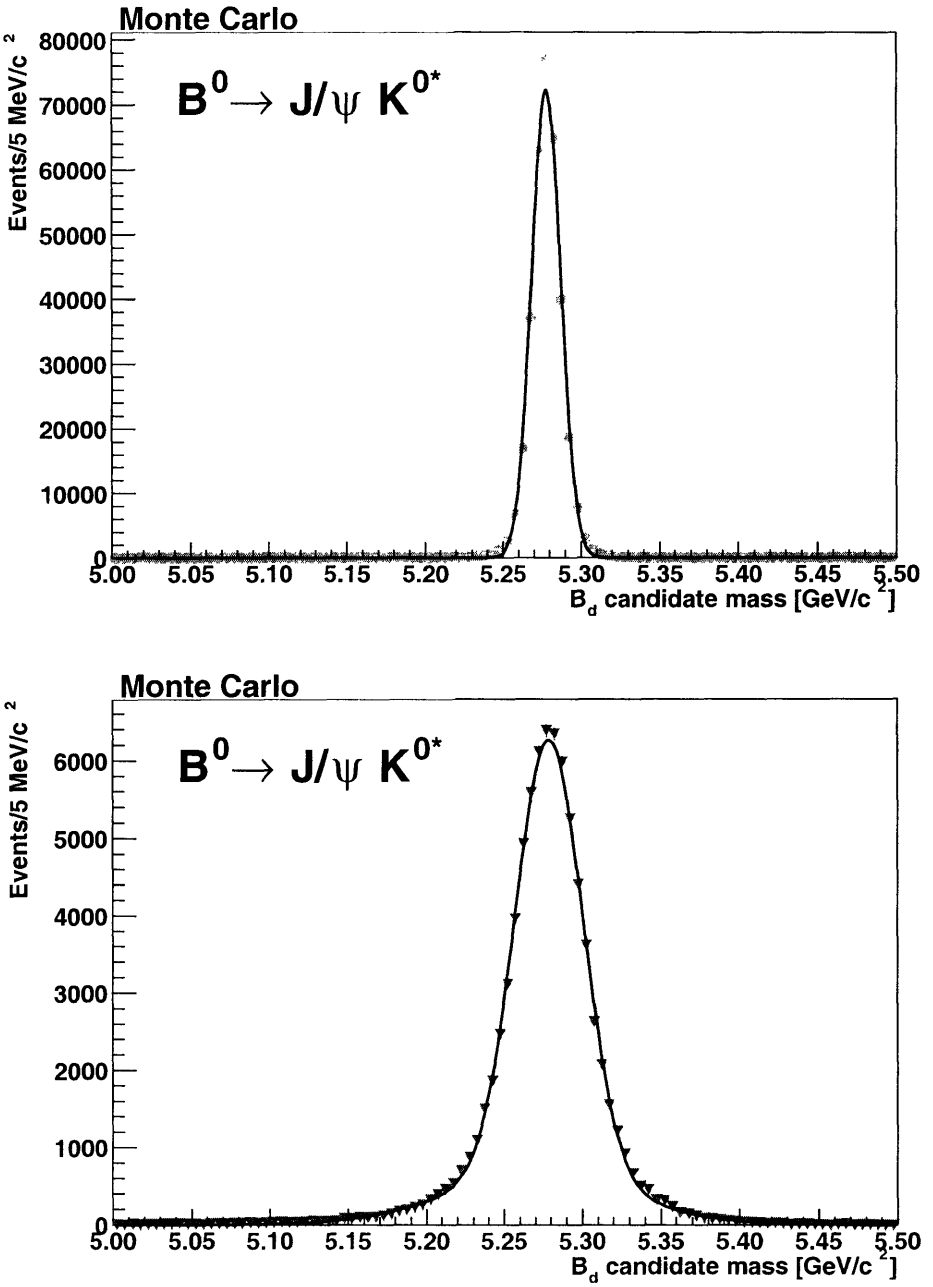

Figure 4-24: The effects of swapping K-π mass assignments in the B^0 masses reconstruction in GEANT Monte Carlo. The upper plot shows the B^0 mass distribution for the unswapped, correctly reconstructed candidates. Events with a swapped K-π mass assignment are shown in the bottom plot.

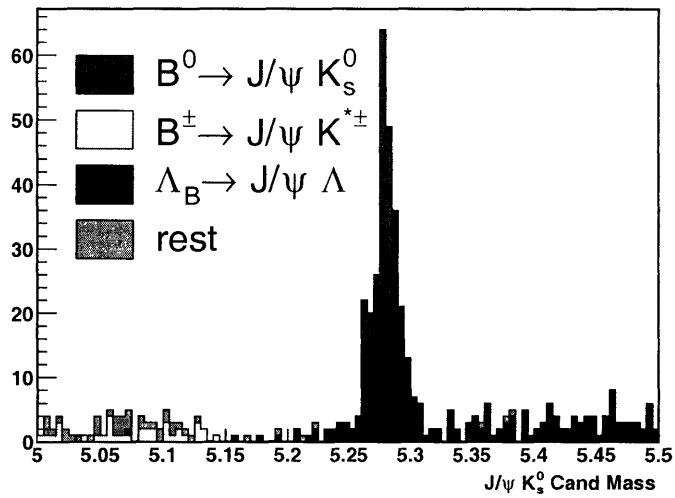

Figure 4-25: A plot of the b-hadron contributions to the reconstructed $B^0 \rightarrow \mathrm{J}/\psi \mathrm{K}^0_\mathrm{s}$ signal.

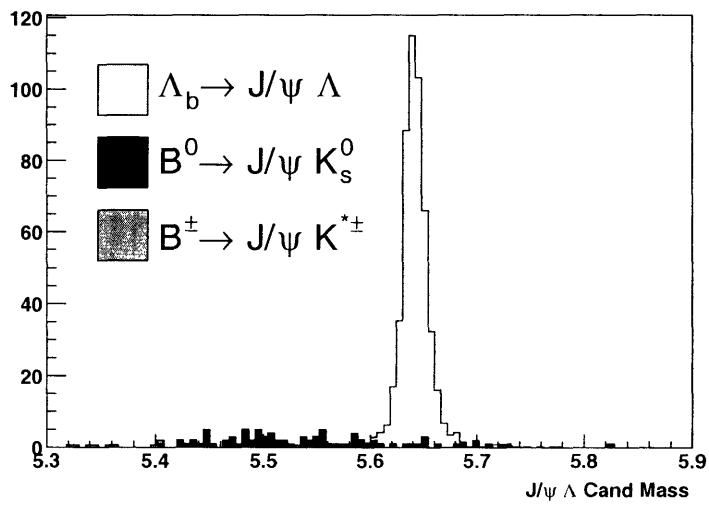

Figure 4-26: A plot of the b-hadron contributions to the reconstructed $\Lambda_b \rightarrow \mathrm{J}/\psi\Lambda$ signal.

contains 78% of the swapped events. This narrow Gaussian is offset by +1.1 MeV with respect to the correctly reconstructed peak. The remaining contribution is modeled by a second Gaussian with a width of 58.7 MeV and −7.8 MeV offset. The parameters of these two Gaussians are fixed in the fit.

There are almost no background contributions from other b-hadrons reconstructed as $B_s^0 \to J/\psi\phi$ as shown in Figure 4-23. This leaves only combinatoric background for this mode.

For the $B^0 \to J/\psi K_s^0$ mode we find a small remaining reflection from $\Lambda_b \to J/\psi\Lambda$ on the high mass side, as expected . On the low mass side we find a contribution from partial reconstruction of the $B^\pm \to J/\psi K^{*\pm}$ mode, where the $K^{*\pm}$ decays into K_s^0 and charged pions as shown in Figure 4-25. The $\Lambda_b \to J/\psi\Lambda$ mode is mainly background free, it has only small contributions from modes containing a K_s^0. This is illustrated in Figure 4-26.

4.5 Fit Results

The $\psi \to J/\psi\pi\pi$ decay mode shown in Figure 4-27, serves as a test case for our mass fit. The actual fit parameters are listed in Table 4.5. The mass value is 0.29 MeV/c^2 below the PDG average of 3685.96 ± 0.09 MeV/c^2.

Table 4.5: The results of the unbinned likelihood fit of the $\psi' \to J/\psi\pi\pi$ sample.

Parameter	Fit Output
Gaussian Mean $m_{\rm fit}$	3685.66 ± 0.08 MeV/c^2
Gaussian Sigma σ	3.45 ± 0.07 MeV/c^2
Background Fraction $f_{\rm b}$	0.8680 ± 0.0026
Background Slope $a_{\rm bg2}$	2284.5 ± 26.0 (GeV/c^2)$^{-2}$
Quadratic Background $b_{\rm bg}$	-304.5 ± 3.5 (GeV/c^2)$^{-3}$
Fit Probability	30.9%

The $B^+ \to J/\psi K^+$ mass distribution is shown back in Figure 4-29, and the results are in Table 4.6. The fitted B^+ mass is consistent with the PDG value of 5279.0 ± 0.5.

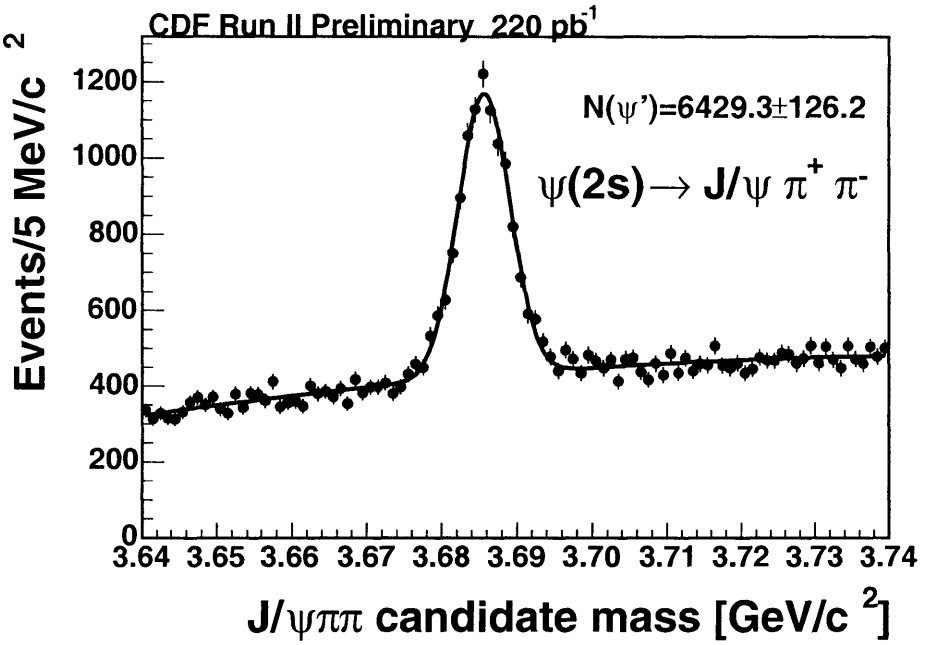

Figure 4-27: The mass distribution for the $\psi' \to J/\psi\pi^+\pi^-$ sample . The result of the log likelihood fit is superimposed.

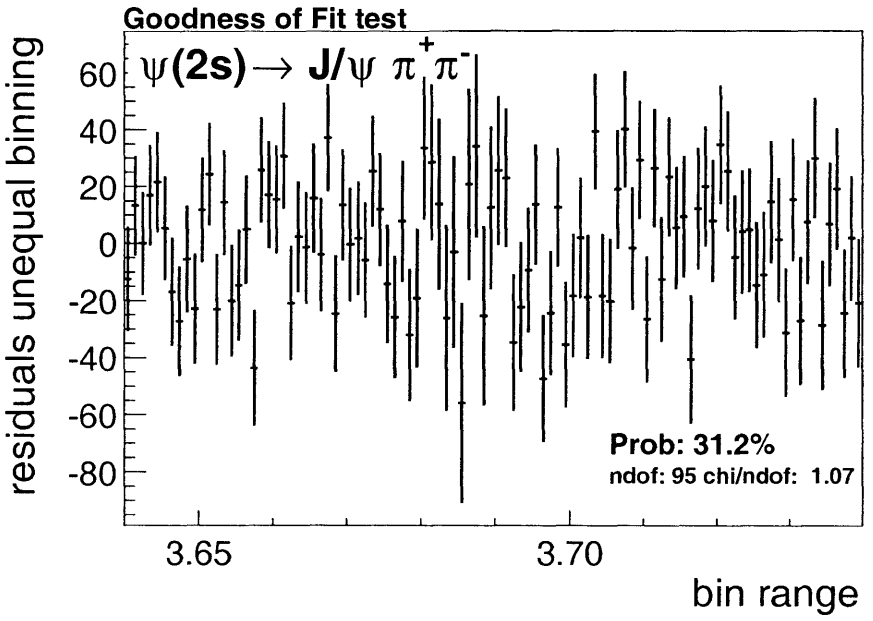

Figure 4-28: The result of a χ^2 goodness of fit test.

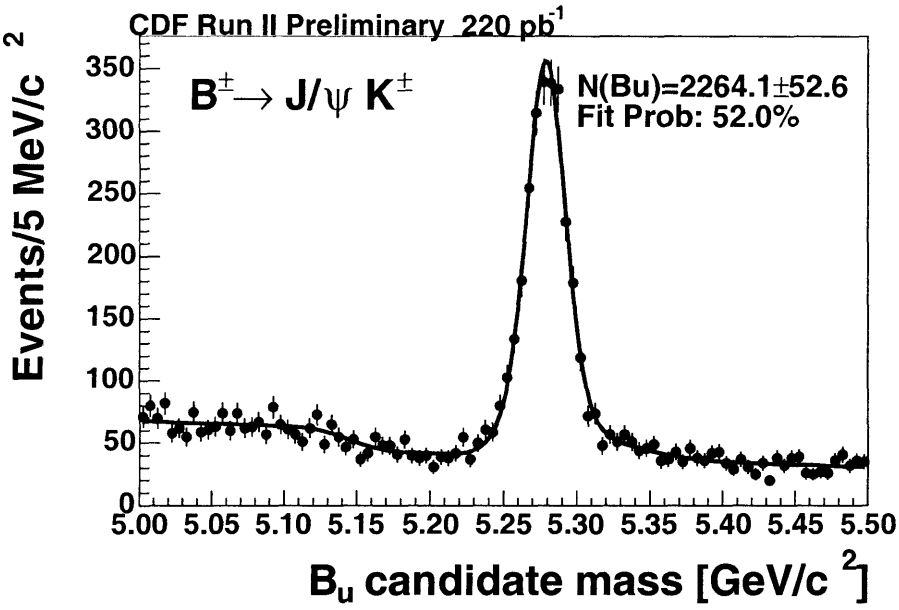

Figure 4-29: The B^+ mass distribution. The result of the log likelihood fit is superimposed.

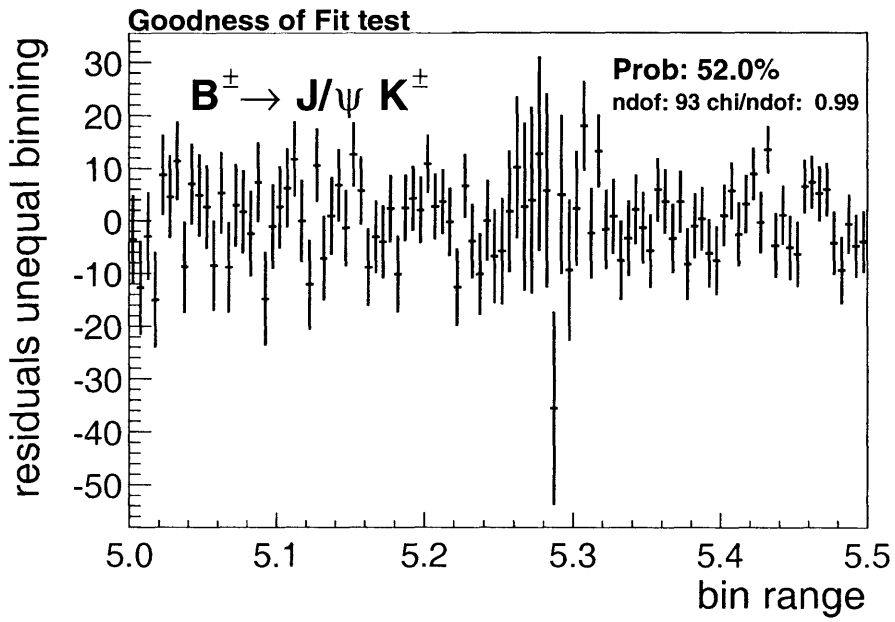

Figure 4-30: The result of a χ^2 goodness of fit test.

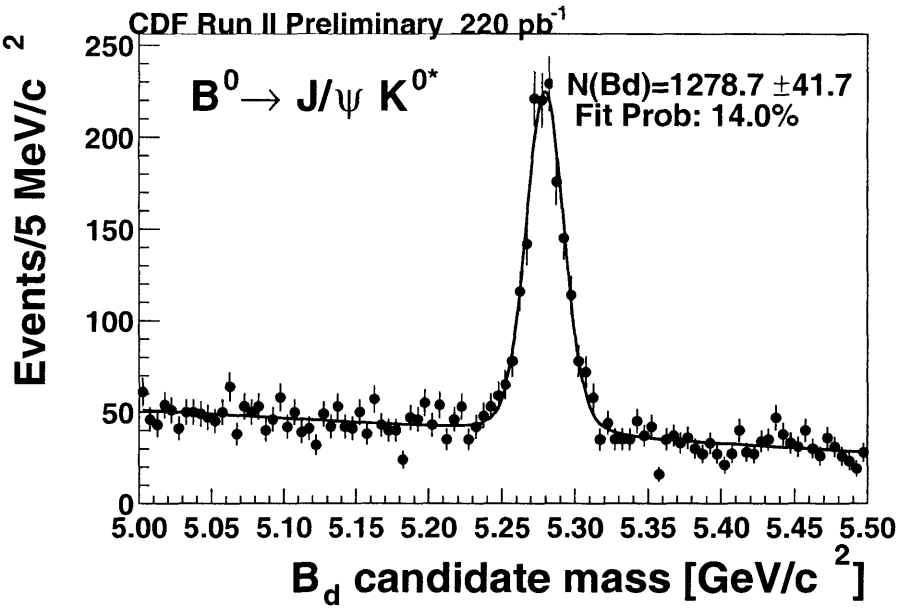

Figure 4-31: The B^0 mass distribution. The result of the log likelihood fit is superimposed.

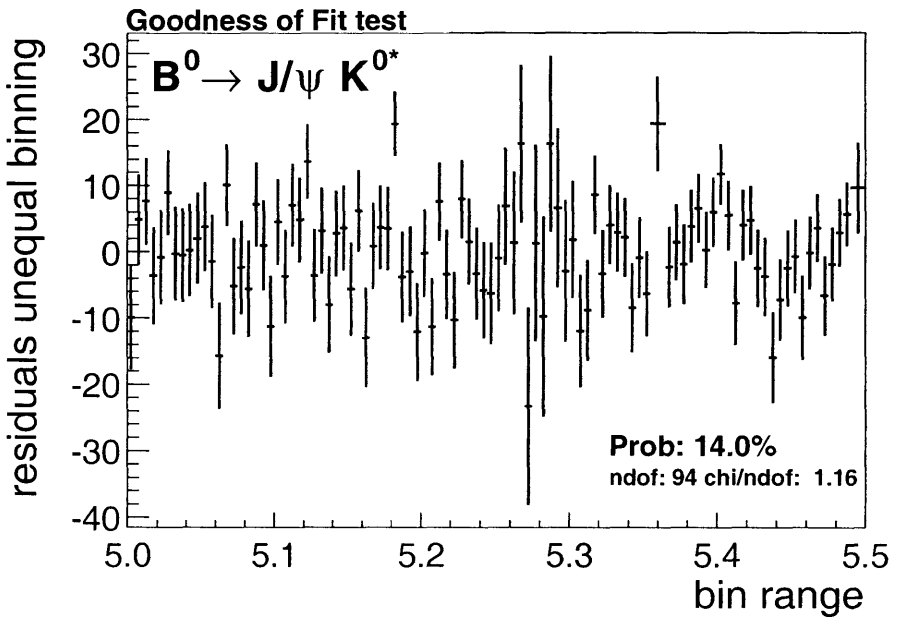

Figure 4-32: The result of a χ^2 goodness of fit test.

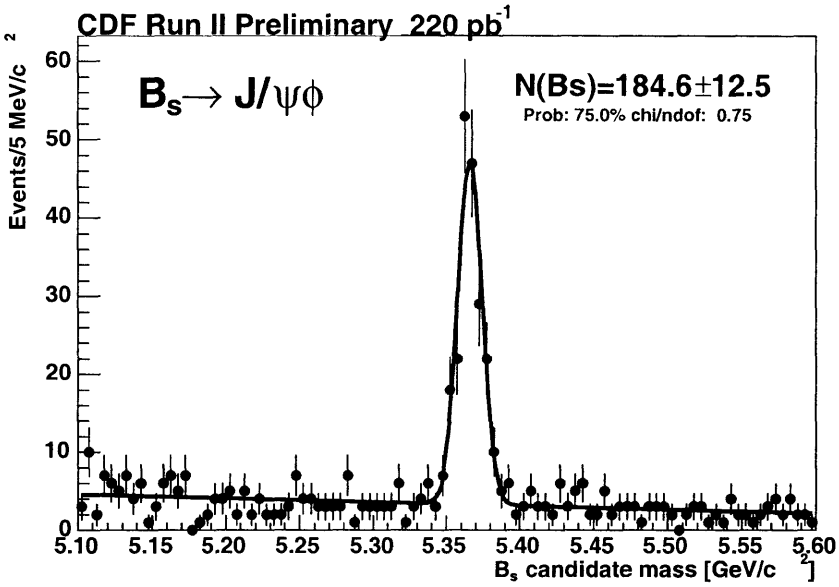

Figure 4-33: The B_s^0 mass distribution. The result of the log likelihood fit is superimposed.

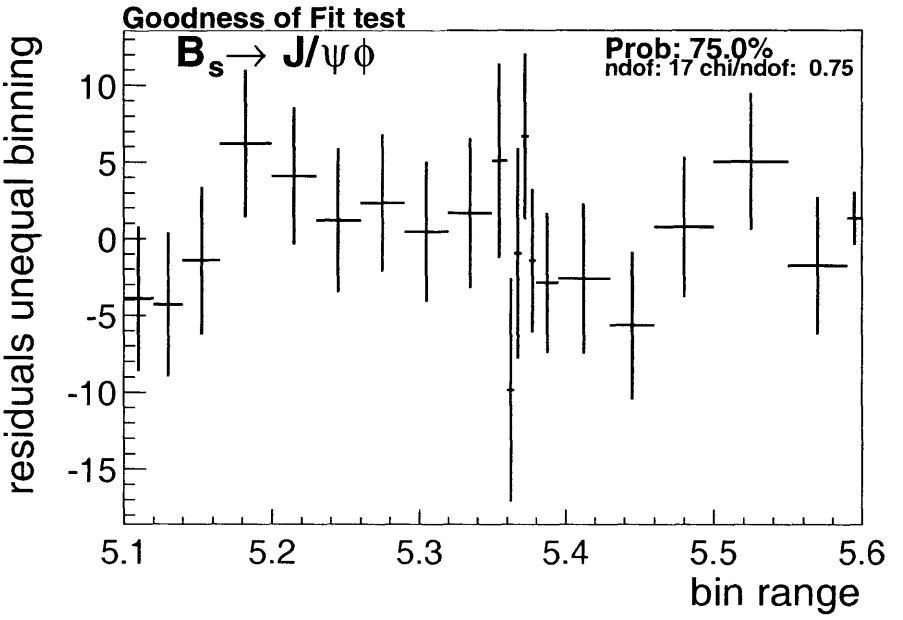

Figure 4-34: The result of a χ^2 goodness of fit test.

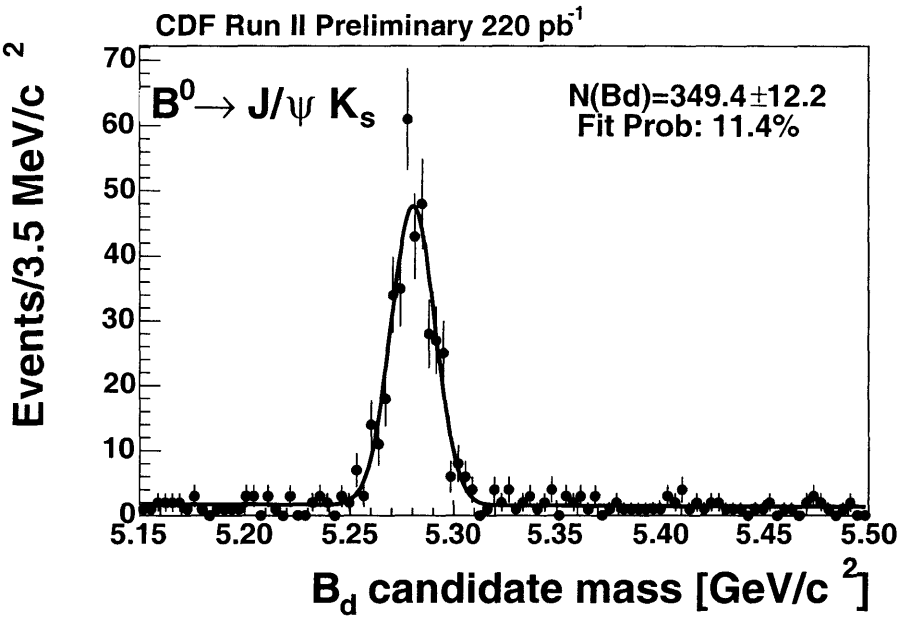

Figure 4-35: The B^0 mass distribution in the $B^0 \to J/\psi K_s^0$ decay mode. The result of the log likelihood fit is superimposed.

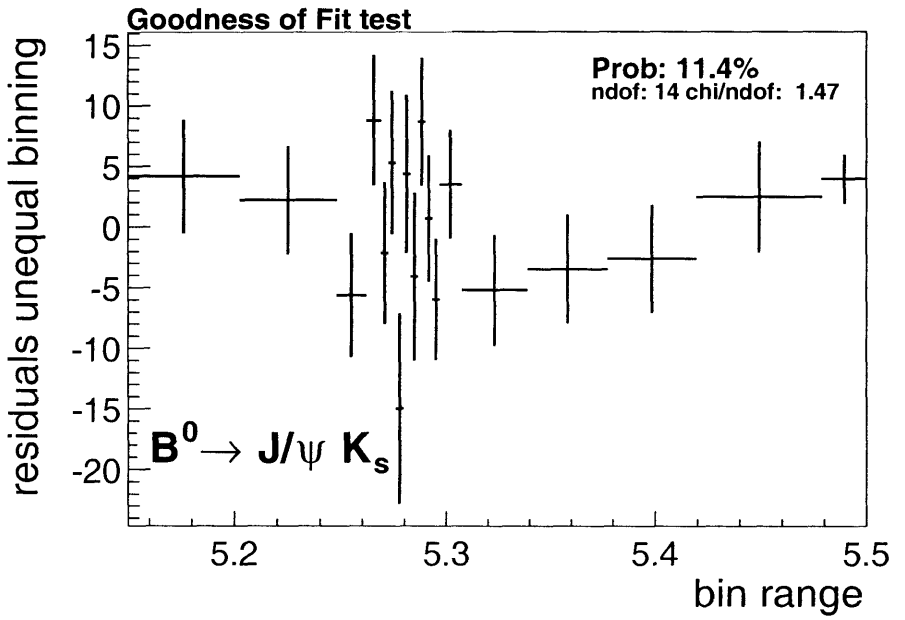

Figure 4-36: The result of a χ^2 goodness of fit test.

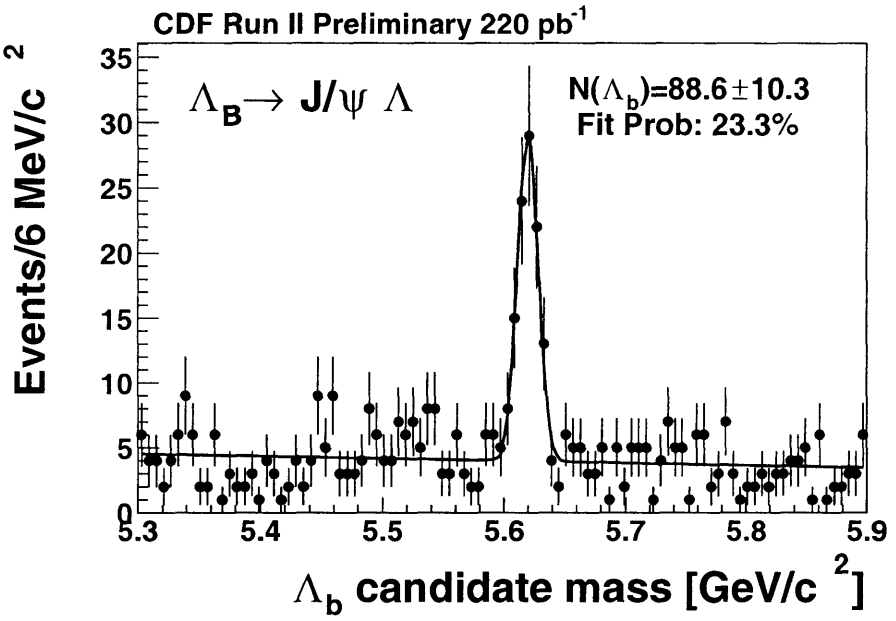

Figure 4-37: The Λ_b mass distribution. The result of the log likelihood fit is superimposed.

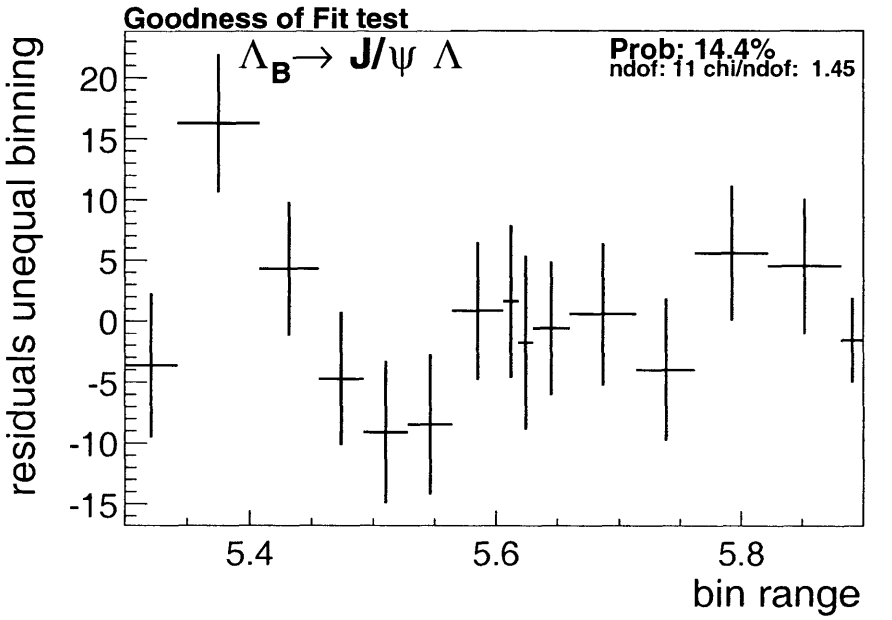

Figure 4-38: The result of a χ^2 goodness of fit test.

Table 4.6: The results of the unbinned likelihood fit of the B^+ sample.

Parameter	Fit Output
Gaussian Mean $m_{\rm fit}$	5279.10 ± 0.41 MeV/c^2
Gaussian Sigma σ	11.76 ± 0.99 MeV/c^2
Background Fraction $f_{\rm b}$	0.6727 ± 0.0076
Background Slope $a_{\rm bg1}$	-1.82 ± 0.37 (GeV/c^2)$^{-2}$
Second Gaussian Fraction $f_g 2$	0.452 ± 0.099
Turn-on Fraction f_T	0.114 ± 0.020
$J/\psi\pi$ Background f_π	0.0250 ± 0.0071
Fit Probability	52.0%

Table 4.7: The results of the unbinned likelihood fit of the B^0 sample.

Parameter	Fit Output
Gaussian Mean $m_{\rm fit}$	5279.63 ± 0.53 MeV/c^2
Gaussian Sigma σ	12.33 ± 0.54 MeV/c^2
Background Fraction $f_{\rm b}$	0.7562 ± 0.0080
Background Slope $a_{\rm bg1}$	-2.33 ± 0.22 (GeV/c^2)$^{-2}$
Fit Probability	14.0%

Table 4.8: The results of the unbinned likelihood fit of the B_s^0 sample.

Parameter	Fit Output
Gaussian Mean $m_{\rm fit}$	5366.02 ± 0.73 MeV/c^2
Gaussian Sigma σ	8.35 ± 0.63 MeV/c^2
Background Fraction $f_{\rm b}$	0.645 ± 0.024
Background Slope $a_{\rm bg1}$	-2.90 ± 0.73 (GeV/c^2)$^{-2}$
Fit Probability	75.0%

Table 4.9: The results of the unbinned likelihood fit of the $B^0 \to {\rm J}/\psi{\rm K}_{\rm s}^0$ sample.

Parameter	Fit Output
Gaussian Mean $m_{\rm fit}$	5280.46 ± 0.63 MeV/c^2
Gaussian Sigma σ	10.58 ± 0.54 MeV/c^2
Background Fraction $f_{\rm b}$	0.307 ± 0.024
Background Slope $a_{\rm bg1}$	-2.5 ± 2.5 (GeV/c^2)$^{-2}$
Fit Probability	11.4%

The $B^0 \to J/\psi K^{*0}$ sample is shown in Figure 4-31 with the unbinned fit superimposed. The fit results are listed in Table 4.7. Our fitted mass value is in good agreement with the PDG value (5279.4 ± 0.5 MeV/c^2).

Running the fitter on the events in the B_s^0 sample produces the results listed in Table 4.8. The B_s^0 sample is shown in Figure 4-33. The fitted B_s^0 mass is 3.6 MeV/c^2 below the PDG value (5369.6 ± 2.4 MeV) [12].

The $B^0 \to J/\psi K_s^0$ sample with the fit superimposed is shown in Figure 4-35. The fit results are listed in Table 4.9. Our fitted mass value is 1.06 MeV/c^2 above the PDG value (5279.4 ± 0.5 MeV/c^2) [12]. A 1.2σ discrepancy including systematic uncertainty, perfectly reasonable.

The $\Lambda_b \to J/\psi\Lambda$ sample is shown in Figure 4-37. The fit results are listed in Table 4.10. Our fitted mass value is in excellent agreement with the PDG value (5624 ± 9 MeV/c^2) and the CDF RUN I measurement ($5621 \pm 4_{\text{(stat)}} \pm 3_{\text{(sys)}}$ MeV/c^2).

Table 4.10: The results of the unbinned likelihood fit of the Λ_b sample.

Parameter	Fit Output
Gaussian Mean m_{fit}	5619.7 ± 1.2 MeV/c^2
Gaussian Sigma σ	8.5 ± 1.0 MeV/c^2
Background Fraction f_{b}	0.818 ± 0.021
Background Slope a_{bg1}	-0.73 ± 0.50 (GeV/c^2)$^{-2}$
Fit Probability	23.3%

4.6 Systematic Studies

4.6.1 Translation of momentum scale uncertainties

The uncertainties on the momentum scale calibration enter directly into the mass uncertainties. Naively, this can be done by repeated analysis with magnetic field and energy loss varied within the uncertainties. This exercise results in shifts of order ± 0.2 MeV/c^2 each. The size is confirmed with Monte Carlo simulation study. Adding the correlated uncertainties for magnetic field and energy loss in quadrature results

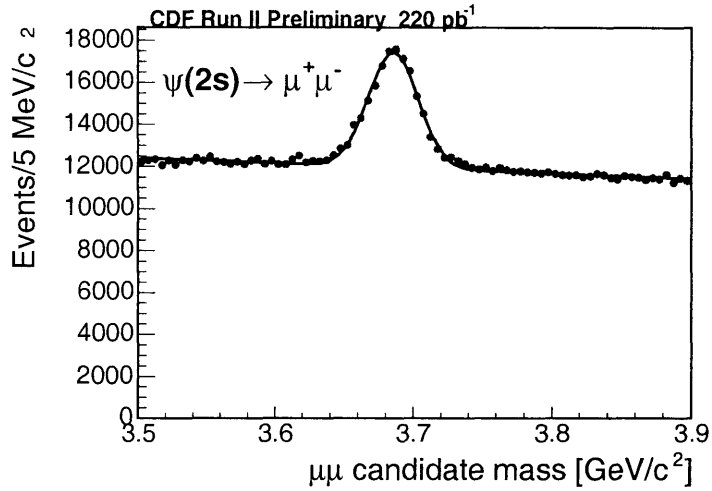

Figure 4-39: Di-muon mass distribution in the $\psi(2s)$ region.

in an overestimate of the uncertainties, but the negligible size permits this simplified approach.

In practice one has to also make sure, that the calibration at the J/ψ mass is safely transported to a different point on the momentum scale. We use particles with a well established mass as reference points to extrapolate the uncertainties. We use the Υ and $\psi(2s)$ for this purpose. The mass distribution for $\psi(2s)$ is shown in Figure 4-39. The use of the $D^0 \to K^{\pm}\pi^{\mp}$ decay is also investigated, but had to be rejected due to the dominate uncertainty for the world average D^0 mass.

In a decay that releases very little kinetic energy, like the $\Lambda \to p\pi$ decay, the measured mass is dominated by the masses of the decay particle and momentum deviations have little influence on the measurement. The figure of merit that determines the sensitivity to momentum scale uncertainties is the kinetic energy released by the decay, commonly known as Q-value. For the decay $J/\psi \to \mu^+\mu^-$ for example the Q-value is given by $Q = m(J/\psi) - 2m(\mu)$.

In Table 4.11 we compile the Q-values for the decays mentioned above. The relevant Q-values of b-hadrons are also listed. We plot the observed absolute mass difference versus the Q-value in Figure 4-40. Shown is a fit to the points. We find a slope of $(1.09 \pm 0.80) \times 10^{-4}$ and an offset of 0.25 ± 0.13 MeV.

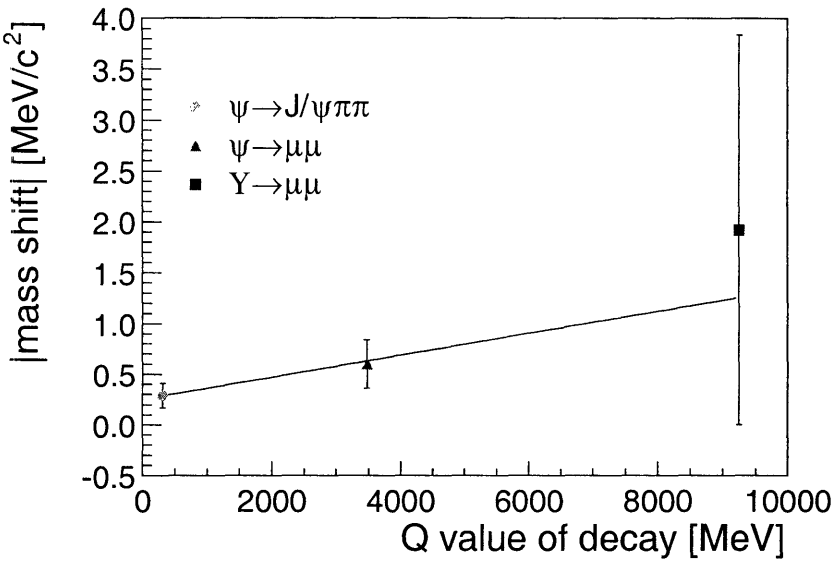

Figure 4-40: The uncertainty due to translation of the momentum scale. Shown are the full observed mass shifts with respect to the PDG value [12]. The uncertainties of the PDG value are included.

From this plot we infer systematic uncertainties due to the momentum scale. Using the Q-value from Table 4.11, and taking half the shift as systematic we find ± 0.22 MeV for $B^{\pm} \to J/\psi K^{\pm}$ and 0.20 MeV for the other b-hadron decay modes. This is consistent with the naive evaluation above.

The variation of the J/ψ mass in z is quite large as shown in Figure 4-11. Any deviation in the z-distribution of the b-hadrons with respect to the J/ψ-meson z-distribution results in a systematic shift. As the b-hadrons are reconstructed in decay modes involving a J/ψ such a difference in the z-distribution is expected to be very small. We quantify this effect by dividing the J/ψ sample and realistic Monte Carlo sample of $B^{\pm} \to J/\psi K^{\pm}$ into z-bins. The shift of the J/ψ mass in each bin with respect to the average is recorded as shown in Table 4.12. Finally the shift in each bin is weighted by the event fraction in that bin. The sum of all weighted shifts is equals the systematic shift. For the J/ψ that shift is zero by design. For the b-hadrons we find -0.016 MeV which can be neglected.

Table 4.11: A compilation of the Q-values of decays used to transport uncertainties from the momentum scale.

mode	Q-value	Δm
$\Upsilon \to \mu\mu$	9250 MeV	$+1.92 \pm 1.05$ MeV
$D^0 \to K\pi$	1231 MeV	± 0.5 MeV(PDG)
$\psi(2s) \to J/\psi\pi\pi$	311 MeV	-0.29 ± 0.12 MeV
$\psi(2s) \to \mu\mu$	3475 MeV	0.60 ± 0.24 MeV
$J/\psi \to \mu\mu$	2886 MeV	-
$B^{\pm} \to J/\psi K\pm$	1689 MeV	0.43 MeV
$B^0 \to J/\psi K^{*0}$	1291 MeV	0.39 MeV
$B_s \to J/\psi\phi$	1253 MeV	0.39 MeV
$\Lambda_b \to J/\psi\Lambda$	1412 MeV	0.40 MeV

Table 4.12: Influence of the z-variation of the J/ψ mass

Events B MC	Events J/ψ Data	J/ψ mass [MeV]	Shift wrt avg [MeV]	Shift weighted [MeV]	Shift B weighted [MeV]
1877	124780	3096.38	-0.0149	-0.00076	-0.00052
1845	126263	3096.73	0.3350	0.01745	0.01165
1881	123103	3096.56	0.1650	0.00838	0.00585
2335	127145	3096.07	-0.3249	-0.01704	-0.01430
3387	138650	3095.05	-1.3449	-0.07694	-0.08588
3094	142082	3095.82	-0.5749	-0.03370	-0.03353
2866	134136	3096.46	0.0650	0.00360	0.00351
2902	137770	3096.40	0.0050	0.00028	0.00027
3024	144601	3096.07	-0.3249	-0.01938	-0.01852
2612	126038	3096.58	0.1850	0.00962	0.00911
2729	123697	3096.59	0.1950	0.00995	0.01003
3284	141090	3096.76	0.3650	0.02125	0.02260
3131	132804	3096.66	0.2650	0.01452	0.01564
3966	133115	3095.54	-0.8549	-0.04695	-0.06392
3240	124857	3095.93	-0.4649	-0.02395	-0.02840
3263	133572	3096.77	0.3750	0.02067	0.02307
3066	129956	3097.16	0.7650	0.04102	0.04422
3101	122991	3097.46	1.0650	0.05405	0.06226
1437	56759	3097.16	0.7650	0.01791	0.02072
53040	2423409			0.00000	-0.01610

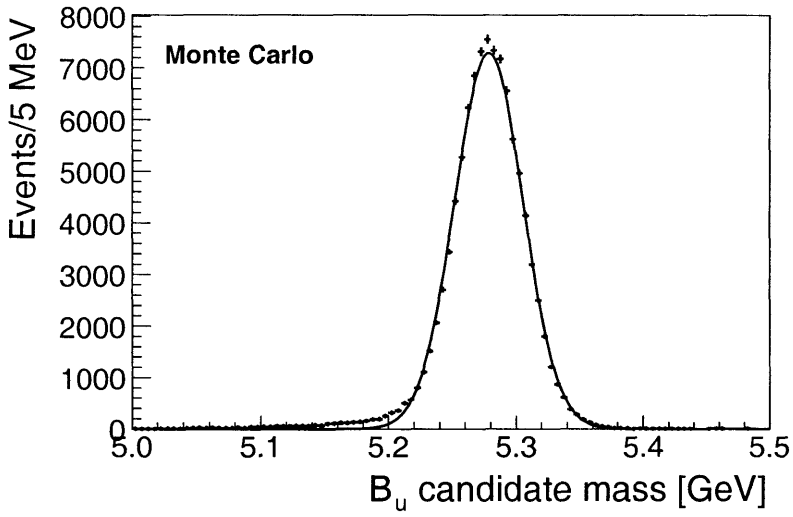

Figure 4-41: Monte Carlo simulation of $B^{\pm} \to \mathrm{J}/\psi \mathrm{K}^{\pm}$ reconstructed without a mass constraint on the J/ψ. The radiative decay of the J/ψ is present and causes a visible low mass tail.

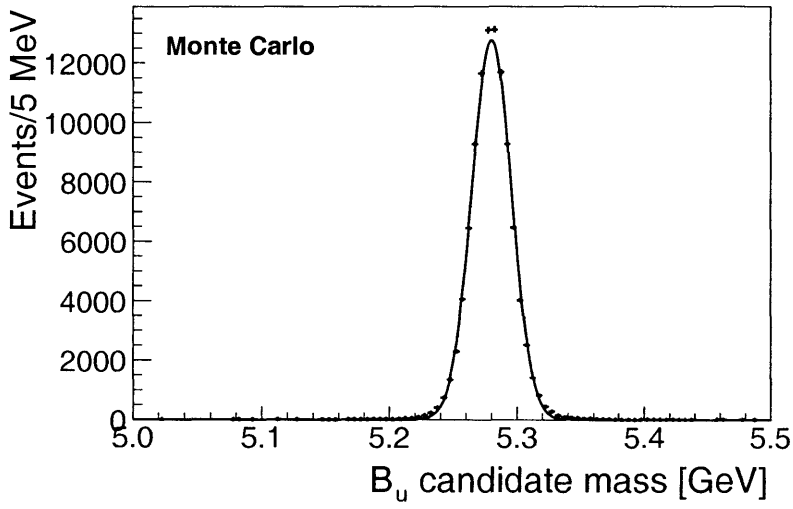

Figure 4-42: Monte Carlo simulation of $B^{\pm} \to \mathrm{J}/\psi \mathrm{K}^{\pm}$ reconstructed with mass constraint on the J/ψ. The radiative decay of the J/ψ is present, but no low mass tail remains.

4.6.2 Influence of radiative J/ψ decay

We have seen in Section 4.3.1 that the measured J/ψ mass is lowered due to its radiative decays. This effect is also present in $b \to J/\psi X \to \mu\mu X$ decays. A parametric Monte Carlo simulation is used to investigate the influence of this effect. We generate two samples of $B^{\pm}$ using Bgenerator [64, 65]. The B-meson is decayed with QQ, forcing the $B^{\pm}$ to decay into $J/\psi K^{\pm}$. In the first case we specify the default radiative decay of the J/ψ into two muons (QQ decay class 40), in the second case we use the decay method without the radiative treatment (QQ decay class 0). Both samples are reconstructed with and without a J/ψ mass constraint applied in the vertex fit. A shift of -1.46 MeV/c^2 in the B-meson mass is attributed to the radiative decay of the J/ψ. Figure 4-41 shows the low mass tail in the B-meson mass distribution. The effect is properly corrected by applying the mass constraint in the vertex fit. The corresponding mass distribution is shown in Figure 4-42. The results are summarized in Table 4.13.

Table 4.13: A comparison of the Monte Carlo simulations samples with and without radiative J/ψ decays. Also shown is the influence of the J/ψ mass constraint on this shift.

	J/ψ Mass Const.		No J/ψ Const.	
	Mass	Width	Mass	Width
B^+ no radiative	5279.99 ± 0.05	14.67 ± 0.04	5280.27 ± 0.10	25.96 ± 0.08
B^+ radiative	5280.14 ± 0.05	15.51 ± 0.04	5278.54 ± 0.09	26.82 ± 0.07
MC input mass	5280.00		5280.00	
Shift	$+0.14 \pm 0.05$		-1.46 ± 0.09	

4.6.3 Tracking Effects

We use two indicators to evaluate possible tracking effects. First, we look at the difference in measured mass when reverting to drift chamber only tracks. In case of no present bias both methods should return the same result. In fact there are known differences. When evaluating false curvature effects illustrated in Figure 4-43 different

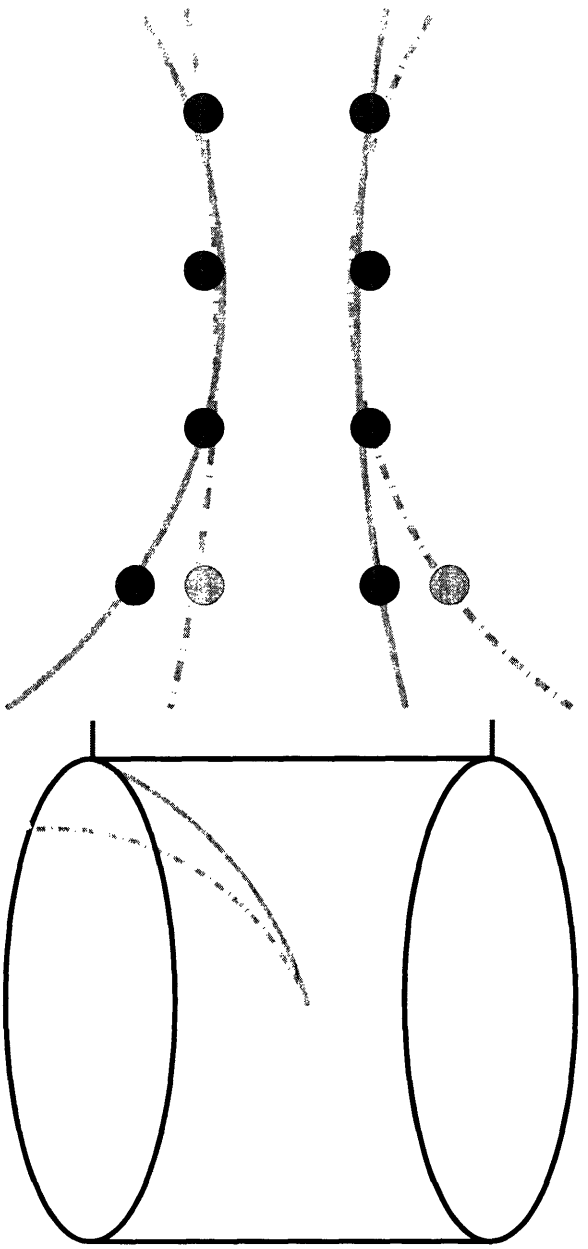

Figure 4-43: Illustration of false curvature effects that are tested in Figure 4-44. A horizontal misalignment results in a constant curvature offset. A torsion of the drift chamber end-caps results in a dependence of the measured curvature on the tilt of the track.

results are obtained for drift chamber only tracks and tracks with silicon hits as seen in Figure 4-44.

The second method is to release the J/ψ mass constraint. Here we have to take the result from Section 4.6.2 into account and correct for a 1.49 MeV/c^2 down shift. The resulting shifts are compiled in Table 4.14.

Another way to evaluate the mass differences is on an event by event basis. Figure 4-45 shows the event by event mass differences between silicon and drift chamber only tracks for the $B^{\pm}$ mode. The event by event mass difference between reconstruction with and without J/ψ mass constraint is shown in Figure 4-45. The observed mass shifts are smaller than the differences shown in Table 4.14. They agree however well with the shifts observed for the $B^0 \rightarrow J/\psi K^{*0}$ mode. We will show in Section 4.6.6 that the $J/\psi\pi$ background causes this additional shift.

For decay modes containing a V^0 we have to take into account effects from the highly displaced V^0 vertex. Tracks from the V^0 traverse only the parts of the detector located from the decay vertex outward. The additional material layer is placed at a radius of 34 cm as the correct radial location of the missing material is not known. The energy loss of displaced V^0 tracks is over-corrected when the V^0 decays between the physically correct location of the missing material and the radius of the phantom layer. The effect is estimated by releasing the mass constraint on the V^0 in the vertex fit. An up-shift of 1.49 MeV/c^2 in mass is observed for the $B^0 \rightarrow J/\psi K^0_s$ as shown in Table 4.14.

A fraction of the V^0 candidates decay outside the silicon detector, tracks originating from such decays are measured by the drift chamber only. The mass of the b-hadron is measured by a combination of tracks from the J/ψ-vertex with silicon hits and tracks from the V^0-vertex. Relative misalignments between drift chamber and silicon system move the vertices against each other, causing a possible bias. When reverting all tracks to drift chamber only measurements, a down shift of 1.94 MeV/c^2 is seen.

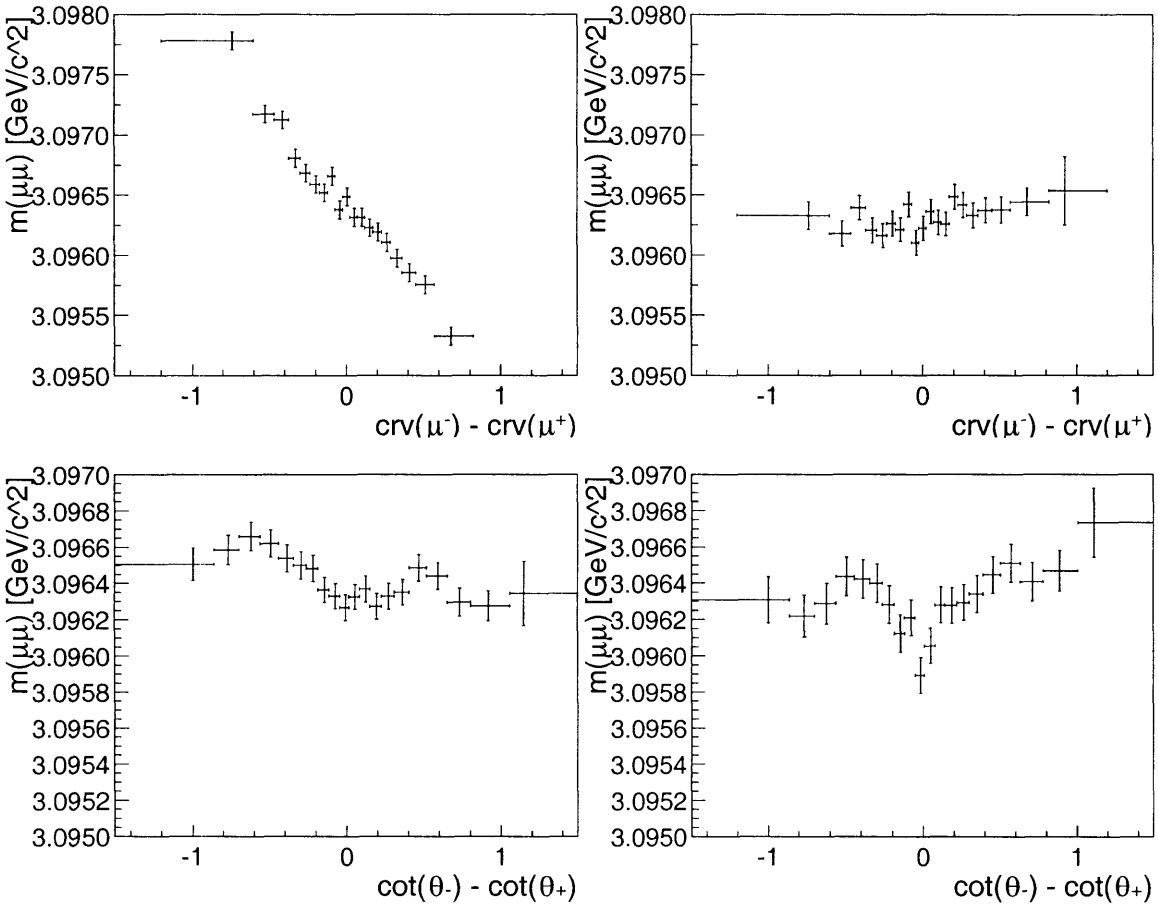

Figure 4-44: The di-muon mass variation as a function of the curvature difference (top), and the $\cot\theta$ difference (bottom), between the positive and negative muon in Run II. The left two plots are using default tracks while the right plots use COT only tracks.

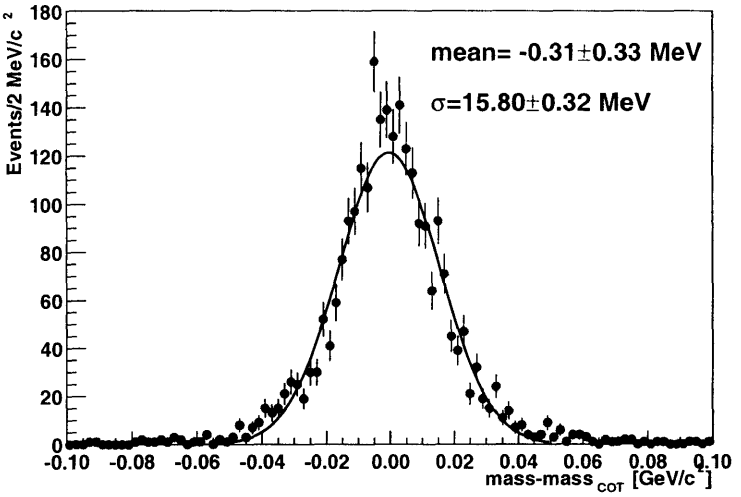

Figure 4-45: Event by event mass differences between $J/\psi K^{\pm}$ candidates reconstructed with silicon versus drift chamber only tracks.

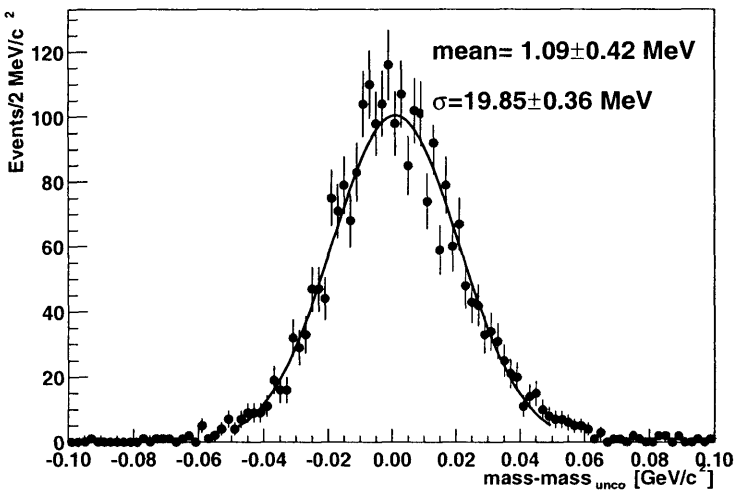

Figure 4-46: Event by event mass differences between $J/\psi K^{\pm}$ candidates reconstructed with versus without J/ψ mass constraint.

Table 4.14: An overview of mass shifts obtained by different tracking and reconstruction methods

Mode: $B^{\pm} \to J/\psi K^{\pm}$				
	uncorr. Mass	corr. Mass	Mass shift	Width
default	5279.10 ± 0.41	5279.10 ± 0.41	-	11.76 ± 0.99
COT only	5279.91 ± 0.60	5279.91 ± 0.60	$+0.81 \pm 0.44$	20.00 ± 1.51
default, no mass constr.	5279.52 ± 0.94	5280.98 ± 0.94	$+1.88 \pm 0.72$	33.07 ± 4.44
Mode: $B^0 \to J/\psi K^{*0}$				
	uncorr. Mass	corr. Mass	Mass shift	Width
default	5279.57 ± 0.53	5279.57 ± 0.53	-	13.76 ± 0.53
COT only	5279.92 ± 0.66	5279.92 ± 0.66	$+0.35 \pm 0.39$	16.39 ± 0.63
default, no mass constr.	5278.54 ± 1.13	5280.00 ± 1.13	$+0.43 \pm 1.00$	25.83 ± 1.16
Mode: $B^0 \to J/\psi K^0_s$				
	uncorr. Mass	corr. Mass	Mass shift	Width
default	5280.46 ± 0.63	5280.46 ± 0.63	-	10.58 ± 0.54
COT only	5278.52 ± 1.18	5278.52 ± 1.18	-1.94 ± 1.00	17.51 ± 1.15
default, no mass constr.	5281.95 ± 1.73	5281.95 ± 1.73	$+1.49 \pm 1.61$	26.74 ± 1.57

4.6.4 Track parameter covariance matrix scale

In Section 4.2.1 we mentioned, that we scale the track covariance matrices, because the returned uncertainties on the track parameters are underestimated. The result of the vertex fit relies on correct track uncertainties. An incorrect estimated covariance matrix could result in a mass bias.

We estimate the effect, by looking at the difference in reconstructed mass with scaled errors compared to the default. The shift on $B^{\pm}$ is -0.01 MeV/c^2, the shift on $B^0 \to J/\psi K^{*0}$ is $+0.06$ MeV/c^2. The effect is, therefore, negligible.

4.6.5 False curvature and charge asymmetry

Misalignments can lead to charge dependent tracking effects. An example is shown in top of Figure 4-43. A measurement point is offset by a fixed amount. Such offset will reduce positive and increase negative curvature and is commonly referred to as false curvature. The effect on the transverse momentum is largest for small curvature tracks. A plot of di-muon mass versus absolute curvature difference of the two muon

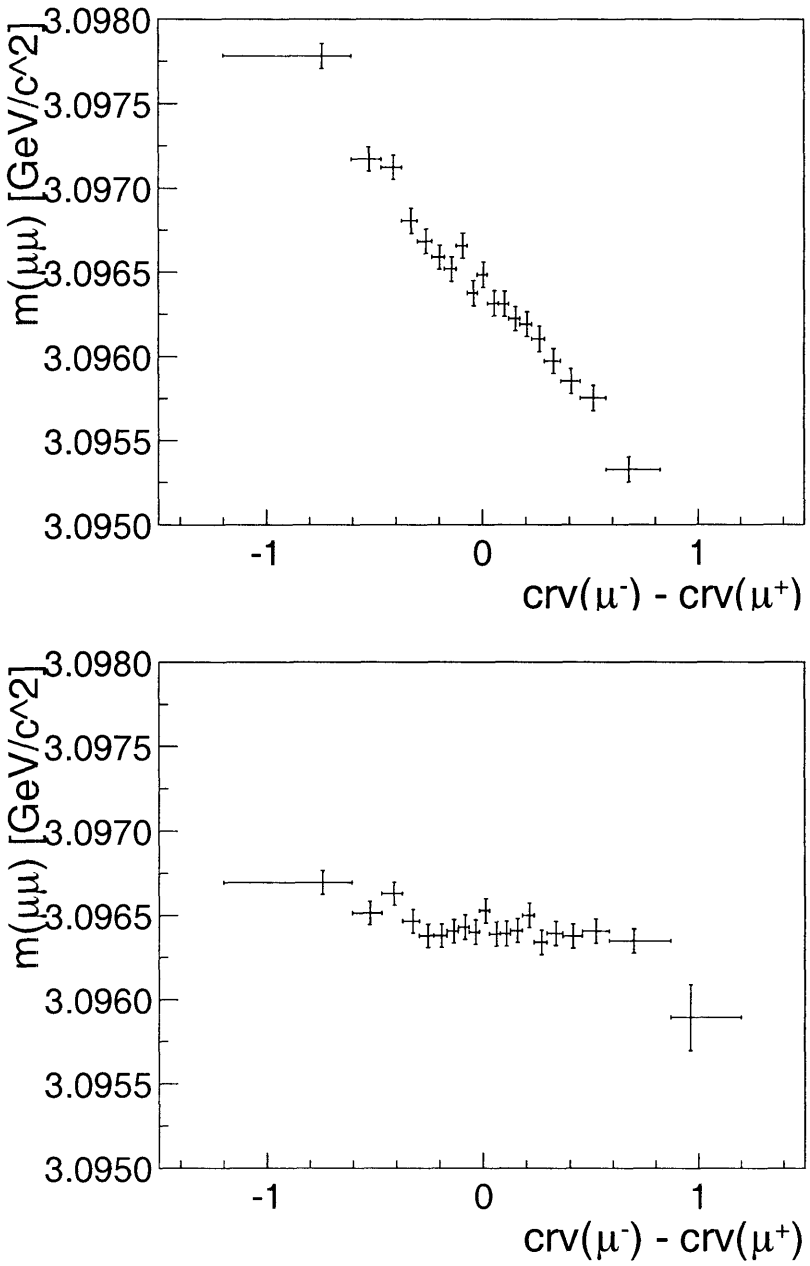

Figure 4-47: The di-muon mass variation as a function of the curvature difference between the positive and negative muon in Run II. The top plot shows the default and the bottom the behavior after a curvature correction is applied.

Table 4.15: Relative reconstruction efficiency for $B^0 \to \mathrm{J}/\psi\mathrm{K}^{*0}$ and $B^0 \to \mathrm{J}/\psi\rho$

mode	generated	reconstructed	ratio
$B^0 \to \mathrm{J}/\psi\mathrm{K}^{*0}$	5755722	423395	0.07356
$B^0 \to \mathrm{J}/\psi\rho$	17675349	11445	0.00065
			0.0088

tracks is a sensitive test for false curvature. This is shown in Figure 4-44. The left side of the plot corresponds to a small curvature negative track and a large curvature positive track.

The charged B-meson sample is evenly divided into 3454 B^+ and 3463 B^- candidates. The B^+ is reconstructed at 5277.30 ± 0.50 MeV/c^2 and the B^- at 5280.93 ± 0.58 MeV/c^2. As both modes are used, any charge asymmetry should cancel.

We correct the false curvature by adding an estimated offset of $-4.5 \times 10^{-07} - 2.1 \times 10^{-06} \sin(\phi_0)$. This correction largely reduces the effect for the J/ψ-mesons as shown in Figure 4-47. When applying this offset to the curvature, we reconstruct the B^+ at 5279.29 ± 0.53 MeV/c^2 and the B^- at 5278.84 ± 0.50 MeV/c^2. The mass splitting is significantly reduced after correction. Combining both modes yields 5279.06 ± 0.36 MeV/c^2.

Half of the resulting mass shift of -0.04 MeV/c^2 is taken as systematic.

4.6.6 Background model

An incomplete modeling of the background can result in mass biases. We encounter two modes with prominent background contributions in the peak region.

In case of the $B^0 \to J/\psi K^{*0}$ the mis-reconstructed, swapped component is shifted with respect to the mean. If we ignore this component, we observe a shift of $+0.12$ MeV that results in ± 0.06 MeV uncertainty.

The second case is the contribution of $B^\pm \to J/\psi\pi^\pm$ on the high mass side of the $B^\pm \to J/\psi K^\pm$ mode. If we ignore this component in our default fits, we observe a shift of $+0.26$ MeV resulting in a ± 0.13 MeV systematic uncertainty. However, this

feature also contributes to other observed systematics. When the mass resolution increases, this component can be swallowed by the main Gaussian and mimic large up-shifts of the mass. In fact, this is shown in Table 4.14 when the $B^{\pm}$ mass is reconstructed with drift chamber only tracks or without the mass constraint. We can mimic these shifts by simple Gaussian smearing of the mass from the nominal reconstruction. The Monte Carlo simulation yields a drift chamber only resolution of 13.6 MeV When the smearing by an additional 14 MeV which results in a final mass resolution of 20 MeV a mass shift is observed. Additional evidence supporting swallowed background hypothesis comes from the fact that these large shifts are not observed on an event by event basis as explained in Section 4.6.3. In $B^0 \to J/\psi K^{*0}$ exists an analog Cabibbo suppressed decay, $B^0 \to J/\psi\rho$. The relative fraction of $B^0 \to J/\psi\rho$ with respect to $B^0 \to J/\psi K^{*0}$ is of order 5%, the same as the relative fraction of $B^{\pm} \to J/\psi\pi^{\pm}$ with respect to the $B^{\pm} \to J/\psi K^{\pm}$ mode. The main difference is that we can distinguish between ρ and K^{*0} by the candidate mass. In Table 4.15 the relative reconstruction efficiency is estimated from Monte Carlo Simulation to less than 1%. This contribution can, therefore, be neglected.

4.6.7 L_{xy}-dependence

When plotting the J/ψ-mass versus L_{xy} a strong dependence is observed as shown in Figure 4-48. This dependence is observed for COT only tracks (Figure 4-49) as well as for tracks with silicon hits attached (Figure 4-48). That the effect is reproduced in the Monte Carlo simulation leads to the conclusion that we are dealing with a property of track reconstruction. The agreement is better for COT only tracks as seen in Figure 4-51.

A good candidate is the naturally arising correlation between impact parameter, d0, and curvature [88]. The effect is illustrated in Figure 4-52. Decays of J/ψ-mesons with muon tracks curving toward each other are referred to as cowboys and those with muon tracks curving away from each other as sailors. For cowboys a fluctuation or mis-measurement towards larger L_{xy} results in a larger curvature for both tracks. For sailors a fluctuation or mis-measurement towards larger L_{xy} results in a smaller

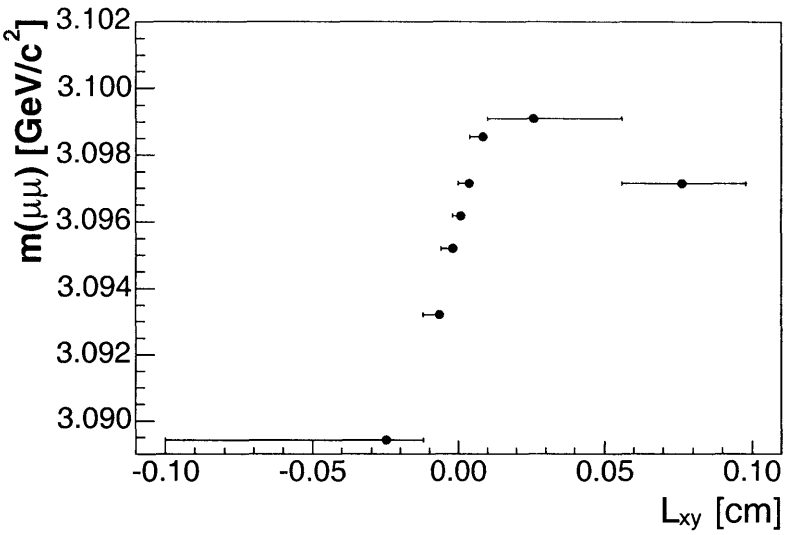

Figure 4-48: Dependence of the J/ψ-mass on L_{xy} for defTracks with silicon hits.

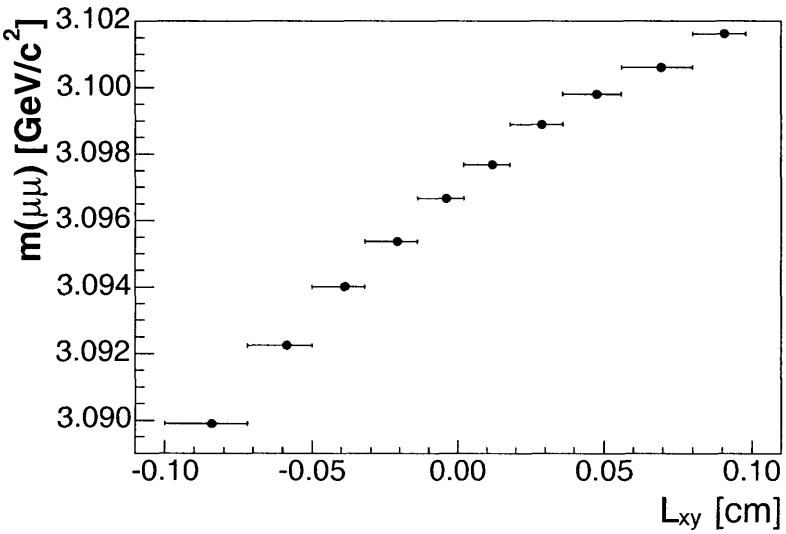

Figure 4-49: Dependence of the J/ψ-mass on L_{xy} for COT only tracks.

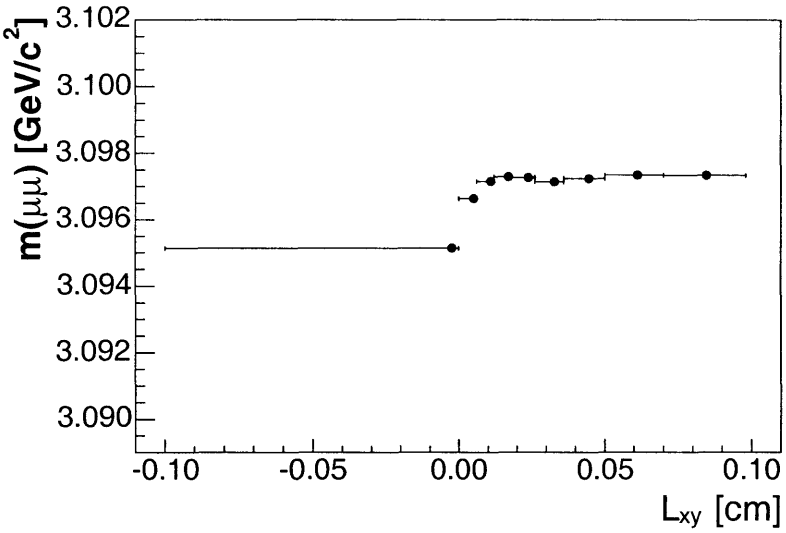

Figure 4-50: Dependence of the J/ψ-mass on L_{xy} for defTracks with silicon hits in realistic Monte Carlo.

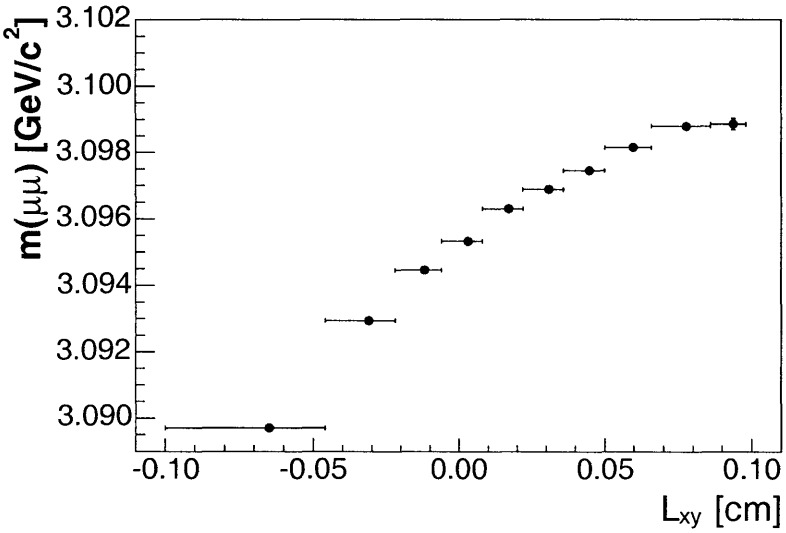

Figure 4-51: Dependence of the J/ψ-mass on L_{xy} for COT only tracks in realistic Monte Carlo.

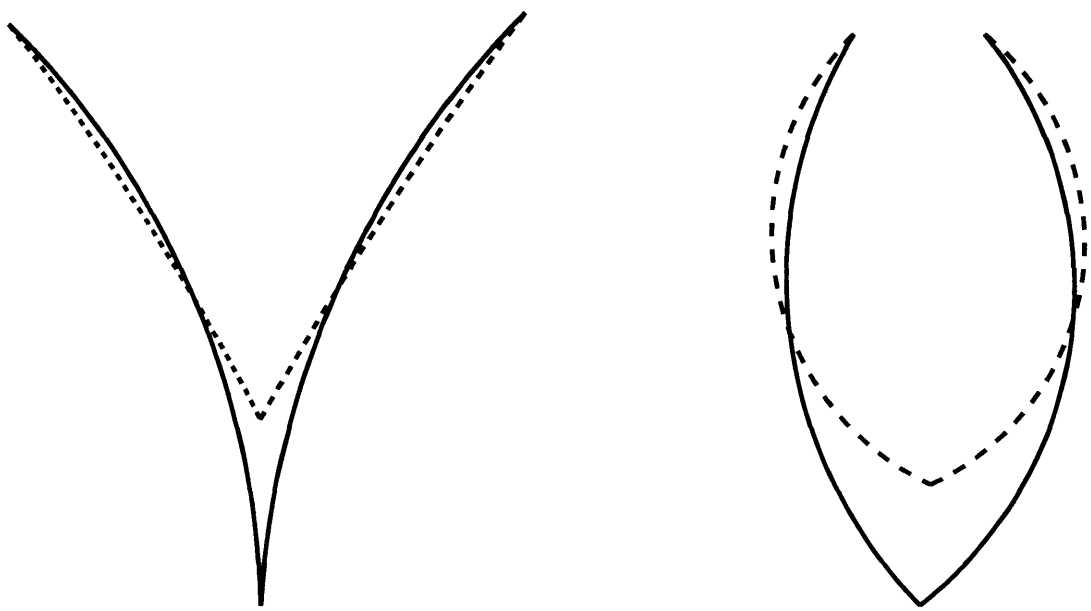

Figure 4-52: Illustration to show the origin of the impact parameter curvature correlation.

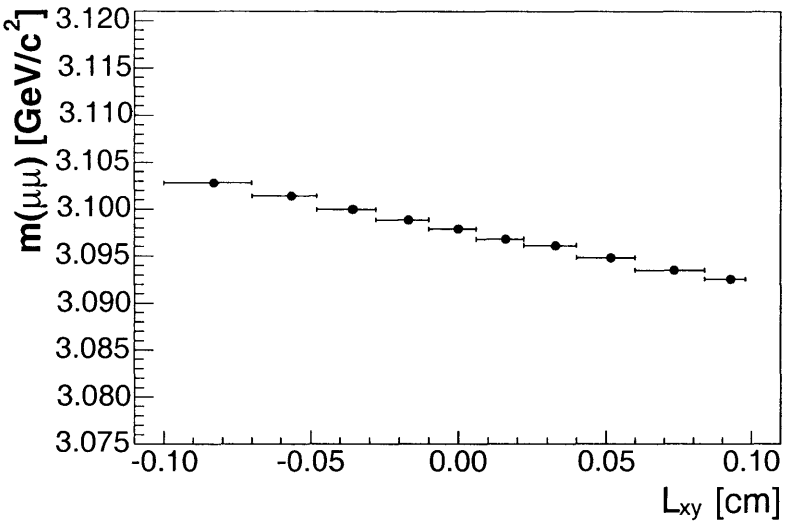

Figure 4-53: Dependence of the J/ψ-mass on L_{xy} for cowboy type J/ψ's.

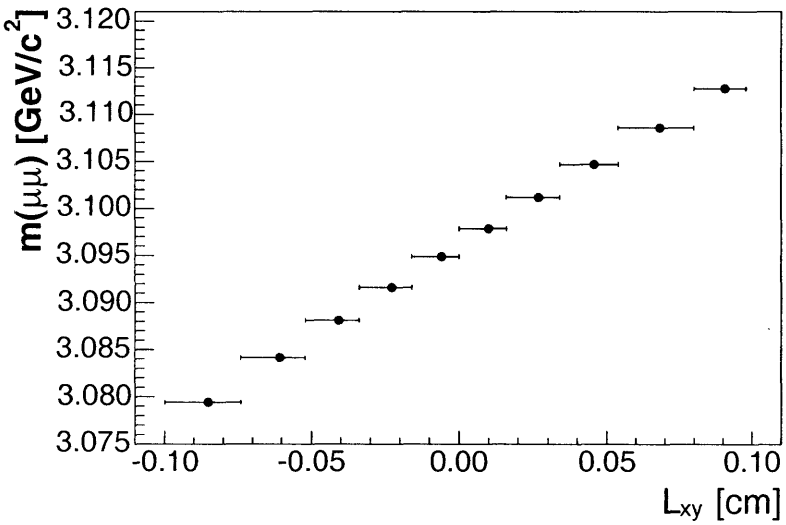

Figure 4-54: Dependence of the J/ψ-mass on L_{xy} for sailor type J/ψ's.

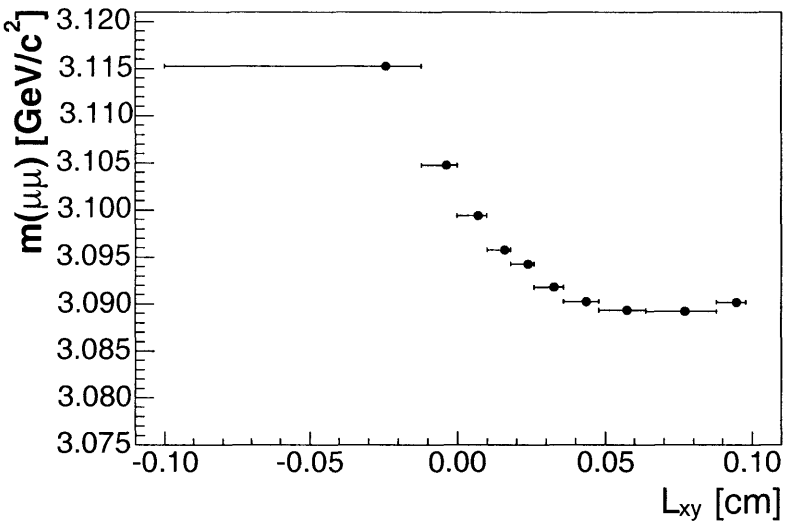

Figure 4-55: A simple toy Monte Carlo simulation assuming 80% correlation between impact parameter and curvature. Shown is the dependence of the J/ψ-mass on L_{xy} for cowboy type J/ψ's.

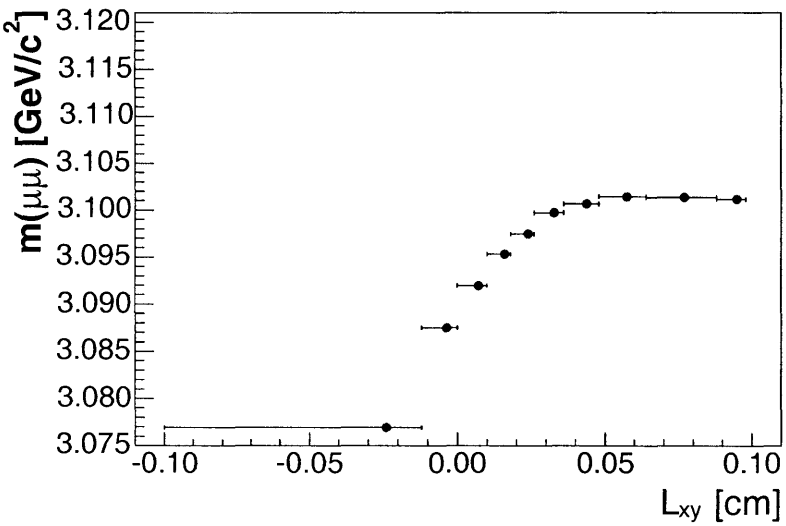

Figure 4-56: A simple toy Monte Carlo simulation assuming 80% correlation between impact parameter and curvature. Shown is the dependence of the J/ψ-mass on L_{xy} for sailor type J/ψ's.

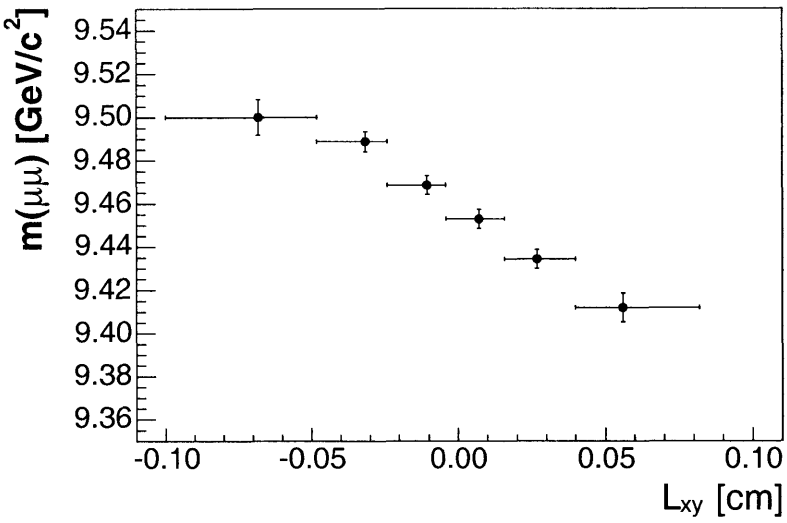

Figure 4-57: Dependence of the Υ-mass on L_{xy} for cowboy type Υ's.

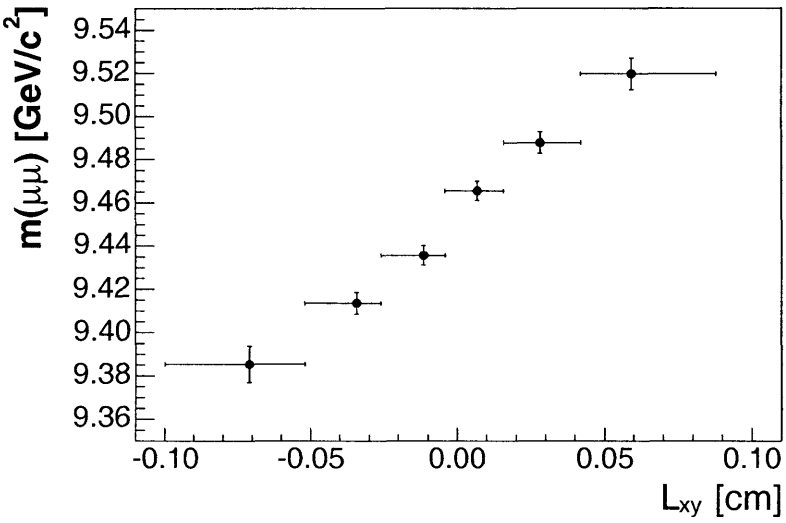

Figure 4-58: Dependence of the Υ-mass on L_{xy} for sailor type Υ's.

curvature for both tracks.

A prediction of this model is that cowboys and sailors show a slope of opposite sign in the mass versus L_{xy}. This prediction is confirmed in Figure 4-53. The sample consists of roughly equal numbers of cowboys and sailors, but the slope for sailors is steeper than the slope for cowboys, resulting in a net effect. See Figure 4-54.

It should be noted that this correlation depends not on the absolute value of L_{xy}, but rather on the shift with respect to the true value. This can be illustrated using $\Upsilon \to \mu\mu$ decays. All Υ mesons are produced promptly, e.g. they should exhibit an L_{xy} of zero. In reality we observe displaced Υ mesons due to resolution. The Υ shows the same L_{xy} dependence as the J/ψ as seen in Figure 4-58.

A simple toy Monte Carlo simulation that assumes a 80% correlation [88] reproduces the effect, in part. Figure 4-56 shows that the slopes for cowboys and sailors are identical. This suggests that another mechanism is present. When studying Figure 4-52, we note that also a correlation between L_{xy} and the opening angle of the two muons exists. This correlation is of the same sign for cowboys and sailors. For larger L_{xy} shifts the opening angle and, therefore, the mass increases. Adding this effect, explains the different slopes for cowboys and sailors and the observed net effect. Unfortunately this opening angle effect is non trivial to model.

We conclude that the effect depends only on the L_{xy} shift with respect to the real value and not on absolute L_{xy}. The asymmetric distribution of true L_{xy} could yield a possible mass bias. This resolution effect is reasonably described in the realistic Monte Carlo simulation, as discussed earlier. When reconstructing a large simulated $B^{\pm}$ sample, we find an offset of $+0.26 \pm 0.06$ MeV. We use half of this shift as systematic.

4.7 Systematics Summary

In Section 4.6.6 we have argued, that the systematic shifts of in the $B^{\pm}$ mode are due to $J/\psi\pi$ contamination. We use the $B^0 \to J/\psi K^{*0}$ mode for the evaluation of tracking and fitting systematics. The situation is summarized in Table 4.16. For the

$J/\psi V^0$ decay modes $B^0 \to J/\psi K_s^0$ and $\Lambda_b \to J/\psi\Lambda$ the higher statistics $B^0 \to J/\psi K_s^0$ deviations are used as shown in Table 4.17.

Table 4.16: Compilation of systematic uncertainty for the B mass measurements. All values are in MeV/c^2. The unbiased high statistics B^0 values have been used for the final $B^\pm$ and B_s systematics.

Source	$B^0 \to J/\psi K^{*0}$	$B^\pm \to J/\psi K^\pm$	$B_s^0 \to J/\psi\phi$
Tracking & Corrections			
momentum scale	0.20	0.22	0.20
Tracking	0.18	from B^0	from B^0
False Curvature	0.02	from $B^\pm$	from $B^\pm$
Fitting	0.10	from B^0	from B^0
Resolution bias	0.13	0.13	0.13
Fit Systematics			
K^{*0}'s with K-π Swapped	0.06	—	—
$J/\psi\pi$ contamination	—	0.13	—
Total Systematic Uncertainty	0.33	0.36	0.33

Table 4.17: Compilation of systematic uncertainty for the Λ_b mass measurement. All values are in MeV/c^2. The high statistics B^0 values have been used for the final Λ_b systematics.

Source	$B^0 \to J/\psi K_s^0$	$\Lambda_b \to J/\psi\Lambda$
Tracking & Corrections		
momentum scale	0.2	0.2
Tracking	1.0	from $B^0 \to J/\psi K_s^0$
Fitting	0.7	from $B^0 \to J/\psi K_s^0$
Total Systematic Uncertainty	1.2	1.2

4.8 Mass Differences

Many of the systematic uncertainties for the mass measurements are correlated and cancel in the mass difference. In addition, mass differences can be predicted by the theory far more precisely than absolute masses.

Table 4.18: Mass Differences

mass difference	input mass [MeV]	input mass [MeV]	Δm [MeV]
$m(B^{\pm}) - m(B^0)$	5279.10 ± 0.41	5279.63 ± 0.53	-0.53 ± 0.67
$m(B_s^0) - m(B^0)$	5366.01 ± 0.73	5279.63 ± 0.53	$+86.38 \pm 0.90$
$m(B_s^0) - m(B^{\pm})$	5366.01 ± 0.73	5279.10 ± 0.41	$+86.91 \pm 0.84$
$m(\Lambda_b) - m(B^0)$	5619.7 ± 1.2	5280.46 ± 0.63	$+349.2 \pm 1.4$

Table 4.19: Systematic Uncertainties of Mass Differences

mass difference	mom. scale uncert.	fit model uncert.	total syst. uncert.
$m(B^{\pm}) - m(B^0)$	0.00 MeV	0.14 MeV	0.14 MeV
$m(B_s^0) - m(B^0)$	0.01 MeV	0.06 MeV	0.06 MeV
$m(B_s^0) - m(B^{\pm})$	0.01 MeV	0.13 MeV	0.13 MeV
$m(\Lambda_b) - m(B^0)$	0.05 MeV	-	0.05 MeV

The evaluation of the mass differences from the results of the previous sections is straight forward. The momentum scale uncertainty simply scales. For the $B^{\pm} \to \mathrm{J}/\psi\mathrm{K}^{\pm}$ decay with a Q-value of 1689 MeV this uncertainty is ± 0.22 MeV. The momentum scale uncertainty for the mass difference Δm is then given by $0.22\ \mathrm{MeV}\frac{\Delta \mathrm{m}}{1689\ \mathrm{MeV}}$. We can eliminate correlated uncertainties by inspecting Table 4.16 and Table 4.17. Only systematic uncertainties related to the specific fit models remain. These uncertainties come from the $\mathrm{J}/\psi\pi$ contribution for the $B^{\pm} \to \mathrm{J}/\psi\mathrm{K}^{\pm}$ mode and the uncertainty due to the modeling of the $K\pi$ swap in $B^0 \to \mathrm{J}/\psi\mathrm{K}^{*0}$. For the $m(\Lambda_b) - m(B^0)$ difference the mass result from the $B^0 \to K_s^0\mathrm{J}/\psi$ mode has to be used, for the uncertainties to cancel. The results for the mass differences are shown in Table 4.18 and the systematic uncertainties are summarized in Table 4.19.

Chapter 5

Conclusion

We have performed improved mass measurements of B hadrons in Run II. Our result for the B_s^0 meson and the Λ_b baryon are the current world best measurements. The results for the $B^{\pm}$ and B^0 are competitive with the single best measurements. Our Λ_b mass is measured to be:

$$5619.7 \pm 1.2_{(stat)} \pm 1.2 \text{ MeV/c}^2$$

This value is in excellent agreement with the RUN I measurement. With the achieved precision the discrepancy mentioned in Section 1 can be resolved. This has great impact on the world average Λ_b mass. The leap in accuracy is clearly illustrated in Figure 5-1.

Our B_s^0 mass result is:

$$5366.01 \pm 0.73_{(stat)} \pm 0.33_{(sys)} \text{ MeV/c}^2$$

. A comparison with previous measurements is shown in Figure 5-2.

For the larger B^0 sample, we find:

$$5279.63 \pm 0.53_{(stat)} \pm 0.33_{(sys)} \text{ MeV/c}^2$$

Our value is in good agreement with the PDG.

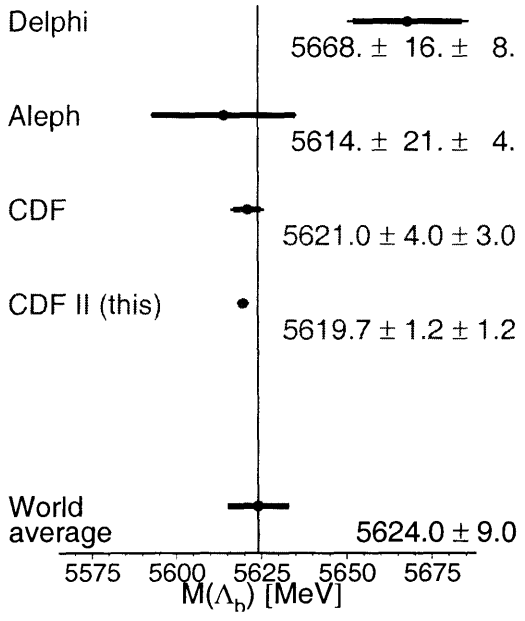

Figure 5-1: Comparison of this measurement of the Λ_b mass with previous measurements and the current world average.

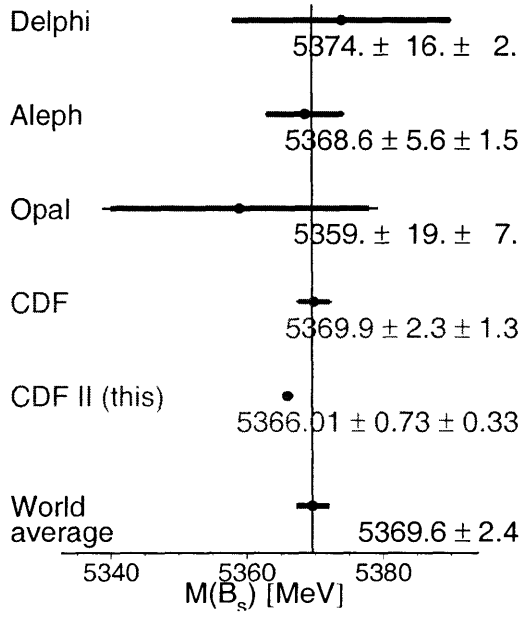

Figure 5-2: Comparison of this measurement of the B_s^0 mass with previous measurements and the current world average.

In the case of the B^+ where we have a fairly large sample of signal events, we measured the mass to be:

$$5279.10 \pm 0.41_{(stat)} \pm 0.36_{(sys)} \text{ MeV/c}^2$$

In this instance, with good statistics, we are very consistent with the PDG. The uncertainty is at the precision of single best measurement. A comparison with the current situation is shown in Figure 5-4. In additon we obtained the following results for the mass differences:

$$\begin{aligned}
m(B^{\pm}) - m(B^0) &= -0.53 \pm 0.67_{(stat)} \pm 0.14_{(sys)} \text{ MeV/c}^2 \\
m(B_s^0) - m(B^0) &= +86.38 \pm 0.90_{(stat)} \pm 0.06_{(sys)} \text{ MeV/c}^2 \\
m(\Lambda_b) - m(B^0) &= +349.2 \pm 1.4_{(stat)} \pm 0.05_{(sys)} \text{ MeV/c}^2
\end{aligned}$$

With these updated results CDF has become a primary contributor to the precision measurement of b-hadron masses.

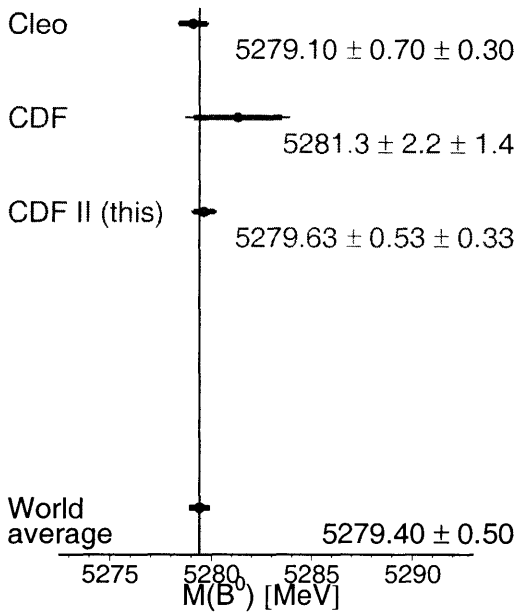

Figure 5-3: Comparison of this measurement of the B^0 mass with previous measurements and the current world average.

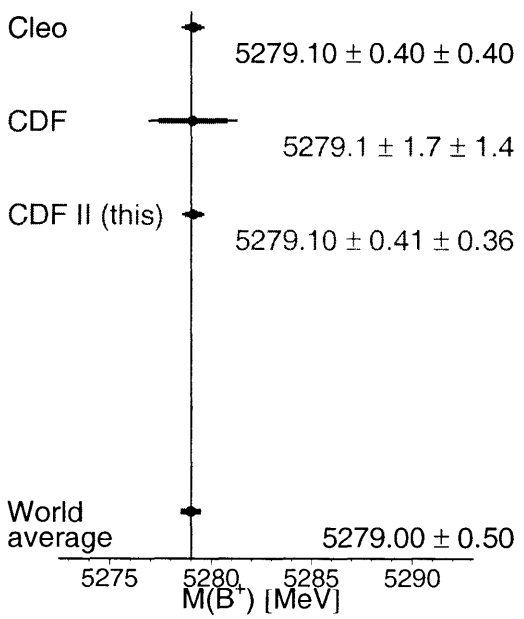

Figure 5-4: Comparison of this measurement of the $B^{\pm}$ mass with previous measurements and the current world average.

Bibliography

[1] J. Joyce. *Finnegans Wake.* Viking Press, New York, 1939. p.383.

[2] T.Nakano et al. *Phys.Rev.Lett.*, 91:012002, 2003.

[3] D. et al Acosta. "Measurement of the B+ total cross section and B+ differential cross section dsigma/dp(T) in p anti-p collisions at $\sqrt{s} = 1.8$ TeV". *Phys. Rev.*, D65:052005, 2002.

[4] R. et al Ammar. "Measurement of the total cross section for e+ e- –¿ hadrons at $\sqrt{s} = 10.52$ GeV". *Phys. Rev.*, D57:1350–1358, 1998.

[5] M. Acciarri et al. Heavy quarkonium production in z decays. *Phys. Lett.*, B453:94–106, 1999.

[6] F. et al Abe. "Measurement of the anti-proton proton total cross-section at $\sqrt{s} = 546$ GeV and 1800 GeV". *Phys. Rev.*, D50:5550–5561, 1994.

[7] P. Abreu et al. *Phys. Lett.*, B(374):351, 1996.

[8] D. Buskulic et al. *Phys. Lett.*, B(380):442, 1996.

[9] F. Abe *et al. Phys. Rev.*, D(55):1142, 1997.

[10] W. Wester. *A Measurement of the Mass of the B_s^0 Meson in Proton-Antiproton Collisions at $\sqrt{s} = 1.8$* TeV. PhD thesis, University of California, Berkeley, 1994.

[11] F. Abe *et al. Phys.Rev.*, D(53):3496, 1996.

[12] D.E. Groom et al (PDG). *Eur. Phys. Jour.*, C(15), 2000.

[13] S.Schramm W.Greiner and E.Stein. *Quantum Chromodynamics.* Springer, 2nd edition, 2002.

[14] M.Gell-Mann and Y. Ne'eman. *The eightfold way.* W.A.Benjamin, Inc., 1964.

[15] G. Zweig, 1964. CERN Reports 8182/TH 401 and 8419/TH 412.

[16] D.Gross and F.Wilczek. *Phys.Rev.Lett.*, (30):1343, 1973.

[17] M.Gell-Mann H.Fritzsch and H.Leutwyler. *Phys.Rev.*, B(47):365, 1973.

[18] S.Okubo. Note on Unitary Symmetry in Strong Interactions. *Prog.Theoret.Phys.*, Kyoto(27):949–966, 1962.

[19] S.Coleman and S.L.Glashow. Electrodynamic properties of baryons in the unitary symmetry scheme. *Phys.Rev.Lett.*, 6:423–425, 1961.

[20] R.N. Faustov D. Ebert and V.O. Galkin. Heavy Quark Potential and mass spectrum of Heavy Mesons. *Phys. Rev.*, D(57):5663–5669.

[21] R.N. Faustov D. Ebert and V.O. Galkin. Heavy Quark Potential and mass spectrum of Heavy Mesons. *Phys. Rev.*, D(59):019902.

[22] U. Aglietti. Prediction of beauty particle masses with the heavy quark effective theory. *Phys. Lett.*, B(281):341–344, 1992.

[23] A. Ali Khan et al. Scaling of the B and D meson spectrum in lattice QCD. *Phys. Rev.*, D(62):054505, 2000.

[24] A. Ali Khan et al. Heavy light mesons and baryons with b quarks. *Phys. Rev.*, D(62):074503, 2000.

[25] R. Lewis N. Mathur and R.M. Woloshyn. Charmed and bottom baryons from lattice nonrelativistic QCD. *Phys. Rev.*, D(66):014502, 2002.

[26] C. Davies et al. B_s mesons using staggered light quarks. *Nucl. Phys.*, B (Proc. Suppl.)(119):604–606, 2003. see: hep-lat/0209096.

[27] Ch.Berger. *Teilchenphysik.* Springer, 1992.

[28] C. Davies. The Heavy Hadron Spectrum. 1997. see: hep-ph/9710394.

[29] J.Richardson. *Phys. Lett.*, B(82):272, 1979.

[30] A.Martin. *Phys. Lett.*, B(93):338, 1980.

[31] C.Quigg and J.L.Rosner. *Phys. Lett.*, B(71):153, 1977.

[32] S. Gottlieb. Results on improved KS dynamical configurations: spectrum, decay constants, etc., 2003. hep-lat/0310041.

[33] H.J.Rothe. *Lattice Gauge Theories, An Introduction*, volume 59 of *Lecture Notes in Physics.* World Scientific, 2nd edition.

[34] C.T.H.Davies. Lattice QCD. In C.T.H.Davies and S.M.Playfer, editors, *Heavy Flavor Physics, Theory and Experimental Results in Heavy Quark Physics.* Proceedings of the 55th Scottish Universities Summer School in Physics, Institute of Physics, 2002.

[35] C. Aubin et al. High-Precision Lattice QCD Confronts Experiment, 2003. hep-lat/0304004.

[36] A.V. Manohar and M.B.Wise. *Heavy Quark Physics.* Cambridge University Press, 2000.

[37] W.E.Caswell and G.P.Lepage. *Phys.Lett.*, B(167):437, 1986.

[38] J. Cockroft and E. Walten. *Proc. Royal Society*, page 136:619, 1932.

[39] E. L. Hubbard. Booster synchrotron. FERMILAB-TM-0405.

[40] R. Billinge. Booster radius. FERMILAB-FN-0152.

[41] C. Hojvat et al. The multiturn charge exchange injection system for the FERMILAB Booster accelerator. FERMILAB-TM-0872.

[42] "Fermilab Beams Division, Run II Handbook".
See: http://www-bd.fnal.gov/runII/.

[43] "Fermilab's Chain of Accelerators".
See: http://www-bd.fnal.gov/public/chain.html.

[44] D. Mohl, G. Petrucci, L. Thorndahl, and S. Van Der Meer. "PHYSICS AND TECHNIQUE OF STOCHASTIC COOLING". *Phys. Rept.*, 58:73–119, 1980.

[45] R. Blair et. al. The CDF-II detector: Technical design report, 1996. FERMILAB-Pub-96/390-E.

[46] T. Affolder et. al. CDF Central Outer Tracker, 2003. FERMILAB-Pub-03/355-E.

[47] F. Bedeschi et al. *NIM*, A(268):50–74, 1988.

[48] T. K. Nelson. "The CDF Layer 00 detector". *Int. J. Mod. Phys.*, A16S1C:1091–1093, 2001. FERMILAB-CONF-01-357-E.

[49] T. K. Nelson. "The CDF-II silicon tracking system". *Nucl. Instrum. Meth.*, A485:1–5, 2002.

[50] G. Ascoli et al. *NIM*, A(268):33–40, 1988.

[51] V. Martin. private communications.

[52] S. Belforte et al. The CDF Run I Muon System Upgrade, 1995, revised 2002. CDF-note: CDF/DOC/MUON/PUBLIC/6362.

[53] C.M. Ginsburg. CDF Run 2 Muon System, 2004. FERMILAB-Conf-03/386-E.

[54] D. Acosta et al. *NIM*, A(518):605–608, 2004.

[55] S. Holm et al. "System architecture and hardware design of the CDF XFT". *IEEE Trans. Nucl. Sci.*, 47:895–902, 2000. FERMILAB-Conf-99-317.

[56] J. Strologas L. Holloway. Determination of the XTRP maps, 1997.
CDF-note: CDF/DOC/TRIGGER/PUBLIC/4146.

[57] H.S. Kim L. Holloway. Update on the Measurement of the Track Extrapolation Parameters for CMU and CMX, 2000.
CDF-note: CDF/TRIGGER/CDFR/XXXX, private communications.

[58] W. Ashmanskas et al. *NIM*, A(447):218, 2000.

[59] K. Anikeev et al. Level3 and Event Builder for ACES, 2001.
CDF-note: CDF/DOC/TRIGGER/CDFR/5793.

[60] C. Hays et al. The COT Pattern Recognition Algorithm and Offline Code, 2004.
CDF-note: CDF/DOC/TRACKING/CDFR/6992.

[61] S. Menzemer et. al. TrackingKal- A Tracking and Alignment Software Package for the CDFII Silicon Detector, 2002. CDF-note: CDF/DOC/TRACKING/PUBLIC/5968.

[62] W.M. Yao and K. Bloom. Outside In Silicon Tracking at CDF, 2000. CDF-note: CDF/TRACKING/DOC/CDFR/5591.

[63] J. Bellinger et al. A Guide to Muon reconstruction and Software for Run 2, 2002.
CDF-note: CDF/DOC/COMP_UPG/CDFR/5870.

[64] P. Sphicas. A $b\bar{b}$ Monte Carlo Generator , 1996. CDF-note: CDF/DOC/BOTTOM/CDFR/2655.

[65] P. Murat K. Anikeev and Ch. Paus. Description of Bgenerator II , 1999. CDF-note: CDF/DOC/BOTTOM/CDFR/5092.

[66] S.Dawson P.Nason and R.K.Ellis. *Nucl.Phys.*, B(327):49, 1989.

[67] K. Read P. Avery and G. Trahern, 1985. Cornell Internal Note CSN-22 (unpublished).

[68] R. Brun and F. Carminati. GEANT Detector Description and Simulation Tool. CERNProgram Library Long Write-up W5013; see also: http://consult.cern.ch/writeup/geant/.

[69] A.Cerri and M. Rescigno. The CDFII realistic Simulation Package. CDF-note: in preparation.

[70] H.S.Bridge and M.Annis. A Cloud-Chamber Study of the New Unstable Particles. *Phys.Rev.*, 82(3):445–446, 1951.

[71] V.L.Fitch. Elementary particle physics: The origins. *Rev.Mod.Phys.*, 71(2):0034–6861/S25–S32, 1999.

[72] A. Korn and M. Herndon.
See CdfCode browser: TrackingUserHL/TrackFitting/TrackRefitter.hh (version 4.11.2).

[73] A. Korn.
See CdfCode browser: Extrapolator/G3XExtrapolator (version 4.11.2).

[74] R. Madrak.
See CdfCode browser: TrackingObjects/Tracks/CorCotTrack.hh (version 4.11.2).

[75] J. Marriner. Secondary Vertex Fit With Mass and Pointing Constraints (CTVMFT), 1993. CDF-note: CDF/DOC/SEC_VTX/PUBLIC/1996, for Run II wrappering see CdfCode browser VertexAlg/doc/ctvmft.txt for documentation and VertexAlg/src for the implementation.

[76] K. Anikeev et al. B Meson Lifetime Measurements Using Exclusively Reconstructed Decays $B \rightarrow J/\psi X$, 2003. CDF-note: CDF/DOC/BOTTOM/CDFR/6266.

[77] R. Madrak. Measurement of the Λ_B Lifetime in the Decay Mode $\Lambda_B \rightarrow J/\psi\Lambda$, 2003. CDF-note: CDF/THESIS/BOTTOM/CDFR/6718.

[78] K. Anikeev et al. Calibration of Energy Loss and Magnetic Field using J/ψ Events in Run II, 2002.
CDF-note: CDF/DOC/BOTTOM/CDFR/5958.

[79] Ch. Paus I. Furic and J. Seely. Track Trigger Simulation at the Generator Level in Run II, 2000. CDF-note: CDF/DOC/TRIGGER/CDFR/5348.

[80] A.Korn K.Anikeev and Ch.Paus. Generator Level Dimuon Trigger Simulation, 2001. CDF-note: CDF/DOC/BOTTOM/CDFR/5686.

[81] L. Vacavant. GEANT Description of the CDF Inner Tracker Passive Material, 2002. CDF-note: CDF/DOC/MONTECARLO/CDFR/5825.

[82] Liz Sexton-Kennedy Joe Boudreau and Elena Gerchtein. Cdf material list. See CdfCode browser: GeometryBase/src/CdfMaterialsList.cc (version 4.11.2).

[83] C. Newman-Holmes. Fitting the Magnetic Field of the CDF Magnet, 1985. CDF-note: CDF/DOC/CDF/PUBLIC/0361.

[84] E. Schmidt C. Newman-Holmes and R. Yamada. *NIM*, A(274):443, 1989.

[85] C. Newman-Holmes R. Yamada and E. Schmidt. Measurement of the Magnetic Field of the CDF Magnet, 1985. CDF-note: CDF/DOC/CDF/PUBLIC/0346.

[86] C. Newman-Holmes R. Yamada and E. Schmidt. Measurement of the Magnetic Field of the CDF Magnet, 1988. CDF-note: CDF/PUB/CDF/PUBLIC/0667.

[87] H. Jensen D. Crane and C. Newman-Holmes. Solenoid Magnetic Field in the 1988-1989 Run, 1989. CDF-note: CDF/MEMO/ELECTROWEAK/CDFR/0969.

[88] A. Mukherjee and tracking group. private communication.